REPORT DOCUMENTATION PAGE

Form Approved OMB NO. 0704-0188

The public reporting burden for this collection of information is estimated to average 1 hour per response, including the time for reviewing instructions, searching existing data sources, gathering and maintaining the data needed, and completing and reviewing the collection of information. Send comments regarding this burden estimate or any other aspect of this collection of information, including suggesstions for reducing this burden, to Washington Headquarters Services, Directorate for Information Operations and Reports, 1215 Jefferson Davis Highway, Suite 1204, Arlington VA, 22202-4302. Respondents should be aware that notwithstanding any other provision of law, no person shall be subject to any oenalty for failing to comply with a collection of information if it does not display a currently valid OMB control number.
PLEASE DO NOT RETURN YOUR FORM TO THE ABOVE ADDRESS.

1. REPORT DATE (DD-MM-YYYY) 13-10-2014	2. REPORT TYPE Ph.D. Dissertation	3. DATES COVERED (From - To) -

4. TITLE AND SUBTITLE
Density Functional Theory Embeddingfor Correlated Wavefunctions

5a. CONTRACT NUMBER
W911NF-11-1-0256

5b. GRANT NUMBER

5c. PROGRAM ELEMENT NUMBER
611102

5d. PROJECT NUMBER

5e. TASK NUMBER

5f. WORK UNIT NUMBER

6. AUTHORS
Jason Goodpaster

7. PERFORMING ORGANIZATION NAMES AND ADDRESSES
California Institute of Technology
Office of Sponsored Research
1200 E. California Blvd.
Pasadena, CA 91125 -0001

8. PERFORMING ORGANIZATION REPORT NUMBER

9. SPONSORING/MONITORING AGENCY NAME(S) AND ADDRESS (ES)
U.S. Army Research Office
P.O. Box 12211
Research Triangle Park, NC 27709-2211

10. SPONSOR/MONITOR'S ACRONYM(S)
ARO

11. SPONSOR/MONITOR'S REPORT NUMBER(S)
58243-CH.11

12. DISTRIBUTION AVAILIBILITY STATEMENT
Approved for public release; distribution is unlimited.

13. SUPPLEMENTARY NOTES
The views, opinions and/or findings contained in this report are those of the author(s) and should not contrued as an official Department of the Army position, policy or decision, unless so designated by other documentation.

14. ABSTRACT

Methods that exploit the intrinsic locality of molecular interactions show significant promise in making tractable the electronic structure calculation of large-scale systems. In particular, embedded density functional theory (e-DFT) offers a formally exact approach to electronic structure calculations in which the interactions between subsystems are evaluated in terms of their electronic density. In the following dissertation, methodological advances of embedded density functional theory are described,

15. SUBJECT TERMS
Density Functional Theory Embeddingfor Correlated Wavefunctions

16. SECURITY CLASSIFICATION OF: a. REPORT	b. ABSTRACT	c. THIS PAGE	17. LIMITATION OF ABSTRACT	15. NUMBER OF PAGES	19a. NAME OF RESPONSIBLE PERSON
UU	UU	UU	UU		Thomas Miller
					19b. TELEPHONE NUMBER 626-395-6588

Standard Form 298 (Rev 8/98)
Prescribed by ANSI Std. Z39.18

Report Title

Density Functional Theory Embeddingfor Correlated Wavefunctions

ABSTRACT

Methods that exploit the intrinsic locality of molecular interactions show significant promise in making tractable the electronic structure calculation of large-scale systems. In particular, embedded density functional theory (e-DFT) offers a formally exact approach to electronic structure calculations in which the interactions between subsystems are evaluated in terms of their electronic density. In the following dissertation, methodological advances of embedded density functional theory are described, numerically tested, and applied to real chemical systems.

First, we describe an e-DFT protocol in which the non-additive kinetic energy component of the embedding potential is treated exactly. Then, we present a general implementation of the exact calculation of the non-additive kinetic potential (NAKP) and apply it to molecular systems. We demonstrate that the implementation using the exact NAKP is in excellent agreement with reference Kohn-Sham calculations, whereas the approximate functionals lead to qualitative failures in the calculated energies and equilibrium structures.

Next, we introduce density-embedding techniques to enable the accurate and stable calculation of correlated wavefunction (CW) in complex environments. Embedding potentials calculated using e-DFT introduce the effect of the environment on a subsystem for CW calculations (WFT-in-DFT). We demonstrate that WFT-in-DFT calculations are in good agreement with CW calculations performed on the full complex.

We significantly improve the numerics of the algorithm by enforcing orthogonality between subsystems by introduction of a projection operator. Utilizing the projection based embedding scheme, we rigorously analyze the sources of error in quantum embedding calculations in which an active subsystem is treated using CWs, and the remainder using density functional theory. We show that the embedding potential felt by the electrons in the active subsystem makes only a small contribution to the error of the method, whereas the error in the nonadditive exchange-correlation energy dominates. We develop an algorithm which corrects this term and demonstrate the accuracy of this corrected embedding scheme.

Density Functional Theory Embedding for Correlated Wavefunctions

Thesis by

Jason D. Goodpaster

In Partial Fulfillment of the Requirements

for the Degree of

Doctor of Philosophy

California Institute of Technology

Pasadena, California

2014

(Defended May 15, 2014)

© 2014

Jason D. Goodpaster

All Rights Reserved

To Julia

Acknowledgments

It is with immense gratitude that I acknowledge the support and help of my thesis advisor Professor Thomas F. Miller III. His encouragement, enthusiasm, and guidance was invaluable throughout my Ph.D. He has taught me how to develop interesting questions and how to approach answering them. He has made me a better scientist, theorist, and communicator. I truly cannot imagine a better advisor and mentor for my graduate studies.

Additionally, I would like to thank the faculty of the Division of Chemistry and Chemical Engineering. In particular, I thank my thesis committee, Dr. William Goddard III, Dr. Zhen-Gang Wang, and Dr. Mark Davis for their support, scientific discussions, and guidance in my future career. I am also deeply grateful to the late Aron Kuppermann for his elegant presentation of quantum mechanics, constant encouragement, and his friendly late night discussions while we were "burning the midnight oil".

I also must thank the division administrative staff, Priscilla Boon for all the support she has provided to myself and the Miller Group, Kathy Bubash for her administrative expertise, and Tom Dunn, Zailo Leite, and Naveed Near-Ansari for their technical expertise, specifically with computing.

I thank all the members of the Miller group: Bin, Nick, Nandini, Romelia, Artur, Josh, Connie, Taylor, Mike, Fran, Kuba, Frank, Michiel, Joonho, Mark, and Matt. Thank you all for your scientific discussion, help with coding and computing, and encouragement. It was truly an honor to work with you all.

I thank my family, my parents and my sister, for your constant support throughout graduate school; you were always there for me. I thank my friends for their understanding, encouragement, and for making my graduate school experience more enjoyable.

Lastly, thank you Julia. You challenge me to be a better scientist and person, you support me in all my endeavors, and you encourage me to strive above and beyond. Thank you for going through this together.

Abstract

Methods that exploit the intrinsic locality of molecular interactions show significant promise in making tractable the electronic structure calculation of large-scale systems. In particular, embedded density functional theory (e-DFT) offers a formally exact approach to electronic structure calculations in which the interactions between subsystems are evaluated in terms of their electronic density. In the following dissertation, methodological advances of embedded density functional theory are described, numerically tested, and applied to real chemical systems.

First, we describe an e-DFT protocol in which the non-additive kinetic energy component of the embedding potential is treated exactly. Then, we present a general implementation of the exact calculation of the non-additive kinetic potential (NAKP) and apply it to molecular systems. We demonstrate that the implementation using the exact NAKP is in excellent agreement with reference Kohn-Sham calculations, whereas the approximate functionals lead to qualitative failures in the calculated energies and equilibrium structures.

Next, we introduce density-embedding techniques to enable the accurate and stable calculation of correlated wavefunction (CW) in complex environments. Embedding potentials calculated using e-DFT introduce the effect of the environment on a subsystem for CW calculations (WFT-in-DFT). We demonstrate that WFT-in-DFT calculations are in good agreement with CW calculations performed on the full complex.

We significantly improve the numerics of the algorithm by enforcing orthogonality between subsystems by introduction of a projection operator. Utilizing the projection-based embedding scheme, we rigorously analyze the sources of error in quantum embedding calculations in which an active subsystem is treated using CWs, and the remainder using density functional theory. We show that the embedding potential felt by the electrons in the active subsystem makes only a small contribution to the error of the method, whereas the error in the nonadditive exchange-correlation energy dominates. We develop an algorithm which corrects this term and demonstrate the accuracy of this corrected embedding scheme.

Contents

Acknowledgments **iv**

Abstract **vi**

Summary **1**

1 Exact non-additive kinetic potentials for embedded density functional theory **6**

1.1 Introduction 6

1.2 Orbital-Free Embedded DFT 7

1.3 The Exact Non-Additive Kinetic Potential 10

1.3.1 Step 1: The Levy Constrained Search 10

1.3.2 Step 2: Exact Kinetic Potentials from KS Orbitals 11

1.3.3 Computational Details 14

1.3.3.1 Basis Sets 15

1.3.3.2 DFT Implementation Details 15

1.3.3.3 ZMP Extrapolation 16

1.4 Results 17

1.5 Extension to Larger Systems 24

1.6 Conclusions 26

1.7 Appendix: Unrestricted Open-Shell e-DFT 27

2 Embedded density functional theory for covalently bonded and strongly interacting subsystems **33**

2.1 Introduction 33

2.2 Theory 34

2.2.1 Orbital-Free Embedded DFT 34

2.2.2 Exact Calculations of NAKP 36

2.3 Implementation Details 38

2.3.1 Supermolecular vs. Monomolecular Basis Sets 38

2.3.2 ZMP Step 38

2.3.3 NAKP Numerics for Regions of Weak Density Overlap 39

2.4 Results: Small Systems 41

2.4.1 Calculation Details 41

2.4.2 Water Dimer 43

2.4.3 Li^+-Be 45

2.4.4 CH_3-CF_3 47

2.5 Results: Extension to Larger Systems 48

2.5.1 Pairwise Treatment of the NAKP 48

2.5.2 Water Trimer Application: Testing Pairwise Additivity in the NAKP 50

2.5.3 Parallel Scaling of e-DFT-EE 52

2.6 Conclusions 54

3 Density functional theory embedding for correlated wavefunctions: Improved methods for open-shell systems and transition metal complexes 61

3.1 Introduction 61

3.2 Theory 62

3.2.1 DFT-in-DFT Embedding 62

3.2.2 WFT-in-DFT Embedding 65

3.3 Methods of Implementation 66
3.3.1 Embedding for Open-Shell Systems 67
3.3.1.1 Open-Shell DFT-in-DFT Embedding 67
3.3.1.2 Open-Shell WFT-in-DFT Embedding 70
3.3.2 Optimized Effective Potential 71
3.3.3 Orbital-Occupation Freezing 74
3.3.4 Computational Details 75
3.4 Results 78
3.4.1 The Ethylene-Propylene Dimer: WFT-in-DFT Embedding . . 78
3.4.2 The Hexaaquairon(II) Cation 79
3.4.2.1 DFT-in-DFT Embedding 79
3.4.2.2 WFT-in-DFT Embedding 82
3.5 Conclusion 87

4 Accurate and systematically improvable density functional theory embedding for correlated wavefunctions 94

4.1 Introduction 94
4.2 Projector-Based Embedding 95
4.3 Results I: Sources of error in WFT-in-DFT embedding 98
4.3.1 Term-By-Term Comparison with LCSSD(T) 98
4.3.2 Calculation Details 100
4.3.3 Sources of Error in WFT-in-DFT embedding 103
4.3.3.1 Error from the Embedding Potential 103
4.3.3.2 Error from Use of DFT for Subsystem B 104
4.3.3.3 Error from the Nonadditive Exchange-Correlation Energy 105
4.3.4 Improvement of the Nonadditive Exchange-Correlation Energy 106

4.4 Results II: Continuity, Convergence, and Conjugation in WFT-in-DFT embedding 108
4.4.1 Potential Energy Surfaces 108
4.4.2 WFT-in-DFT Embedding of Conjugated Systems 109
4.5 Conclusions 115
4.6 Accurate and Systematically Improvable Density Functional Theory Embedding for Correlated Wavefunctions: Supplemental Information 117
4.6.1 Potential Energy Surfaces 117
4.7 Data Set Computational Details 118
4.7.1 Symmetric S_N2 Reaction Barrier 118
4.7.2 Acid Hydrolysis Reaction Energy 120
4.7.3 Phenol Deprotonation 121
4.7.4 Ring Closing 122
4.7.5 Diels Alder 124

Outlook **132**

List of Figures

1.1 Accuracy in the extrapolation of kinetic energy from the ZMP method 15
1.2 The 2s electron density for an isoelectronic series of atoms calculated using KS-DFT and e-DFT 17
1.3 The KSCED effective potential for an isoelectronic series of atoms . . . 21
1.4 The NAKP, KSCED effective potential, and the 2s electron density for the modified NAKP 25

2.1 The water dimer dissociation curve obtained using KS-DFT and e-DFT 43
2.2 Basis set dependence of the water dimer dissociation curve obtained using KS-DFT and e-DFT 45
2.3 The Li^+-Be dissociation curve obtained using KS-DFT and e-DFT . . 46
2.4 The CH_3-CF_3 dissociation curve for heterolytic cleavage of the C-C bond obtained using KS-DFT and e-DFT 48
2.5 Symmetric dissociation curves for the water trimer, illustrating the pairwise additivity of the NAKP. 51
2.6 Wall-clock timings for lattices of hydrogen molecules 53
2.7 Error in the total energy of e-DFT relative to KS-DFT for lattices of hydrogen molecules 54

3.1 An illustrative Newton step in the OEP calculation 75
3.2 WFT-in-DFT embedding for the ethylene-propylene dimer. 77
3.3 DFT-in-DFT embedding for the hexaaquairon(II) cation. 80
3.4 MP2-in-DFT embedding for the hexaaquairon(II) cation. 83

3.5 CCSD(T)-in-DFT embedding for the hexaaquairon(II) cation. 85

4.1 Contributions to the total WFT-in-DFT error 103
4.2 MP2 corrected WFT-in-DFT errors 106
4.3 Potential energy surface for 1-penten-1-one 108
4.4 Error in dissociation of F^- from alkane chain 110
4.5 Error in dissociation of F^- from alkene chain 112
4.6 Error in exchange reaction energy for alkane and alkene chains 114
4.7 Discontinuities in the potential energy surface for 1-penten-1-one . . . 118

List of Tables

1.1 Total energy and ionization energy obtained using KS-DFT and e-DFT. 20

1.2 Total energy and ionization energy obtained using e-DFT with the NAKP switching function 24

3.1 High-spin/low-spin splitting energies in cm^{-1} for the hexaaquairon(II) cation using MP2 theory and MP2-in-DFT 84

3.2 High-spin/low-spin splitting energies in cm^{-1} for the hexaaquairon(II) cation using CCSD(T) theory and CCSD(T)-in-DFT 86

4.1 CCSD(T) reaction energies and barriers in the test set 102

4.2 Change in the dipole moment for dissociation of F^- from the alkane and alkene chains 113

Summary

Quantum-chemistry calculations invariably feature a compromise between computational efficiency and accuracy. Kohn-Sham Density Functional Theory (KS-DFT) is one of the most commonly used methods because it is tractable for systems containing up to a thousand atoms. However, DFT methods, which generally employ approximate descriptions of electron correlation, often fail to even qualitatively predict reaction barriers, which are critical in determining reaction rates and mechanisms. More rigorous correlated wavefunction (CW) methods can provide an accurate and systematically improvable description of reaction barriers, but poor scaling of these methods can lead to impractical computation costs for systems with even tens of atoms.

Embedded density functional theory (e-DFT), is a formally exact approach to electronic structure, which exploits the locality of molecular interactions. In the e-DFT approach, a system is divided into smaller subsystems. Then, the interactions between subsystems are evaluated in terms of their electronic density. This approach naturally leads to two different partitioning schemes. One, a large system can be separated into many smaller subsystems, allowing for significant computational savings as this leads to a naturally parallelizable algorithm. Two, a large system is separated into a 'high-level' (accurate) and a 'low-level' (approximate) regions; therefore, if higher accuracy is required for a region of system, a higher level of theory can be seamlessly embedded into a DFT environment and still remain computationally tractable as only a handful of atoms are treated at the CW level. The objectives of the e-DFT approach are thus similar to those of more approximate partitioning and frag-

mentation schemes; however, e-DFT avoids the uncontrolled approximations (such as link atoms) and errors associated with subsystem interfaces that fundamentally limit other widely used methods.

This dissertation is focused on the development of new methods that make e-DFT an accurate, practical, and scalable method for the description of complex systems. The following key contributions are discussed: (i) the development of numerically exact methods for obtaining subsystem embedding potentials in e-DFT, which reduce embedding errors by orders of magnitude in comparison with previously available approximate methods, (ii) the development of parallelization algorithms that enable the description of large systems with sub-linear scaling of the required computational time, (iii) the combination of e-DFT potentials with correlated wavefunction theory (WFT) methods to enable seamless WFT-in-DFT embedding for general systems, and (iv) the development of systematically improvable methods for WFT-in-DFT to allow for a hierarchy of embedding methods with increasing accuracy.

In Chapter 1, we describe an embedded density functional theory (DFT) protocol in which the non-additive kinetic energy component of the embedding potential is treated exactly. At each iteration of the Kohn-Sham equations for constrained electron density, the Zhao-Morrison-Parr constrained search method for constructing Kohn-Sham orbitals is combined with the King-Handy expression for the exact kinetic potential. We use this exact embedding protocol to calculate ionization energies for a series of 3- and 4-electron systems, and the results are compared to embedded DFT calculations that utilize the Thomas-Fermi (TF) and the Thomas-Fermi-von Weisacker approximations to the kinetic energy functional. These calculations illustrate a breakdown due to the TF approximation for the non-additive kinetic potential, with errors of 30-80% in the calculated ionization energies; by contrast, the exact protocol is found to be accurate and stable. This work has been published as J. D. Goodpaster,

N. Ananth, F. R. Manby, and T. F. Miller III, "Exact non-additive kinetic potentials for embedded density functional theory," *J. Chem. Phys.*, **133**, 084103 (2010).

In Chapter 2, we present a general implementation of the exact calculation of the non-additive kinetic potential (NAKP). Potential energy curves are computed for the dissociation of Li^+-Be, CH_3-CF_3, and hydrogen-bonded water clusters, and e-DFT results obtained using this exact treatment of the NAKP are compared with those obtained using approximate kinetic energy functionals. In all cases, the exact NAKP is in excellent agreement with reference Kohn-Sham calculations, whereas the approximate functionals lead to qualitative failures in the calculated energies and equilibrium structures. We also demonstrate an accurate pairwise approximation to the NAKP that allows for efficient parallelization of the method in large systems; benchmark calculations on molecular crystals reveal ideal, size-independent scaling of wall-clock time with increasing system size. This work has been published as J. D. Goodpaster, T. A. Barnes, and T. F. Miller III, "Embedded density functional theory for covalently bonded and strongly interacting subsystems," *J. Chem. Phys.*, **134**, 164108 (2011).

In Chapter 3, we introduce density embedding techniques to enable the accurate and stable calculation of CWs in complex environments. Embedding potentials calculated using e-DFT introduce the effect of the environment on a subsystem for wavefunction calculations (WFT-in-DFT). These methods are demonstrated for calculating the potential energy curve of the dispersion-bound ethene-propene dimer and for the hexaaquairon(II) ion (HA). The potential energy curve for the ethene-propene dimer reveals that benchmark CCSD(T) calculations performed over the full complex can be reproduced within 0.05 kcal/mol using this method, illustrating that small energy differences can be accurately calculated while embedding across a covalent bond. e-DFT calculations on HA that employ these new techniques demonstrate that Kohn-Sham (KS-DFT) calculations can be reproduced for both the low-spin and the high-spin states. The ability of different exchange-correlation (XC) functionals to describe the energy differences between the low-spin and the high-spin states (ΔE_{LH}) and to describe the ligation energy in HA is studied. KS-DFT calculations of ΔE_{LH} demonstrate a strong dependency on XC functionals where WFT-in-DFT calculations reveal a significantly diminished dependency and that ΔE_{LH} is in good agreement with *ab initio* calculations performed on the full complex. The ligation energies have a small dependency on the XC functional and are near identical for KS-DFT and WFT-in-DFT demonstrating that the interactions energies between subsystems remain at DFT level accuracy. This work has been published as J. D. Goodpaster, T. A. Barnes, F. R. Manby, and T. F. Miller III, "Density functional theory embedding for correlated wavefunctions: Improved methods for open-shell systems and transition metal complexes," *J. Chem. Phys.*, **137**, 224113 (2012).

In Chapter 4, we present continuing work on projection based embedding. The original formulation has been published as F. R. Manby, M. Stella, J. D. Goodpaster, and T. F. Miller III, "A simple, exact density-functional-theory embedding scheme," *J. Chem. Theory Comput.*, **8**, 2564 (2012) and T. A. Barnes, J. D. Goodpaster, F. R. Manby, and T. F. Miller III, "Accurate basis set truncation for wavefunction embedding," *J. Chem. Phys.*, **139**, 024103 (2013). Building upon that work, we analyze the sources of error in quantum embedding calculations in which an active subsystem is treated using CW methods, and the remainder using DFT. We show that the embedding potential felt by the electrons in the active subsystem makes only a small contribution to the error of the method whereas the error in the nonadditive exchange-correlation energy dominates. We test an MP2 correction for this term and demonstrate that the corrected embedding scheme accurately reproduces the full wavefunction calculations for a series of chemical reactions. This work has been published as J. D. Goodpaster, T. A. Barnes, F. R. Manby, and T. F. Miller III, "Accurate and systematically improvable density functional theory embedding for correlated wavefunctions," *J. Chem. Phys.*, **140**, 18A507 (2014).

Chapter 1

Exact non-additive kinetic potentials for embedded density functional theory

1.1 Introduction

Orbital-free embedded density functional theory (e-DFT) is an appealing method for calculating the electronic structure of complex molecular systems. It provides a formally exact framework for dividing the total electronic density of a system into subsystem densities that can be separately calculated.[1–4] This feature of e-DFT allows for the development of multiscale strategies in which the electronic density for regions of central interest is calculated with high accuracy, while the electronic density for surrounding regions is obtained using more approximate techniques.[5–7]

However, in addition to the usual approximations for the basis set and the exchange-correlation functional that appear in Kohn-Sham (KS) DFT,[8] e-DFT requires the evaluation of a non-additive contribution to the kinetic energy from the subsystem densities.[4] This term, which is generally largest for cases in which the subsystem densities are strongly overlapping,[9] is a significant source of error in many e-DFT calculations, and it currently limits the method to applications in which the subsystem densities involve non-bonded or weakly interacting molecular groups.[4,9] Although encouraging progress towards the accurate calculation of the non-additive kinetic energy contribution have been reported,[3,9–13] more work in this direction is needed.

In this paper, we present an exact protocol for calculating the non-additive kinetic energy contribution in e-DFT calculations, and we report calculations in which the protocol is applied to 3- and 4-electron systems that exhibit strongly overlapping subsystem densities. Although, in its numerically demonstrated form, this protocol does not offer any computational speed-up over the KS calculation for the full system, it suggests new methods to systematically, efficiently, and accurately perform e-DFT calculations for large systems, which we discuss.

1.2 Orbital-Free Embedded DFT

Suppose that the entire electronic density ρ_{AB} for a closed-shell system is divided into two subsystems, ρ_{A} and ρ_{B}, such that $\rho_{\mathrm{AB}} = \rho_{\mathrm{A}} + \rho_{\mathrm{B}}$. The one-electron orbitals that give rise to these subsystem electronic densities obey the coupled Kohn-Sham equations for constrained electron density (KSCED),[4]

$$\left[-\frac{1}{2}\nabla^2 + V_{\mathrm{eff}}^{\mathrm{KSCED}}[\rho_{\mathrm{A}}, \rho_{\mathrm{B}}; \mathbf{r}]\right] \phi_i^{\mathrm{A}}(\mathbf{r}) = \epsilon_i^{\mathrm{A}} \phi_i^{\mathrm{A}}(\mathbf{r}), \qquad i = 1, ..., \frac{N_{\mathrm{A}}}{2}, \tag{1.1}$$

$$\left[-\frac{1}{2}\nabla^2 + V_{\mathrm{eff}}^{\mathrm{KSCED}}[\rho_{\mathrm{B}}, \rho_{\mathrm{A}}; \mathbf{r}]\right] \phi_i^{\mathrm{B}}(\mathbf{r}) = \epsilon_i^{\mathrm{B}} \phi_i^{\mathrm{B}}(\mathbf{r}), \qquad i = 1, ..., \frac{N_{\mathrm{B}}}{2}, \tag{1.2}$$

where N_{A} and N_{B} are the number of electrons in the respective subsystems,

$$\rho_{\mathrm{A}}(\mathbf{r}) = 2\sum_{i=1}^{N_{\mathrm{A}}/2} |\phi_i^{\mathrm{A}}(\mathbf{r})|^2, \qquad \text{and} \tag{1.3}$$

$$\rho_{\mathrm{B}}(\mathbf{r}) = 2\sum_{i=1}^{N_{\mathrm{B}}/2} |\phi_i^{\mathrm{B}}(\mathbf{r})|^2. \tag{1.4}$$

In these coupled equations, $V_{\mathrm{eff}}^{\mathrm{KSCED}}[\rho_{\mathrm{A}}, \rho_{\mathrm{B}}; \mathbf{r}]$ is the KS effective potential for subsystem A embedded in subsystem B,

$$V_{\text{eff}}^{\text{KSCED}}[\rho_{\text{A}}, \rho_{\text{B}}; \mathbf{r}] = v_{\text{ne}}(\mathbf{r}) + v_{\text{J}}[\rho_{\text{AB}}; \mathbf{r}] + v_{\text{xc}}[\rho_{\text{AB}}; \mathbf{r}] + v_{\text{nad}}[\rho_{\text{A}}, \rho_{\text{B}}; \mathbf{r}], \tag{1.5}$$

and $V_{\text{eff}}^{\text{KSCED}}[\rho_{\text{B}}, \rho_{\text{A}}; \mathbf{r}]$ is the similarly defined KS effective potential for subsystem B embedded in subsystem A. The contributions to the KS effective potential include

$$\begin{aligned} v_{\text{ne}}(\mathbf{r}) &= -\sum_{i}^{N_{\text{nuc}}} \frac{Z_i}{|\mathbf{r} - \mathbf{R}_i|}, & (1.6) \\ v_{\text{J}}[\rho_{\text{AB}}; \mathbf{r}] &= \int \frac{\rho_{\text{AB}}(\mathbf{r}')}{|\mathbf{r}' - \mathbf{r}|} d\mathbf{r}', \text{ and} & (1.7) \\ v_{\text{xc}}[\rho_{\text{AB}}; \mathbf{r}] &= \left[\frac{\delta E_{\text{xc}}[\rho]}{\delta \rho} \bigg|_{\rho=\rho_{\text{AB}}} \right] (\mathbf{r}), & (1.8) \end{aligned}$$

which are the usual nuclear-electron Coulomb potential, Hartree potential, and exchange-correlation potential, respectively, and N_{nuc} is the number of nuclei in the system. The final term in $V_{\text{eff}}^{\text{KSCED}}[\rho_{\text{B}}, \rho_{\text{A}}; \mathbf{r}]$ is the non-additive kinetic potential (NAKP)

$$v_{\text{nad}}[\rho_{\text{A}}, \rho_{\text{B}}; \mathbf{r}] = \left[\frac{\delta T_{\text{s}}^{\text{nad}}[\rho_{\text{A}}, \rho_{\text{B}}]}{\delta \rho_{\text{A}}} \right] (\mathbf{r}) = \frac{\delta T_{\text{s}}[\rho]}{\delta \rho} \bigg|_{\rho=\rho_{\text{AB}}} (\mathbf{r}) - \frac{\delta T_{\text{s}}[\rho]}{\delta \rho} \bigg|_{\rho=\rho_{\text{A}}} (\mathbf{r}), \tag{1.9}$$

which is obtained from the functional derivative of the non-additive component of the non-interacting kinetic energy

$$T_{\text{s}}^{\text{nad}}[\rho_{\text{A}}, \rho_{\text{B}}] = T_{\text{s}}[\rho_{\text{AB}}] - T_{\text{s}}[\rho_{\text{A}}] - T_{\text{s}}[\rho_{\text{B}}]. \tag{1.10}$$

The total energy functional for the embedded system is

$$E[\rho_{\text{AB}}] = T_{\text{s}}[\rho_{\text{A}}] + T_{\text{s}}[\rho_{\text{B}}] + T_{\text{s}}^{\text{nad}}[\rho_{\text{A}}, \rho_{\text{B}}] + V_{\text{ne}}[\rho_{\text{AB}}] + J[\rho_{\text{AB}}] + E_{\text{xc}}[\rho_{\text{AB}}], \tag{1.11}$$

where the last three terms on the right hand side (RHS) are the nuclear-electron Coulomb energy, Hartree energy, and exchange-correlation energy for the total density.

Two aspects of the orbital-free embedding DFT formulation are worth emphasizing. Firstly, like conventional KS-DFT, it is a theory that is exact in principle, but practical calculations must employ an approximate form for the unknown exchange-correlation functional. Secondly, unlike conventional KS-DFT calculations, the embedding formulation introduces an NAKP because the KS orbitals for subsystem A are not necessarily orthogonal to those of subsystem B. Without knowledge of the exact functional for the non-interacting kinetic energy, this creates a second source of approximation in the e-DFT approach. The significance of the NAKP is system dependent, with the most severe cases including those for which the subsystem densities ρ_{A} and ρ_{B} greatly overlap.[4,9,14,15]

The non-interacting kinetic energy for the density corresponding to a set of $\mathcal{N}$ closed-shell orbitals is

$$T_{\mathrm{s}}[\rho] = 2\sum_{i=1}^{\mathcal{N}} \langle \phi_i | -\frac{1}{2}\nabla^2 | \phi_i \rangle. \tag{1.12}$$

Standard approximations to this kinetic energy functional include the Thomas-Fermi (TF) result for the homogenous electron gas,[16,17]

$$T_{\mathrm{TF}}[\rho] = C_{\mathrm{TF}} \int \rho^{5/3}(\mathbf{r}) d\mathbf{r} \tag{1.13}$$

where $C_{\mathrm{TF}} = \frac{3}{10}(3\pi^2)^{2/3}$, and the von Weizsäcker (vW) result for the limit of a one-electron density,

$$T_{\mathrm{vW}}[\rho] = \frac{1}{8} \int \frac{|\nabla \rho(\mathbf{r})|^2}{\rho(\mathbf{r})} d\mathbf{r}. \tag{1.14}$$

Other approximate kinetic energy functionals can be constructed using the strategies from the development of exchange-correlation functionals. For example, the

PW91k kinetic energy functional[10,11] employs the analytical form of the Perdew-Wang (PW91) exchange functional,[19] and the TW02 functional[13] and the PBE2, PBE3, and PBE4 functionals[9] utilizes the form suggested by Becke.[20] These functionals have been shown to successfully describe weakly interacting systems and coordination compounds.[9] Furthermore, kinetic energy functionals that have been developed using linear response corrections to the homogeneous electron gas and have been shown to work well for metals.[3,21–23] However, no approximate kinetic energy functional has been demonstrated to yield accurate results for embedded subsystems that are connected by a covalent bond.[9,15,24]

1.3 The Exact Non-Additive Kinetic Potential

For each iteration of the KSCED equations (Eqs. 1.1 and 1.2), $\{\phi_i^{\mathrm{A}}\}$ and $\{\phi_i^{\mathrm{B}}\}$ (and thus ρ_{A} and ρ_{B}) are known from either the previous iteration or the initial guess, and the NAKP must be calculated. We employ a two-step protocol to obtain the exact NAKP. In the first step, a Levy constrained search[25] (LCS) or equivalent method is used to determine the full set of orthogonal KS orbitals, $\{\phi_i^{\mathrm{AB}}\}$, that correspond to the total density ρ_{AB}. In the second step, the NAKP is calculated from the orbital sets $\{\phi_i^{\mathrm{AB}}\}$, $\{\phi_i^{\mathrm{A}}\}$, and $\{\phi_i^{\mathrm{B}}\}$.

1.3.1 Step 1: The Levy Constrained Search

Given a total electron density ρ_{AB}, the fully orthogonal KS orbitals $\{\phi_i^{\mathrm{AB}}\}$ can be calculated from an LCS, in which the non-interacting kinetic energy is minimized with respect to one-electron orbitals that are constrained to yield ρ_{AB}.[25] Alternatively, we employ the approach of Zhao, Morrison, and Parr (ZMP),[26–28] in which the full set of KS orbitals are obtained by solving the one-electron equations

$$\left[-\frac{1}{2}\nabla^2 - \sum_{i}^{N_{\rm nuc}} \frac{Z_i}{|\mathbf{r}-\mathbf{R}_i|} + V_c^{\lambda}(\mathbf{r})\right] \phi_i^{\rm AB,\lambda}(\mathbf{r}) = \epsilon_i \phi_i^{\rm AB,\lambda}(\mathbf{r}), \qquad i = 1, ..., \frac{N_{\rm AB}}{2}, \tag{1.15}$$

where $N_{\rm AB} = N_{\rm A} + N_{\rm B}$,

$$V_c^{\lambda}(\mathbf{r}) = \lambda \int \frac{\rho_{\rm AB}(\mathbf{r}') - \tilde{\rho}_{\rm AB}(\mathbf{r}')}{|\mathbf{r}'-\mathbf{r}|} d\mathbf{r}', \tag{1.16}$$

$\tilde{\rho}_{\rm AB}(\mathbf{r}) = 2 \sum_{i=1}^{N_{\rm AB}/2} |\phi_i^{\rm AB}(\mathbf{r})|^2$, and $V_c^{\lambda}(\mathbf{r})$ is a potential energy function that restrains the $\tilde{\rho}_{\rm AB}(\mathbf{r})$ to the target density $\rho_{\rm AB}(\mathbf{r})$. Solution of Eq. 1.15 in the limit $\lambda \to \infty$ is equivalent to performing the LCS.[26–28]

In practice, Eq. 1.15 is solved for six large, but finite, values of λ, and the KS orbitals and eigenvalues are obtained via extrapolation.[26–28] For each value of λ, the $\{\epsilon_i^{\lambda}\}$, $\{\phi_i^{\rm AB,\lambda}\}$, and $\{\nabla^2\phi_i^{\rm AB,\lambda}\}$ are calculated and stored on a spatial grid. For the orbitals, extrapolation to $\lambda \to \infty$ is performed via expansion to third order in $\frac{1}{\lambda}$,

$$\phi_i^{\rm AB,\lambda}(\mathbf{r}) = \phi_i^{\rm AB}(\mathbf{r}) + \frac{1}{\lambda} a_i^{(1)}(\mathbf{r}) + \frac{1}{\lambda^2} a_i^{(2)}(\mathbf{r}) + \frac{1}{\lambda^3} a_i^{(3)}(\mathbf{r}), \tag{1.17}$$

with a linear least-squares fit of the expansion coefficients $\{\phi_i^{\rm AB}(\mathbf{r}), a_i^{(1)}(\mathbf{r}), a_i^{(2)}(\mathbf{r}), a_i^{(3)}(\mathbf{r})\}$ at each value of $\mathbf{r}$. The $\{\nabla^2\phi_i^{\rm AB}\}$ are similarly obtained via extrapolation at each value of $\mathbf{r}$, while each ϵ_i requires only a single extrapolation. With the $\{\phi_i^{\rm AB}\}$ and $\{\nabla^2\phi_i^{\rm AB}\}$ obtained on the spatial grid, the non-interacting kinetic energy for the total system can be calculated via numerical integration using Eq. 1.12.

1.3.2 Step 2: Exact Kinetic Potentials from KS Orbitals

To calculate the NAKP from the orbital sets $\{\phi_i^{\rm AB}\}$, $\{\phi_i^{\rm A}\}$, and $\{\phi_i^{\rm B}\}$, we extend the approach developed by King and Handy.[29]

Minimization of the electronic energy with respect to the total electron density ρ_{AB} yields the stationary condition[8]

$$\frac{\delta T_{\mathrm{s}}[\rho]}{\delta \rho}\bigg|_{\rho=\rho_{\mathrm{AB}}}(\mathbf{r}) + v_{\mathrm{ne}}(\mathbf{r}) + v_{\mathrm{J}}[\rho_{\mathrm{AB}};\mathbf{r}] + v_{\mathrm{xc}}[\rho_{\mathrm{AB}};\mathbf{r}] = \mu_{\mathrm{AB}} \tag{1.18}$$

where μ_{AB} is a Lagrange multiplier that imposes the constraint $\int \rho_{\mathrm{AB}}(\mathbf{r})d\mathbf{r} = N_{\mathrm{AB}}$. Furthermore, rearrangement of the usual KS equations yields

$$\frac{2}{\rho_{\mathrm{AB}}(\mathbf{r})}\sum_{i}^{N_{\mathrm{AB}}/2}\left(-\frac{1}{2}\phi_i^{\mathrm{AB}}(\mathbf{r})\nabla^2\phi_i^{\mathrm{AB}}(\mathbf{r}) - \epsilon_i\phi_i^{\mathrm{AB}}(\mathbf{r})^2\right) + v_{\mathrm{ne}}(\mathbf{r}) + v_{\mathrm{J}}[\rho_{\mathrm{AB}};\mathbf{r}] + v_{\mathrm{xc}}[\rho_{\mathrm{AB}};\mathbf{r}] = 0. \tag{1.19}$$

Comparison of these two results leads to an exact expression for the total kinetic potential,[29]

$$\frac{\delta T_{\mathrm{s}}[\rho]}{\delta \rho}\bigg|_{\rho=\rho_{\mathrm{AB}}}(\mathbf{r}) = \frac{2}{\rho_{\mathrm{AB}}(\mathbf{r})}\sum_{i}^{N_{\mathrm{AB}}/2}\left(-\frac{1}{2}\phi_i^{\mathrm{AB}}(\mathbf{r})\nabla^2\phi_i^{\mathrm{AB}}(\mathbf{r}) - \epsilon_i\phi_i^{\mathrm{AB}}(\mathbf{r})^2\right) + \mu_{\mathrm{AB}}. \tag{1.20}$$

Analogous results can be derived for each of the embedded subsystems. Specifically, the electron density for subsystem A also obeys a stationary condition,[2]

$$\frac{\delta T_{\mathrm{s}}[\rho]}{\delta \rho}\bigg|_{\rho=\rho_{\mathrm{A}}}(\mathbf{r}) + v_{\mathrm{ne}}(\mathbf{r}) + v_{\mathrm{J}}[\rho_{\mathrm{AB}};\mathbf{r}] + v_{\mathrm{xc}}[\rho_{\mathrm{AB}};\mathbf{r}] + v_{\mathrm{nad}}[\rho_{\mathrm{A}},\rho_{\mathrm{B}};\mathbf{r}] = \mu_{\mathrm{A}}, \tag{1.21}$$

where μ_{A} is the Lagrange multiplier that imposes the constraint $\int \rho_{\mathrm{A}}(\mathbf{r})d\mathbf{r} = N_{\mathrm{A}}$. Combination of Eq. 1.21 with Eq. 1.1 results in an exact expression for the subsystem kinetic potential,

$$\frac{\delta T_{\mathrm{s}}[\rho]}{\delta \rho}\bigg|_{\rho=\rho_{\mathrm{A}}}(\mathbf{r}) = \frac{2}{\rho_{\mathrm{A}}(\mathbf{r})}\sum_{i}^{N_{\mathrm{A}}/2}\left(-\frac{1}{2}\phi_i^{\mathrm{A}}(\mathbf{r})\nabla^2\phi_i^{\mathrm{A}}(\mathbf{r}) - \epsilon_i^{\mathrm{A}}\phi_i^{\mathrm{A}}(\mathbf{r})^2\right) + \mu_{\mathrm{A}}, \tag{1.22}$$

which can be compared with kinetic potential for the total system in Eq. 1.20.

Insertion of Eqs. 1.18 and 1.21 into Eq. 1.9 yields $\mu_{\mathrm{AB}} = \mu_{\mathrm{A}}$, and since A is an arbitrarily chosen subsystem, we likewise obtain $\mu_{\mathrm{AB}} = \mu_{\mathrm{B}}$, or

$$\mu_{\mathrm{A}} = \mu_{\mathrm{B}}. \tag{1.23}$$

This result has a simple physical interpretation. In the zero temperature limit, the Lagrange multipliers μ_{A} and μ_{B}, are equivalent to the chemical potential for the subsystem electronic densities.[8] Solution to the KSCED equations thus yields densities that are in equilibrium with respect to the number of electrons in each subsystem.

Finally, insertion of Eq. 1.20 and 1.22 into Eq. 1.9 yields the desired expression for the NAKP,

$$\begin{aligned} v_{\mathrm{nad}}[\rho_{\mathrm{A}}, \rho_{\mathrm{B}}; \mathbf{r}] &= \frac{2}{\rho_{\mathrm{AB}}(\mathbf{r})} \sum_{i}^{N_{\mathrm{AB}}/2} \left(-\frac{1}{2} \phi_i^{\mathrm{AB}}(\mathbf{r}) \nabla^2 \phi_i^{\mathrm{AB}}(\mathbf{r}) - \epsilon_i \phi_i^{\mathrm{AB}}(\mathbf{r})^2 \right) \\ &- \frac{2}{\rho_{\mathrm{A}}(\mathbf{r})} \sum_{i}^{N_{\mathrm{A}}/2} \left(-\frac{1}{2} \phi_i^{\mathrm{A}}(\mathbf{r}) \nabla^2 \phi_i^{\mathrm{A}}(\mathbf{r}) - \epsilon_i^{\mathrm{A}} \phi_i^{\mathrm{A}}(\mathbf{r})^2 \right). \end{aligned} \tag{1.24}$$

Note that the ZMP protocol generally yields a constant shift in the calculated set of KS eigenenergies, $\{\epsilon_i^\lambda\}$;[26] in Eq. 1.24, we see that this leads only to a constant shift in $v_{\mathrm{nad}}[\rho_{\mathrm{A}}, \rho_{\mathrm{B}}; \mathbf{r}]$ and causes no change in any calculated observables. Throughout this study, the NAKP is shifted such that it approaches zero at large distances.

Visscher and coworkers previously observed that the NAKP can be expressed in terms of the stationary condition for the total system (Eq. 1.18) and a subsystem (Eq. 1.21).[30] They suggested a strategy in which the ZMP method is used to obtain the external potentials for both the full system and the subsystem, so that the difference between those potentials is equal to the NAKP, but this strategy has not been implemented to our knowledge. The approach presented here directly expresses the NAKP in terms of the KS orbitals for the total system and the subsystem (Eq. 1.24); it avoids performing the ZMP method for the subsystem, and it avoids using the difference between two potentials that are obtained via the ZMP method. It is straightforward to show that Eq. 1.24 recovers the limit for weakly overlapping subsystem densities that is reported in Ref. 30.

In another approach that does not utilize the exact framework of the KSCED equations, Aguado and coworkers employ an embedding strategy in which the ZMP formalism is used to constrain the sum of the subsystem densities to that of the total density.[31,32] This approach has been pursued as a useful, but approximate, strategy for partitioning a total density into subsystems.

Other e-DFT strategies also express the kinetic potential in terms of the KS orbitals, as we have done here. For example, Huang and Carter report an explicit expression for the kinetic potential in terms of the KS orbitals, using the assumption that the non-interacting kinetic energy is a linear functional of the density; an empirical parameter is included in their result to account for non-linear effects.[33] The approach presented here involves no adjustable parameters and no assumptions about the linearity of the kinetic energy functional.

1.3.3 Computational Details

Calculations are performed on four atomic systems: Li, Ne^{7+}, $\mathrm{Q}_{2.5}^{-0.5}$ and Be, where $\mathrm{Q}_{2.5}^{-0.5}$ is a model 3-electron atom that has a nuclear charge of +2.5. In all e-DFT calculations, we take ρ_{A} to be the density for a single 2s electron, and ρ_{B} includes all other electrons. The KSCED equations for each system were solved with ρ_{B} fixed at the density obtained from the corresponding orbitals of an unrestricted KS-DFT calculation on the full system; this is justified for the cases studied here because solution of the KSCED equations for ρ_{A} subject to a fixed $\rho_{\mathrm{B}} \leq \rho_0$ (at all $\mathbf{r}$), where ρ_0 is the exact ground state density for the full system, ensures the exact calculation of the ground state energy and ground state density.[4] All calculations were performed using in-house codes, and all results are reported in atomic units.

1.3.3.1 Basis Sets

All calculations were performed using the fully uncontracted cc-pVTZ basis set of Gaussian-type orbitals (GTOs),[34] with only the s-type orbitals included. For calculations on $Q_{2.5}^{-0.5}$, the Li basis set was used. For Ne^{7+}, the most diffuse s-orbital was removed to facilitate convergence. Although not reported, all calculations were also repeated with slater-type orbitals, which led to somewhat improved convergence but very similar numerical accuracy.

1.3.3.2 DFT Implementation Details

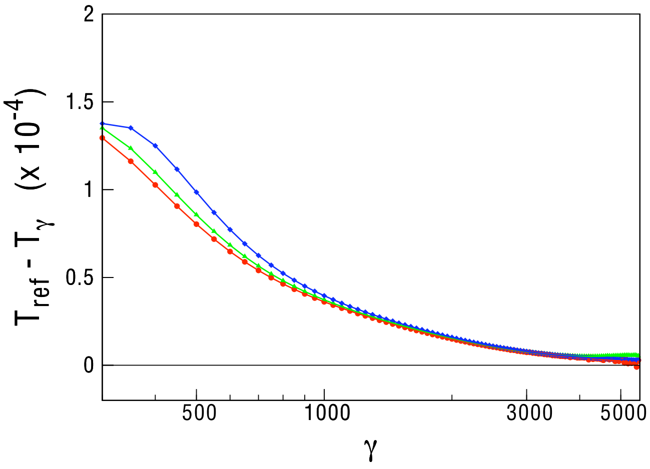

Figure 1.1: The difference between the non-interacting kinetic energy $T_{\mathrm{s}}[\rho]$ from KS-DFT and from the ZMP method, plotted as a function of γ. The extrapolation is performed using $\{\lambda\} = \{\gamma - j\tau\}$, $j = 5, 4, \ldots, 0$, and using τ of 10 (red), 20 (green), and 40 (blue). See text for details.

For all applications considered here, ρ_{A} is an open shell system, and the calculations were performed using the unrestricted KS formalism. Details for the unrestricted KSCED equations are given in the Appendix. All calculations employ the Slater exchange functional[35] and the Vosko, Wilk, and Nusair correlation functional.[36] In calculating $V_{\mathrm{eff}}^{\mathrm{KSCED}}[\rho_{\mathrm{A}}, \rho_{\mathrm{B}}; \mathbf{r}]$, a uniform radial grid is used to evaluate the exchange-correlation functions, $\{\phi^{\mathrm{AB}}\}$, $\{\nabla^2\phi^{\mathrm{AB}}\}$, and the NAKP. Upon convergence of the

KSCED equations, the same radial grid is used to evaluate the exchange-correlation energy and to numerically integrate the kinetic energy. For Be and Li the grid extends from $r = 0$ to 15, while for $Q_{2.5}^{-0.5}$, $r = 0$ to 20 and Ne^{7+}, $r = 0$ to 2. For Be, Li and Q the grid density is 2000 points/a_0 and for Ne^{7+}, 20000 points/a_0. We note that future applications that employ either a non-uniform[37] or variational[38] mesh will require fewer gridpoints to achieve the same level of accuracy. Unless otherwise stated, the iterative solution of the KSCED equations were deemed converged when the total energy of the system changed by less than 10^{-8} Hartrees between successive iterations.

1.3.3.3 ZMP Extrapolation

To examine the extrapolation error associated with the ZMP method, convergence tests were performed for the Li atom system. The total density for the system, ρ_{AB}, and the reference value for the non-interacting kinetic energy were calculated from a full KS calculation. This ρ_{AB} was used to define the restraint potential (Eq. 1.16), and the ZMP extrapolation was performed using six equally spaced values of λ (i.e., $\{\lambda\} = \{\gamma - j\tau\}$, where $j = 5, 4, \ldots, 0$). For a given pair of parameters γ and τ, the non-interacting kinetic energy was numerically integrated, and the extrapolation error was taken to be the difference between this result and the reference value from the full KS calculation. Fig. 1.1 presents this calculated error as a function γ and for various values of τ. These results indicate that the extrapolation error decreases to within 0.1 mH for $\gamma > 500$, and the spacing parameter τ has only a small effect. The error decreases to within 1 μH for larger values of γ. Results reported hereafter employ $\gamma = 600$ and $\tau = 10$. The orbitals from Eq. 1.15 were deemed converged when all occupied orbital coefficients changed less than 10^{-7} between successive iterations.

The ZMP extrapolation scheme used here does not constrain the normalization of the orbitals. In general, we found that extrapolation violated normalization by less then 0.01%, and it was found that normalizing the orbitals after extrapolation led to less than 0.1 mH change in the total energy. The results reported here do not include *a posteriori* orbital normalization.

1.4 Results

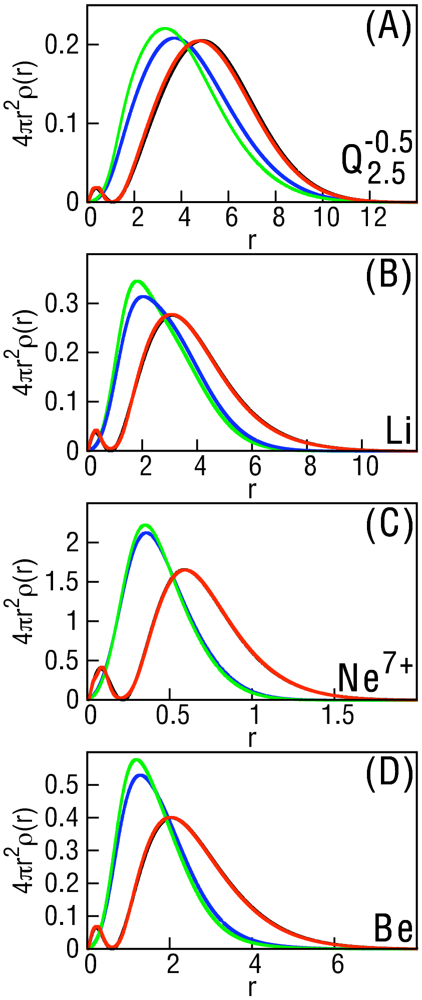

Figure 1.2: The 2s electron density (ρ_A) for **(A)** the $Q_{2.5}^{-0.5}$ ion, **(B)** the Li atom, **(C)** the Ne^{+7} ion, and **(D)** the Be atom. Calculations performed using e-DFT with the non-additive kinetic energy calculated using our exact protocol (red), the TF functional (blue), and the TFvW functional (green). The black curve, which is nearly indistinguishable from the exact protocol, presents the results from the full KS-DFT calculation.

e-DFT was performed for a series of three-electron systems, $Q_{2.5}^{-0.5}$, Li, and Ne^{7+}, as well as the four-electron Be atom. For each application, ρ_{A} was chosen to include a single 2s electron, and the remaining electrons were included in ρ_{B}. In addition to using the exact embedding protocol described here, the NAKP in the embedding calculations was treated using the approximate TF kinetic energy functional ($T_{\text{TF}}[\rho]$, Eq. 1.13) and the TFvW functional with the standard 1/9 mixing parameter ($T_{\text{TF}}[\rho]+\frac{1}{9}T_{\text{vW}}[\rho]$).

Fig. 1.2 presents the ρ_{A} obtained in these e-DFT calculations. For reference, Fig. 1.2 also includes the 2s orbital density from the full KS-DFT calculation. Absolute agreement between the KS-DFT results and the e-DFT results would only be expected if all results were obtained with the exact exchange-correlation functional. Nonetheless, since all calculations in this study employ the same approximate exchange-correlation functional, comparison of the e-DFT and KS-DFT results provides a significant test of the accuracy of the various NAKP descriptions.

Fig. 1.2 clearly demonstrates the sensitivity of e-DFT calculations to the method of treating the NAKP. In comparison to KS-DFT, the e-DFT results from the approximate TF and TFvW functionals are peaked at significantly shorter radial distances, and they qualitatively fail to capture the nodal structure. Interestingly, the vW correction to the TF functional actually worsens the agreement with the KS-DFT reference. The exact embedding protocol describe here, however, is graphically indistinguishable from the KS-DFT result.

Further evaluation of the e-DFT methods can be obtained by comparing the calculated one-electron ionization energies (IEs) for the various methods. The e-DFT IE is calculated from the difference between the total electron energy from Eq. 3.6 and the energy from a full KS-DFT calculation performed on the ionized (N-1 electron) system. These results are presented in Table 1.1, which again illustrates the qualitative shortcomings of the approximate NAKP treatments. For the approximate NAKP descriptions, the relative error between the e-DFT result and the KS-DFT result for the IEs ranges from 30-60% for 3-electron systems, and up to 80% for Be. As has been observed previously,[40] including the vW gradient correction decreases the accuracy of the IE calculation. The exact embedding protocol almost completely eliminates these differences with the reference calculation, with errors of less than 0.2% for $Q_{2.5}^{-0.5}$, Li, and Be and with an error of less 4% for Ne^{7+}.

The lower accuracy of our embedding protocol for the case of Ne^{7+} arises from the description of the nuclear cusp. The KSCED equations converged slowly for this case, and the convergence threshold had to be raised to 10^{-5} hartrees. By changing from GTOs to Slater-type orbitals (results not shown), the convergence problem was removed, and it was found that for all four applications, the IEs obtained using our e-DFT protocol were within 1% of the full KS-DFT result. Below, we describe how the use of a simple switching function for the NAKP in the cusp region also removes these convergence problems for the GTOs, while preserving the accuracy of the IE calculation.

We note that the ionization of the closed shell Be atom presents an electronic structure challenge that is similar to the homolytic cleavage of a covalent bond. From the perspective of the NAKP, this atomic system is especially challenging since both electrons in the 2s "bond" are co-localized on a single attractive center. The difficulty of this particular case is confirmed by the especially poor description provided by the TF and TFvW functionals for the IE of the Be atom. The excellent accuracy of the new embedding protocol for this case suggests that the method will allow for accurate e-DFT calculations in which the subsystems are linked by covalent bonds.

Fig. 1.3 illustrates the KSCED potentials, $V_{\mathrm{eff}}^{\mathrm{KSCED}}[\rho_{\mathrm{A}}, \rho_{\mathrm{B}}; \mathbf{r}]$, and the corresponding NAKPs, $v_{\mathrm{nad}}[\rho_{\mathrm{A}}, \rho_{\mathrm{B}}; \mathbf{r}]$, that are obtained from the exact embedding calculations. For each system, the similarity between these two potentials illustrates the dominance of the NAKP at short distances. However, the NAKP decays rapidly, and the KSCED potential is dominated at larger distances by the Coulombic terms (Eq. 1.5).

Table 1.1: Total energy (TE) and ionization energy (IE) obtained using KS-DFT and e-DFT.

Atom	Calculation	TE	IE	Error (%)
$Q_{2.5}^{-0.5}$				
	KS	-4.799405	0.060142	-
	TFvW	-4.835122	0.095258	59.99
	TF	-4.819221	0.079357	33.28
	Exact Embedding	-4.799510	0.060247	0.18
Li				
	KS	-7.343870	0.201098	-
	TFvW	-7.443321	0.300549	49.45
	TF	-7.408509	0.265737	32.14
	[a] Exact Embedding	-7.344046	0.201274	0.09
Ne^{7+}				
	KS	-101.964612	8.754056	-
	TFvW	-106.413890	13.203334	50.83
	TF	-105.630042	12.419486	41.87
	[b] Exact Embedding	-102.294207	9.083650	3.77
Be				
	KS	-14.447017	0.331698	-
	TFvW	-14.717243	0.601924	81.47
	TF	-14.635950	0.520631	56.96
	[a] Exact Embedding	-14.447463	0.328900	0.13

[a] KSCED equations converged to 10^{-7} Hartree

[b] KSCED equations converged to 10^{-5} Hartree

Although it is not visible from the scale of the plots in Fig. 1.3, the $v_{\rm nad}[\rho_{\rm A}, \rho_{\rm B}; \mathbf{r}]$ term comprises less than 1% of the $V_{\rm eff}^{\rm KSCED}[\rho_{\rm A}, \rho_{\rm B}; \mathbf{r}]$ for distances greater than 3 a.u. for all cases. (For $\rm Ne^{7+}$, this regime is reached at 0.43 a.u.)

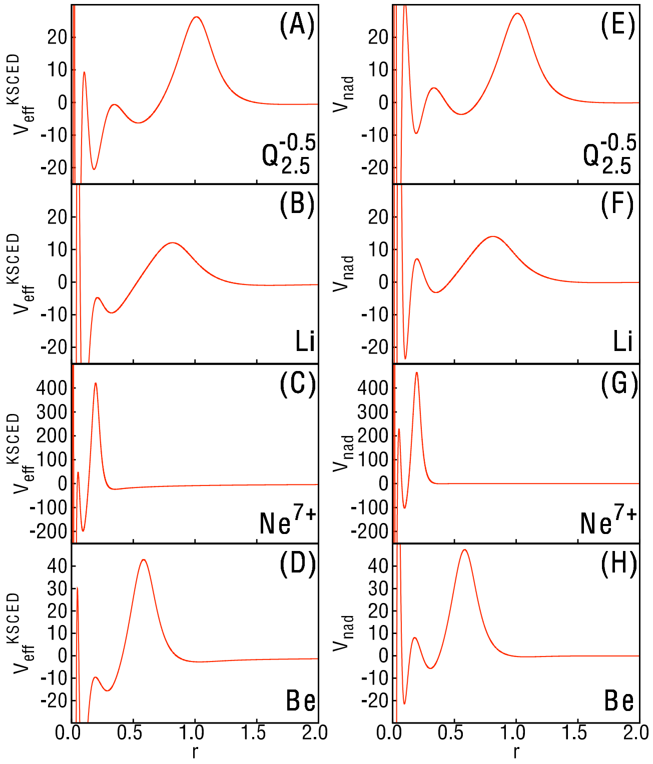

Figure 1.3: The KSCED effective potential, $V_{\rm eff}^{\rm KSCED}[\rho_{\rm A}, \rho_{\rm B}; \mathbf{r}]$, for **(A)** the $\rm Q_{2.5}^{-0.5}$ ion, **(B)** the Li atom, **(C)** the $\rm Ne^{+7}$ ion, and **(D)** the Be atom and the NAKP, $v_{\rm nad}[\rho_{\rm A}, \rho_{\rm B}; \mathbf{r}]$, for **(E)** the $\rm Q_{2.5}^{-0.5}$ ion, **(F)** the Li atom, **(G)** the $\rm Ne^{+7}$ ion, and **(H)** the Be atom using the e-DFT protocol presented here.

Comparison of the NAKPs in Fig. 1.3E-H with the densities in Fig. 1.2 illustrates that the nodal structure in the 2s electron density is enforced by the NAKP. For each system, the large outer peak in the NAKP coincides with the nodal feature in the 2s density. Unlike the KS-DFT results, we note that the densities obtained using e-DFT in Fig. 1.2 do not exhibit a genuine radial node, since $\rho_{\rm A}$ corresponds to the ground-state eigenvector of Eq. 1.1. A large peak in the e-DFT effective potential is therefore essential to achieve the correct 2s shell structure. The NAKPs obtained from the approximate TF and TFvW functionals do not exhibit this pronounced peak (not shown), which leads to the poor descriptions for the 2s electron density (Fig. 1.2) and the IE (Table 1.1).

In addition to the pronounced outer-most peak for each NAKP in Fig. 1.3E-H, oscillations at short distances are observed. This oscillatory behavior is sensitive to the basis set representation. Small changes in the orbital coefficients for regions of low density give rise to large changes in the kinetic potential (Eq. 1.24), resulting in slow convergence of the KSCED equations. (These oscillations are not observed when the density vanishes at large distances since the basis set expansion is dominated by only the slowest-decaying function in that regime.) Using STOs rather than GTOs, the NAKP oscillations at short distances were diminished (not shown), and the iterative convergence was improved. In future applications of the exact embedding protocol with GTOs, the use of the convergence acceleration algorithms such as DIIS[39] may prove beneficial. However, we now demonstrate that the problems associated with poor convergence and NAKP oscillations can be alleviated with a simple modification of Eq. 1.24.

As ρ_A vanishes close to the nucleus, evaluation of the second term in Eq. 1.24 becomes unstable, leading to the aforementioned convergence problems. This is avoided by introducing a switching function that changes from the exact expression for the kinetic potential of subsystem A to the corresponding TF approximation near the nucleus,

$$\begin{aligned}
v_\mathrm{nad}[\rho_\mathrm{A},\rho_\mathrm{B};\mathbf{r}] &= \frac{2}{\rho_\mathrm{AB}(\mathbf{r})}\sum_{i=1}^{N_\mathrm{AB}/2}\left(-\frac{1}{2}\phi_i^\mathrm{AB}(\mathbf{r})\nabla^2\phi_i^\mathrm{AB}(\mathbf{r})-\epsilon_i\phi_i^\mathrm{AB}(\mathbf{r})^2\right) && (1.25)\\
&- \frac{2}{\rho_\mathrm{A}(\mathbf{r})}\sum_{i=1}^{N_\mathrm{A}/2}\left(-\frac{1}{2}\phi_i^\mathrm{A}(\mathbf{r})\nabla^2\phi_i^\mathrm{A}(\mathbf{r})-\epsilon_i^\mathrm{A}\phi_i^\mathrm{A}(\mathbf{r})^2\right)\times && (1.26)\\
&\quad (1-f[\rho_\mathrm{B};\mathbf{r}])-\left(\frac{5}{3}C_\mathrm{TF}\;\rho_\mathrm{A}^{2/3}\right)f[\rho_\mathrm{B};\mathbf{r}],
\end{aligned}$$

where $f[\rho_{\rm B}; \mathbf{r}]$ is the smooth switching function

$$f[\rho_{\rm B}; \mathbf{r}] = \frac{1}{e^{\kappa(-\rho_{\rm B}(\mathbf{r})+\rho'_{\rm B})} + 1}. \tag{1.27}$$

Previous work used a similar function to switch between approximate expressions for the NAKP in the vicinity of the nuclear cusp.[40] The parameters $\rho'_{\rm B}$ and κ determine the radial distance and the abruptness with which switching occurs, respectively. The parameter $\rho'_{\rm B}$ was related to the integrated electron density in the cusp region, setting $\rho'_{\rm B} = \rho_{\rm B}(r\prime)$, where

$$\xi = 4\pi \int_0^{r\prime} r^2 \rho_{\rm B}(r) dr. \tag{1.28}$$

e-DFT results obtained using range of values for κ and ξ were compared to determine robust parameters for the switching function. Setting $\kappa = 50$, we varied ξ over the range from 0.4 to 0.8 for Li and Ne^{7+}, which led to changes in the total calculated energy of less than 0.4 mH and 5 mH, respectively. Similarly, setting $\xi = 0.6$ and varying κ over the range from 50 to 500 led to differences of less than 0.1 mH for both Li and Ne.

Using the NAKP expression in Eq. 1.27 with $\xi = 0.6$ and $\kappa = 50$, our e-DFT protocol was applied to all four systems, and the results are presented in Table 1.2. All calculations reached full 10^{-8} convergence within 80 iterations of the KSCED equations, in contrast with the calculations using Eq. 1.24, which was difficult to converge in some cases even with 2000 iterations. Furthermore, the e-DFT calculations with the modified NAKP expression in Eq. 1.27 yields excellent accuracy in comparison to the full KS-DFT equations, with less than 1.5% error in the IE for all cases.

For the Li atom, Fig. 1.4 compares the NAKP, the KSCED effective potential, and the 2s electron density obtained by solving the KSCED equations using either Eq. 1.24 (black) or Eq. 1.27 (red) for the NAKP. The black curves in this figure are the same as those for Li in Figs. 1.2 and 1.3. It is clear from Fig. 1.4A that at short

Table 1.2: Total energy (TE) and ionization energy (IE) obtained using e-DFT with the NAKP switching function (Eq. 1.27).

Atom	TE	IE	Error (%)
$Q_{2.5}^{-0.5}$	-4.799142	0.059879	0.44
Li	-7.342720	0.199948	0.57
Ne^{7+}	-101.843497	8.632941	1.38
Be	-14.443703	-0.328383	1.00

distances, the switching function produces a relatively featureless, repulsive NAKP due to the TF approximation; the arrow in this figure indicates the radial distance r' that corresponds to the parameter $\xi = 0.6$. Fig. 1.4B illustrates that the repulsive NAKP largely cancels the attractive electron-nuclear Coulomb term in the KSCED effective potential (Eq. 1.5). As ρ_{A} vanishes at the nucleus, the KSCED effective potential must also approach zero.[30] The remaining oscillations at radial distances in Fig. 1.4B are an artifact of the finite basis set. Finally, Fig. 1.4C demonstrates that the 2s electron density that is obtained using the switching function does not reproduce the features of the radial node, but it recovers the exact embedding result for distances beyond 1 a.u. This close agreement at large distances is expected[41] from the accuracy of the IE calculations in Table 1.2. In light of the much improved convergence efficiency, use of the NAKP expression in Eq. 1.27 compares favorably with exact embedding via Eq. 1.24.

1.5 Extension to Larger Systems

The calculations reported here demonstrate a proof-of-principle for the exact calculation of the NAKP. However, for applications of e-DFT to large systems, performance of the ZMP extrapolation at each iteration of the KSCED equations is impractical. Nonetheless, the short-ranged nature of the NAKP (see Fig. 1.3E-H) suggests several strategies for employing our e-DFT protocol in larger systems.

For example, suppose that subsystem B is further divided into fragments (B_1, B_2,

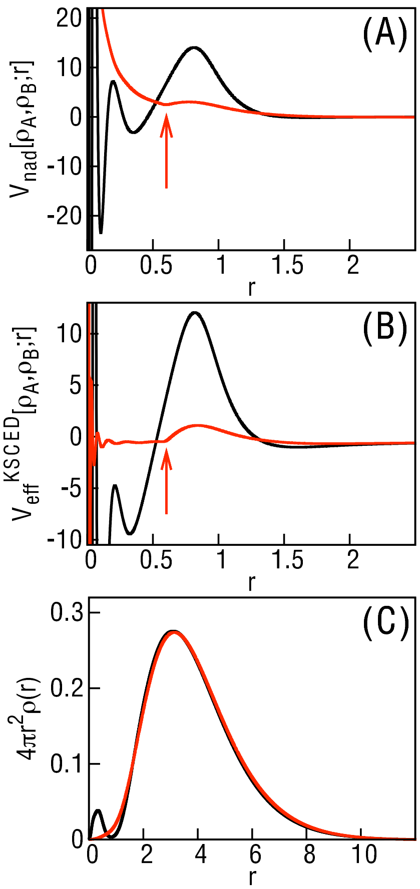

Figure 1.4: **(A)** The NAKP, **(B)** the KSCED effective potential, and **(C)** the 2s electron density (ρ_{A}) for the Li atom, obtained using exact embedding (black) and using the modified NAKP in Eq. 1.27 (red). The arrow indicates the radial distance at which switching occurs.

…, B_f), and consider the sum of the NAKP terms due to the individual fragments,

$$v_{\mathrm{nad}}[\rho_{\mathrm{A}}, \rho_{\mathrm{B}}; \mathbf{r}] \approx \sum_{i=1}^{f} \left(\frac{\delta T_{\mathrm{s}}[\rho]}{\delta \rho}\bigg|_{\rho=\rho_{\mathrm{A}}+\rho_{B_i}} - \frac{\delta T_{\mathrm{s}}[\rho]}{\delta \rho}\bigg|_{\rho=\rho_{\mathrm{A}}} \right). \tag{1.29}$$

This equation is exact in the limit of one fragment, and its implementation with our protocol will avoid ZMP extrapolation for anything larger than the union of subsystem A with a single fragment.

The assumption in Eq. 1.29 that the NAKP is additive among the fragments must be tested. However, any error introduced from this assumption can be partially corrected using the TF (or other) approximate kinetic energy functional,

$$
\begin{aligned}
v_{\mathrm{nad}}[\rho_{\mathrm{A}},\rho_{\mathrm{B}};\mathbf{r}] \approx{} & \left(\frac{\delta T_{\mathrm{s}}[\rho]}{\delta\rho}^{(\mathrm{appr})}\Bigg|_{\rho=\rho_{\mathrm{A}}+\rho_{\mathrm{B}}} - \frac{\delta T_{\mathrm{s}}[\rho]}{\delta\rho}^{(\mathrm{appr})}\Bigg|_{\rho=\rho_{\mathrm{A}}}\right) \\
& - \sum_{i=1}^{f}\left(\frac{\delta T_{\mathrm{s}}[\rho]}{\delta\rho}^{(\mathrm{appr})}\Bigg|_{\rho=\rho_{\mathrm{A}}+\rho_{B_i}} - \frac{\delta T_{\mathrm{s}}[\rho]}{\delta\rho}^{(\mathrm{appr})}\Bigg|_{\rho=\rho_{\mathrm{A}}}\right) \\
& + \sum_{i=1}^{f}\left(\frac{\delta T_{\mathrm{s}}[\rho]}{\delta\rho}^{(\mathrm{exact})}\Bigg|_{\rho=\rho_{\mathrm{A}}+\rho_{B_i}} - \frac{\delta T_{\mathrm{s}}[\rho]}{\delta\rho}^{(\mathrm{exact})}\Bigg|_{\rho=\rho_{\mathrm{A}}}\right). \qquad (1.30)
\end{aligned}
$$

Here, the first term on the RHS corresponds to the NAKP obtained from the TF functional for the full system. In the second term, the contribution due to each of the fragments using the TF approximation is removed, and in the third term, each of the fragment contributions is replaced using the exact protocol. The short-ranged nature of the NAKP suggests that distance-based cutoffs can be employed with summations in Eqs. 1.29 and 1.30, allowing for significant computational savings.

1.6 Conclusions

We have described a general and exact protocol for treating the non-additive kinetic potential in embedded density functional theory calculations. In applications to a series of three- and four-electron systems, we have numerically demonstrated the approach, and we have illustrated the qualitative failures that can arise from the use of approximate kinetic energy functionals. We have also shown that improved convergence of the KSCED equations can be obtained with appropriate switching of the NAKP in the vicinity of the nuclear cusps, and we have described possible strategies for the scalable implementation of our embedding protocol in large systems. Natural applications of exact embedding include the rigorous calculation of one-electron pseudopotentials, the calculation of DFT embedding potentials for use with high-level *ab initio* calculations on small subsystems,[5,21,42,43] and the accurate implementation of the “molecular embedding” strategy in which each molecule of a large system is assigned to a different embedded subsystem.[44]

1.7 Appendix: Unrestricted Open-Shell e-DFT

For unrestricted open-shell e-DFT calculations, the density of each subsystem is further partitioned into α and β spin densities, such that $\rho_{\mathrm{AB}} = \rho_{\mathrm{A}}^{\alpha} + \rho_{\mathrm{A}}^{\beta} + \rho_{\mathrm{B}}^{\alpha} + \rho_{\mathrm{B}}^{\beta}$. This leads to the KSCED equations

$$\left[-\frac{1}{2}\nabla^2 + V_{\mathrm{eff}}^{\mathrm{KSCED}}[\rho_{\mathrm{A}}^{\alpha}, \rho_{\mathrm{A}}^{\beta}, \rho_{\mathrm{B}}^{\alpha}, \rho_{\mathrm{B}}^{\beta}; \mathbf{r}]\right] \phi_i^{A,\alpha}(\mathbf{r}) = \epsilon_i^{A,\alpha}\phi_i^{A,\alpha}(\mathbf{r}) \qquad i = 1, ..., N_{\mathrm{A}}^{\alpha}, \quad (1.31)$$

$$\left[-\frac{1}{2}\nabla^2 + V_{\mathrm{eff}}^{\mathrm{KSCED}}[\rho_{\mathrm{A}}^{\beta}, \rho_{\mathrm{A}}^{\alpha}, \rho_{\mathrm{B}}^{\beta}, \rho_{\mathrm{B}}^{\alpha}; \mathbf{r}]\right] \phi_i^{A,\beta}(\mathbf{r}) = \epsilon_i^{A,\beta}\phi_i^{A,\beta}(\mathbf{r}) \qquad i = 1, ..., N_{\mathrm{A}}^{\beta}, \quad (1.32)$$

$$\left[-\frac{1}{2}\nabla^2 + V_{\mathrm{eff}}^{\mathrm{KSCED}}[\rho_{\mathrm{B}}^{\alpha}, \rho_{\mathrm{B}}^{\beta}, \rho_{\mathrm{A}}^{\alpha}, \rho_{\mathrm{A}}^{\beta}; \mathbf{r}]\right] \phi_i^{B,\alpha}(\mathbf{r}) = \epsilon_i^{B,\alpha}\phi_i^{B,\alpha}(\mathbf{r}) \qquad i = 1, ..., N_{\mathrm{B}}^{\alpha}, \quad (1.33)$$

$$\left[-\frac{1}{2}\nabla^2 + V_{\mathrm{eff}}^{\mathrm{KSCED}}[\rho_{\mathrm{B}}^{\beta}, \rho_{\mathrm{B}}^{\alpha}, \rho_{\mathrm{A}}^{\beta}, \rho_{\mathrm{A}}^{\alpha}; \mathbf{r}]\right] \phi_i^{B,\beta}(\mathbf{r}) = \epsilon_i^{B,\beta}\phi_i^{B,\beta}(\mathbf{r}) \qquad i = 1, ..., N_{\mathrm{B}}^{\beta}. \quad (1.34)$$

Here, N_{μ}^{ν} is the number of electrons in each subsystem, and $\rho_{\mu}^{\nu}(\mathbf{r}) = \sum_{i=1}^{N_{\mu}^{\nu}} |\phi_i^{\mu,\nu}(\mathbf{r})|^2$, where $\mu \in \{\mathrm{A}, \mathrm{B}\}$ and $\nu \in \{\alpha, \beta\}$. The KSCED effective potential, $V_{\mathrm{eff}}^{\mathrm{KSCED}}[\rho_{\mathrm{A}}^{\alpha}, \rho_{\mathrm{A}}^{\beta}, \rho_{\mathrm{B}}^{\alpha}, \rho_{\mathrm{B}}^{\beta}; \mathbf{r}]$, is

$$V_{\mathrm{eff}}^{\mathrm{KSCED}}[\rho_{\mathrm{A}}^{\alpha}, \rho_{\mathrm{A}}^{\beta}, \rho_{\mathrm{B}}^{\alpha}, \rho_{\mathrm{B}}^{\beta}; \mathbf{r}] = v_{\mathrm{ne}}(\mathbf{r}) + v_{\mathrm{J}}[\rho_{\mathrm{AB}}; \mathbf{r}] + v_{\mathrm{xc}}[(\rho_{\mathrm{A}}^{\alpha} + \rho_{\mathrm{B}}^{\alpha}), (\rho_{\mathrm{A}}^{\beta} + \rho_{\mathrm{B}}^{\beta}); \mathbf{r}] + v_{\mathrm{nad}}[\rho_{\mathrm{A}}^{\alpha}, \rho_{\mathrm{B}}^{\alpha}; \mathbf{r}] \quad (1.35)$$

where $v_{\mathrm{ne}}(\mathbf{r})$ and $v_{\mathrm{J}}[\rho_{\mathrm{AB}}; \mathbf{r}]$ are unchanged from Eq. 1.5, $v_{\mathrm{xc}}[(\rho_{\mathrm{A}}^{\alpha} + \rho_{\mathrm{B}}^{\alpha}), (\rho_{\mathrm{A}}^{\beta} + \rho_{\mathrm{B}}^{\beta}); \mathbf{r}]$ is the usual open-shell exchange-correlation potential for the total system,[8] and the NAKP is discussed below.

The kinetic energy functional is separable into two different spin contributions[8]

$$T_{\mathrm{s}}[\rho_{\mu}^{\alpha}, \rho_{\mu}^{\beta}] = T_{\mathrm{s}}[\rho_{\mu}^{\alpha}, 0] + T_{\mathrm{s}}[0, \rho_{\mu}^{\beta}], \quad (1.36)$$

where

$$T_{\mathrm{s}}[\rho_\mu^\alpha, 0] = \sum_{i=1}^{N_\mu^\alpha} \langle \phi_i^{\mu,\alpha} | -\frac{1}{2}\nabla^2 | \phi_i^{\mu,\alpha} \rangle \tag{1.37}$$

and likewise for $T_{\mathrm{s}}[0, \rho^\beta]$. Therefore, the NAKP depends only on spin densities corresponding to the same spin, such that

$$\begin{aligned} v_{\mathrm{nad}}[\rho_{\mathrm{A}}^\alpha, \rho_{\mathrm{B}}^\alpha; \mathbf{r}] &= \frac{\delta T_{\mathrm{s}}[\rho^\alpha, 0]}{\delta \rho^\alpha}\Big|_{\rho^\alpha = \rho_{\mathrm{A}}^\alpha + \rho_{\mathrm{B}}^\alpha}(\mathbf{r}) - \frac{\delta T_{\mathrm{s}}[\rho^\alpha, 0]}{\delta \rho^\alpha}\Big|_{\rho^\alpha = \rho_{\mathrm{A}}^\alpha}(\mathbf{r}), \text{ and} && (1.38) \\ v_{\mathrm{nad}}[\rho_{\mathrm{A}}^\beta, \rho_{\mathrm{B}}^\beta; \mathbf{r}] &= \frac{\delta T_{\mathrm{s}}[0, \rho^\beta]}{\delta \rho^\beta}\Big|_{\rho^\beta = \rho_{\mathrm{A}}^\beta + \rho_{\mathrm{B}}^\beta}(\mathbf{r}) - \frac{\delta T_{\mathrm{s}}[0, \rho^\beta]}{\delta \rho^\beta}\Big|_{\rho^\beta = \rho_{\mathrm{A}}^\beta}(\mathbf{r}). && (1.39) \end{aligned}$$

The ZMP extrapolation is used to calculate the KS spin orbitals $\{\phi_i^{\mathrm{AB},\nu}\}$ and eigenvalues $\{\epsilon_i^{\mathrm{AB},\nu}\}$ for the full system, exactly as is described in the text, except that the total spin density is employed instead of the total electron density. Finally, our exact expression for the NAKP for open-shell systems is modified from Eq. 1.24 as follows:

$$\begin{aligned} v_{\mathrm{nad}}[\rho_{\mathrm{A}}^\nu, \rho_{\mathrm{B}}^\nu; \mathbf{r}] &= \frac{1}{\rho_{\mathrm{AB}}^\nu(\mathbf{r})} \sum_i^{N_{\mathrm{A}}^\nu + N_{\mathrm{B}}^\nu} \left(-\frac{1}{2}\phi_i^{\mathrm{AB},\nu}(\mathbf{r})\nabla^2\phi_i^{\mathrm{AB},\nu}(\mathbf{r}) - \epsilon_i^{\mathrm{AB},\nu}\phi_i^{\mathrm{AB},\nu}(\mathbf{r})^2 \right) \\ &- \frac{1}{\rho_{\mathrm{A}}^\nu(\mathbf{r})} \sum_i^{N_{\mathrm{A}}^\nu} \left(-\frac{1}{2}\phi_i^{A,\nu}(\mathbf{r})\nabla^2\phi_i^{A,\nu}(\mathbf{r}) - \epsilon_i^{A,\nu}\phi_i^{A,\nu}(\mathbf{r})^2 \right). \end{aligned} \tag{1.40}$$

The TF approximation for the non-additive kinetic energy in an open-shell calculation is

$$T_{\mathrm{TF}}^{\mathrm{nad}}[\rho_{\mathrm{A}}^\nu, \rho_{\mathrm{B}}^\nu] = 2^{2/3} C_{\mathrm{TF}} \int \left(\rho_{\mathrm{AB}}^{\nu\,5/3}(\mathbf{r}) - \rho_{\mathrm{A}}^{\nu\,5/3}(\mathbf{r}) - \rho_{\mathrm{B}}^{\nu\,5/3}(\mathbf{r}) \right) d\mathbf{r}, \tag{1.41}$$

and corresponding result for the TFvW functional is

$$T_{\mathrm{TFvW}}^{\mathrm{nad}}[\rho_{\mathrm{A}}^\nu, \rho_{\mathrm{B}}^\nu] = T_{\mathrm{TF}}^{\mathrm{nad}}[\rho_{\mathrm{A}}^\nu, \rho_{\mathrm{B}}^\nu] + \frac{1}{72} \int \left(\frac{|\nabla \rho_{\mathrm{AB}}^\nu(\mathbf{r})|^2}{\rho_{\mathrm{AB}}^\nu(\mathbf{r})} - \frac{|\nabla \rho_{\mathrm{A}}^\nu(\mathbf{r})|^2}{\rho_{\mathrm{A}}^\nu(\mathbf{r})} - \frac{|\nabla \rho_{\mathrm{B}}^\nu(\mathbf{r})|^2}{\rho_{\mathrm{B}}^\nu(\mathbf{r})} \right) d\mathbf{r}. \tag{1.42}$$

Bibliography

[1] P. Cortona, Phys. Rev. B **44**, 8454 (1991).

[2] T. A. Wesolowski and A. Warshel, J. Phys. Chem. **97**, 8050 (1993).

[3] N. Govind, Y. A. Yang, A. J. R. da Silva, and E. A. Carter, Chem. Phys. Lett. **295**, 129 (1998).

[4] T. A. Wesolowski, *Computational Chemistry: Reviews of Current Trends*, edited by J. Leszczynski (World Scientific, Singapore, 2006), Vol. 10, 1-82.

[5] T. Klüner, N. Govind, Y. A. Yang, and E. A. Carter, J. Chem. Phys. **116**, 42 (2001).

[6] G. Hong, M. Strajbl, T. A. Wesolowski, and A. Warshel, J. Comp. Chem. **21**, 234110 (2000).

[7] M. Hodak, W. Lu, and J. Bernholc, J. Chem. Phys. **128**, 014101 (2008).

[8] R. G. Parr and W. Yang, *Density-Functional Theory of Atoms and Molecules* (Oxford University Press, New York, 1989).

[9] A. W. Götz, S. M. Beyhan, and L. Visscher, J. Chem. Theory Comput. **5**, 3161 (2009).

[10] T. A. Wesolowski, J. Chem. Phys. **106**, 8516 (1997).

[11] A. Lembarki and H. Chermette, Phys. Rev. A **50**, 5328 (1994).

[12] V. V. Karasiev, S. B. Trickey, and F. E. Harris, J. Comput.-Aided Mater. Des. **13**, 111 (2006).

[13] F. Tran and T. A. Wesolowski, Int. J. Quantum Chem. **89**, 441 (2002).

[14] C. R. Jacob and L. Visscher, J. Phys. Chem. **128**, 155102 (2008).

[15] S. M. Beyhan, A. W. Götz, C. R. Jacob, and L. Visscher, J. Chem. Phys. **132**, 044114 (2010).

[16] L. H. Thomas, Proc. Camb. Phil. Soc. **23**, 542 (1927).

[17] E. Fermi, Z. Phys. **48**, 73 (1928).

[18] C. F. von Weizsäcker, Z. Phys. **96**, 431 (1935).

[19] J. P. Perdew, J. Chevary, S. Vosko, K. A. Jackson, M. R. Pederson, D. Singh, and C. Fiolhais, Phys. Rev. B. **46**, 6671 (1992).

[20] A. D. Becke, J. Chem. Phys. **84**, 8 (1986).

[21] Y. A. Wang, N. Govind, and E. A. Carter, Phys. Rev. B **60**, 16350 (1999).

[22] J. A. Alonso and L. A Girifalco, Phys. Rev. B **17**, 3735-3743 (1978).

[23] P. García-González, J. E. Alvarellos, and E. Chacón, Phys. Rev. B **53**, 9509-9512 (1996).

[24] S. Fux, K. Kiewish, C. R. Jacob, J. Neugebauer, and M. Reiher, Chem. Phys. Lett. **461**, 353 (2008).

[25] M. Levy, Proc. Natl. Acad. Sci. USA **76**, 6062 (1979).

[26] Q. S. Zhao and R. G Parr, Phys. Rev. A **46**, 2337 (1992).

[27] Q. S. Zhao and R. G Parr, J. Chem. Phys. **98**, 543 (1993).

[28] Q. S. Zhao, R. C. Morrison, and R. G Parr, Phys. Rev. A **50**, 2138 (1994).

[29] R. A. King and N. C Handy, Phys. Chem. Chem. Phys. **2**, 5049-5056 (2000).

[30] C. R. Jacob, S. M. Beyhan, and L. Visscher, J. Chem. Phys. **126**, 234116 (2007).

[31] O. Roncero, M. P. de Lara-Castells, P. Villarreal, F. Flores, J. Ortega, M. Paniagua, and A. Aguado, J. Chem. Phys. **129**, 184104 (2008).

[32] O. Roncero, A. Zanchet, P. Villarreal, and A. Aguado, J. Chem. Phys. **131**, 234110 (2009).

[33] P. Huang and E. A. Carter, J. Chem. Phys. **125**, 084102 (2006).

[34] T. H. Dunning, J. Chem. Phys. **90**, 1007 (1989).

[35] J. C. Slater, Phys. Rev. **81**, 385-390 (1951).

[36] S. H. Vosko, L. Wilk, and M. Nusair, Can. J. Phys. **58**, 1200-1211 (1980).

[37] B. N. Papas and H. F. Schaefer, III, J. Mol. Struc.: THEOCHEM **768**, 175 (2006).

[38] M. R. Pederson and K. A. Jackson, Phys. Rev. B **41**, 7453 (1990).

[39] P. Pulay, Chem. Phys. Lett. **72**, 393 (1980).

[40] J. M. L. Lastra, J. W. Kaminski, and T. A. Wesolowski, J. Chem. Phys. **129**, 074107 (2008).

[41] D. J. Tozer and H. C. Handy, Molec. Phys. **101**, 2669 (2003).

[42] P. Huang and E. A. Carter, Annu. Rev. Phys. Chem. **59**, 261 (2008).

[43] S. Sharifzadeh, P. Huang, and E. A. Carter, Chem. Phys. Lett. **470**, 347 (2009).

[44] M. Iannuzzi, B. Kirchner, and J. Hutter, Chem. Phys. Lett. **421**, 16 (2005).

Vis

Chapter 2

Embedded density functional theory for covalently bonded and strongly interacting subsystems

2.1 Introduction

Important methodological challenges in electronic structure theory include the long-timescale simulation of *ab initio* molecular dynamics and the seamless combination of high- and low-level electronic structure methods in complex systems. Methods that exploit the intrinsic locality of molecular interactions have demonstrated encouraging progress towards these goals.[1–17]

In particular, orbital-free embedded DFT (e-DFT) offers a formally exact approach to electronic structure theory in which the interactions between subsystems are evaluated in terms of their electronic densities.[1–4] Recent work has demonstrated that constructing the embedded subsystems from individual molecules leads to a linear-scaling electronic structure approach that maps naturally onto distributed-memory parallel computers,[13,18] and it provides a systematic framework for calculating electronic excited states in condensed phase systems.[19,20] However, approximate treatments of the non-additive kinetic potential (NAKP) limit the accuracy of this approach in applications involving strongly interacting subsystems.[21] For example, severe artifacts in the structure of liquid water, including the complete absence of a second peak in the oxygen-oxygen radial distribution function, have been predicted from existing approximations to the NAKP,[18] and e-DFT applications involving covalently bonded embedded subsystems have also been shown to qualitatively fail.[21–23] The development of improved methods to address the NAKP problem will open new doors for on-the-fly, massively parallel electronic structure calculations in general, condensed-phase systems.

In this paper, we describe progress towards the development of accurate, scalable treatments for the NAKP in e-DFT. We provide the first molecular applications of our recently developed Exact Embedding (EE) method,[24] demonstrating that it successfully describes the breaking of covalent bonds and hydrogen bonds with chemical accuracy. Additionally, we introduce and numerically demonstrate a pairwise approximation to the NAKP, which allows for the scalable implementation of the EE method in large systems. Benchmark calculations are presented for systems with up to 125 molecules, demonstrating that parallel implementation of the method enables constant system-size scaling of the wall-clock calculation time.

2.2 Theory

2.2.1 Orbital-Free Embedded DFT

We utilize the orbital-free e-DFT formulation of Cortona[1] and Wesolowski and coworkers.[2,3] For the case in which the total electronic density ρ_{AB} is partitioned into two subsystems, $\rho_{\mathrm{AB}} = \rho_{\mathrm{A}} + \rho_{\mathrm{B}}$, the corresponding one-electron orbitals obey the Kohn-Sham Equations with Constrained Electron Density (KSCED),[3]

$$\left[-\frac{1}{2}\nabla^2 + v_{\mathrm{eff}}[\rho_{\mathrm{A}}, \rho_{\mathrm{AB}}; \mathbf{r}]\right] \phi_i^{\mathrm{A}}(\mathbf{r}) = \epsilon_i^{\mathrm{A}} \phi_i^{\mathrm{A}}(\mathbf{r}) \tag{2.1}$$

$$\left[-\frac{1}{2}\nabla^2 + v_{\mathrm{eff}}[\rho_{\mathrm{B}}, \rho_{\mathrm{AB}}; \mathbf{r}]\right] \phi_j^{\mathrm{B}}(\mathbf{r}) = \epsilon_j^{\mathrm{B}} \phi_j^{\mathrm{B}}(\mathbf{r}), \tag{2.2}$$

where $i = 1, \ldots, N^{\mathrm{A}}$, $j = 1, \ldots, N^{\mathrm{B}}$, and N^{A} and N^{B} are the number of electrons in the respective subsystems. v_{eff} is the effective potential for the coupled one-electron equations, such that

$$\begin{aligned} v_{\mathrm{eff}}[\rho_{\mathrm{A}}, \rho_{\mathrm{AB}}; \mathbf{r}] &= v_{\mathrm{ne}}(\mathbf{r}) + v_{\mathrm{J}}[\rho_{\mathrm{AB}}; \mathbf{r}] + v_{\mathrm{xc}}[\rho_{\mathrm{AB}}; \mathbf{r}] \\ &\quad + v_{\mathrm{nad}}[\rho_{\mathrm{A}}, \rho_{\mathrm{AB}}; \mathbf{r}], \end{aligned} \tag{2.3}$$

where the N_{nuc} nuclei occupy positions $\{\mathbf{R}_i\}$,

$$v_{\mathrm{ne}}(\mathbf{r}) = -\sum_{i}^{N_{\mathrm{nuc}}} \frac{Z_i}{|\mathbf{r} - \mathbf{R}_i|}, \tag{2.4}$$

$$v_{\mathrm{J}}[\rho; \mathbf{r}] = \int \frac{\rho(\mathbf{r}')}{|\mathbf{r}' - \mathbf{r}|} d\mathbf{r}', \tag{2.5}$$

$$v_{\mathrm{xc}}[\rho; \mathbf{r}] = \left[\frac{\delta E_{\mathrm{xc}}[\rho]}{\delta \rho}\right](\mathbf{r}), \tag{2.6}$$

and $E_{\mathrm{xc}}[\rho]$ is the exchange-correlation functional. $v_{\mathrm{nad}}[\rho_{\mathrm{A}}, \rho_{\mathrm{AB}}; \mathbf{r}]$ is the potential due to the non-additive kinetic energy for non-interacting electrons, such that

$$v_{\mathrm{nad}}[\rho_{\mathrm{A}}, \rho_{\mathrm{AB}}; \mathbf{r}] = \left[\frac{\delta T_{\mathrm{s}}^{\mathrm{nad}}[\rho_{\mathrm{A}}, \rho_{\mathrm{B}}]}{\delta \rho_{\mathrm{A}}}\right](\mathbf{r}), \tag{2.7}$$

where $T_{\mathrm{s}}^{\mathrm{nad}}[\rho_{\mathrm{A}}, \rho_{\mathrm{B}}] \equiv T_{\mathrm{s}}[\rho_{\mathrm{AB}}] - T_{\mathrm{s}}[\rho_{\mathrm{A}}] - T_{\mathrm{s}}[\rho_{\mathrm{B}}]$. The subsystem densities are constructed from the corresponding KS orbitals, using $\rho_{\mathrm{A}}(\mathbf{r}) = \sum_{i=1}^{N^{\mathrm{A}}} |\phi_i^{\mathrm{A}}(\mathbf{r})|^2$ and $\rho_{\mathrm{B}}(\mathbf{r}) = \sum_{j=1}^{N^{\mathrm{B}}} |\phi_j^{\mathrm{B}}(\mathbf{r})|^2$. Eqs. 3.1-2.7 are easily generalized for the e-DFT description of multiple embedded subsystems.[1,18]

Two aspects of e-DFT are worth emphasizing. Firstly, like conventional Kohn-Sham (KS)-DFT, it is a theory that is exact in principle, but practical calculations must employ approximations to the unknown exchange-correlation functional. Secondly, unlike conventional KS-DFT calculations, the embedding formulation introduces the NAKP, $v_{\mathrm{nad}}[\rho_{\mathrm{A}}, \rho_{\mathrm{AB}}; \mathbf{r}]$, since the one-electron orbitals for subsystem A are not necessarily orthogonal to those of subsystem B. Without knowledge of the exact functional for the non-interacting kinetic energy, this creates a second source of approximation in e-DFT calculations. The significance of the NAKP is system-dependent, with the most severe cases including those for which the subsystem densities greatly overlap; no approximate kinetic energy functional has been previously demonstrated to yield accurate results for embedded subsystems that are connected by covalent bonds.[3,21,22,25,26]

2.2.2 Exact Calculations of NAKP

We have recently developed the Exact Embedding (EE) method to calculate the NAKP.[24] The general method can be summarized for two embedded subsystems as follows: A Levy constrained search (LCS)[27] or equivalent technique is first used to determine the full set of orthogonal KS orbitals, $\{\phi_i^{\mathrm{AB}}\}$, that correspond to the total density ρ_{AB} from the latest iteration of Eqs. 3.1-2.3. Then, from the KS orbitals $\{\phi_i^{\mathrm{AB}}\}$, $\{\phi_i^{\mathrm{A}}\}$, and $\{\phi_i^{\mathrm{B}}\}$, the corresponding kinetic potentials are calculated using the exact result of King and Handy,[28]

$$v_{T_{\mathrm{s}}}(\mathbf{r}) = \frac{\sum_{i=1}^{n}(-\frac{1}{2}\phi_i(\mathbf{r})\nabla^2\phi_i(\mathbf{r})) - \epsilon_i\phi_i(\mathbf{r})^2)}{\rho(\mathbf{r})} + \mu, \tag{2.8}$$

where n is the number of occupied orbitals, ϵ_i is the KS eigenvalue corresponding to orbital ϕ_i, and μ is a constant. Finally, the NAKP needed for the next iteration of Eqs. 3.1-2.3 is calculated directly from the difference

$$v_{\mathrm{nad}}[\rho_{\mathrm{A}}, \rho_{\mathrm{AB}}; \mathbf{r}] = v_{T_{\mathrm{s}}}^{\mathrm{AB}}(\mathbf{r}) - v_{T_{\mathrm{s}}}^{\mathrm{A}}(\mathbf{r}), \tag{2.9}$$

where the superscripts in this equation indicate the orbital set to which each kinetic potential corresponds.

Rather than explicitly performing the LCS, we use the equivalent protocol of Zhao, Morrison, and Parr (ZMP)[29–31] to obtain the exact non-interacting kinetic energy and the KS orbitals $\{\phi_i^{\mathrm{AB}}\}$. This requires solution of the following one-electron equations

$$\left[-\frac{1}{2}\nabla^2 + v_{\mathrm{ext}}(\mathbf{r}) + v_{\mathrm{c}}^{\lambda}(\mathbf{r})\right]\phi_{i,\lambda}^{\mathrm{AB}}(\mathbf{r}) = \epsilon_{i,\lambda}^{\mathrm{AB}}\phi_{i,\lambda}^{\mathrm{AB}}(\mathbf{r}) \tag{2.10}$$

in the limit $\lambda \to \infty$, where $i = 1, \ldots, (N^{\mathrm{A}} + N^{\mathrm{B}})$, and

$$v_{\mathrm{c}}^{\lambda}(\mathbf{r}) = \lambda \int \frac{\rho(\mathbf{r}') - \rho_{\mathrm{AB}}(\mathbf{r})}{|\mathbf{r}' - \mathbf{r}|} d\mathbf{r}'. \tag{2.11}$$

$v_{\mathrm{ext}}(\mathbf{r})$ corresponds to any well-behaved external potential,[30,31] and various choices for this potential are described in Sec. III B. In practice, Eq. 2.10 is solved at several large, finite values of λ, and the KS orbitals and eigenvalues, as well as the final non-interacting kinetic energy, are obtained via extrapolation.[29–31] In Sec. V, we discuss a technique to robustly implement the ZMP step for NAKP calculations in large systems.

The EE method outlined in Eqs. 2.8 - 2.11 is unique in that it allows for the formally exact calculation of the total electronic density within the e-DFT framework, using integer orbital occupancies and without approximations to the NAKP. The method was previously demonstrated for atomic systems with strongly overlapping subsystem densities,[24] and the current paper presents its first molecular applications. We note that several other groups have also used density inversion techniques to calculate the NAKP, assuming that the total electron density is already available from another electronic structure calculation.[23,32,33] In particular, Visscher and coworkers have applied this approach to molecular systems with the aim of developing improved non-additive kinetic energy functionals.[23] Furthermore, Partition DFT has been introduced as a formally exact embedding scheme in which subsystem densities are described using partially occupied orbitals, and it has been applied to one-dimensional model systems.[6]

2.3 Implementation Details

We have implemented e-DFT in the Molpro quantum chemistry package,[34] allowing for calculation of the NAKP with either approximate functionals or the EE method. In this section, methodological and numerical aspects of the implementation are discussed.

2.3.1 Supermolecular vs. Monomolecular Basis Sets

The atom-centered basis sets used to solve the KSCED (Eqs. 3.1 and 3.2) are implemented using two different conventions.[21,35] In the monomolecular basis set convention, the density for each embedded subsystem is described using only the basis functions that are centered on atoms belonging to that subsystem. In the supermolecular basis set convention, the density for each embedded subsystem is described using the same basis set, which includes functions that are centered on all atoms in the system. The supermolecular basis set convention provides a closer approximation to the complete basis set limit, although it is more costly.

2.3.2 ZMP Step

In our implementation, the ZMP step of the EE method is performed by solving Eq. 2.10 for six large, finite values of λ. The KS orbitals $\{\phi_i^{\mathrm{AB}}\}$ are then obtained from extrapolation of the atomic orbital coefficients for the $\{\phi_{i,\lambda}^{\mathrm{AB}}\}$, using a third-order polynomial in λ^{-1}, and normalization of the extrapolated orbitals is enforced *a posteriori*. The KS eigenvalues $\{\epsilon_i^{\mathrm{AB}}\}$ are similarly obtained from extrapolation of the $\{\epsilon_{i,\lambda}^{\mathrm{AB}}\}$. $T_{\mathrm{s}}[\rho_{\mathrm{AB}}]$ is calculated analytically from the extrapolated orbital coefficients, which ensures that the total energy from the EE method is bound from below by the KS-DFT energy.

In the limit $\lambda \to \infty$, the solutions to Eq. 2.10 are independent of the choice of external potential $v_{\mathrm{ext}}(\mathbf{r})$,[29–31] although $v_{\mathrm{ext}}(\mathbf{r})$ does effect the convergence with increasing λ. Various options where thus considered, including

$$v_{\mathrm{ext}}(\mathbf{r}) = v_{\mathrm{ne}}(\mathbf{r}), \tag{2.12}$$

$$v_{\mathrm{ext}}(\mathbf{r}) = v_{\mathrm{ne}}(\mathbf{r}) + \left(1 - \frac{1}{N^{\mathrm{A}} + N^{\mathrm{B}}}\right) v_{\mathrm{J}}[\rho_{\mathrm{AB}}; \mathbf{r}], \tag{2.13}$$

$$v_{\mathrm{ext}}(\mathbf{r}) = v_{\mathrm{ne}}(\mathbf{r}) + v_{\mathrm{J}}[\rho_{\mathrm{AB}}; \mathbf{r}] + v_{\mathrm{xc}}[\rho_{\mathrm{AB}}; \mathbf{r}]. \tag{2.14}$$

At every iteration of the KSCED, these versions of $v_{\mathrm{ext}}(\mathbf{r})$ are all available without the need for additional computation. Test calculations have indicated that the external potential in Eq. 2.14 leads to the fastest convergence of the extrapolation with increasing λ, and this potential is used in all results for the EE method reported here.

2.3.3 NAKP Numerics for Regions of Weak Density Overlap

Numerical evaluation of the kinetic potential from Eq. 2.8 is unstable in regions for which the corresponding density vanishes. The problem is exacerbated by the incorrect distance dependence of the low-density tails obtained from calculations using Gaussian-type orbitals (GTOs).[28] However, these numerically treacherous regions correspond to weak overlap between subsystem densities, where the magnitude of the NAKP is necessarily small and easily approximated.[2] We thus utilize a density-based criterion to switch from the exact expression for the kinetic potential to a numerically stable approximation, such as the Thomas-Fermi (TF) kinetic potential. The protocol used to perform this switching is described below.

In a first step, we calculate the constant shift that is needed to match the exact result for each kinetic potential to the corresponding TF result in a prescribed switching region. Specifically, for each of the kinetic potentials (i.e., $v_{T_{\mathrm{s}}}(\mathbf{r}) \in \left\{v_{T_{\mathrm{s}}}^{\mathrm{AB}}(\mathbf{r}), v_{T_{\mathrm{s}}}^{\mathrm{A}}(\mathbf{r}), v_{T_{\mathrm{s}}}^{\mathrm{B}}(\mathbf{r})\right\}$ which correspond, respectively, to $\rho(\mathbf{r}) \in \{\rho_{\mathrm{AB}}(\mathbf{r}), \rho_{\mathrm{A}}(\mathbf{r}), \rho_{\mathrm{B}}(\mathbf{r})\}$), the average difference ($\Delta \in \left\{\Delta^{\mathrm{AB}}, \Delta^{\mathrm{A}}, \Delta^{\mathrm{B}}\right\}$) between the results from Eq. 2.8 and from the TF functional is evaluated in the vicinity of the $\rho(\mathbf{r}) = \rho'$ density isosurface. Each Δ is computed over gridpoints in the region $\xi < f[\rho; \mathbf{r}] < (1 - \xi)$, where

$$f[\rho; \mathbf{r}] = \frac{1}{e^{\kappa(\rho(\mathbf{r}) - \rho')} + 1}, \tag{2.15}$$

ξ, κ, and ρ' are parameters that define the switching region, and the relative contribution from each gridpoint is weighted according to

$$\omega[\rho; \mathbf{r}] = e^{-\kappa(\rho_{\mathrm{AB}}(\mathbf{r}) - \rho(\mathbf{r}))}. \tag{2.16}$$

Note that the weighting function in Eq. 2.16 is uniform for the case of $\rho = \rho_{\mathrm{AB}}$, and it preferentially selects values which $\rho(\mathbf{r}) \approx \rho_{\mathrm{AB}}(\mathbf{r})$ for the cases in which $\rho(\mathbf{r})$ is one of the subsystem densities.

In a second step, each kinetic potential is computed on the grid; this is done by vertically shifting the exact result with the corresponding Δ and then smoothly switching to the TF result at densities below ρ', using the density-based switching function $f[\rho; \mathbf{r}]$ in Eq. 2.15. Finally, the NAKP is calculated from the smoothly switched kinetic potentials using Eq. 2.9. The vertical shifts that are applied to kinetic potentials simply give rise to an additive constant in the final NAKP, which has no physical effect. Although we find that switching to the TF functional at low densities is both convenient and accurate, the protocol described above could be performed using any approximate kinetic energy functional.

2.4 Results: Small Systems

2.4.1 Calculation Details

In this section, e-DFT calculations are presented for the dissociation curves of $(H_2O)_2$ and the covalently bound Li^+-Be and CH_3-CF_3 molecules; standard KS-DFT calculations are included for comparison. All results are obtained using the Molpro quantum chemistry package,[34] with KS-DFT available in the standard version and with the e-DFT method implemented in our modified version. In the e-DFT calculations, the NAKP is described using either the EE method or the approximate TF[36,37] and LC94[38] kinetic energy functionals; these approaches will hereafter be referred to as e-DFT-EE, e-DFT-TF, and e-DFT-LC, respectively.

All calculations in this section are performed using the B88-P86 exchange-correlation (XC) functional.[39,40] Both the XC functional and the NAKP are evaluated on a grid of Becke-Voronoi[41] cells with resolution to limit the integration error of Slater exchange to 10^{-12} Hartree; the grid is generated using the Molpro directive GRID=10^{-12}.

The KSCED in Eqs. 3.1-3.2 are initialized from the gas phase density of each subsystem, and the eigensolutions for each set of equations are updated at every iteration. Convergence of these equations is improved with the molecular orbital (MO) shifting and direct inversion of iterative subspace (DIIS) algorithms.[42,43] For the water dimer, an MO shift of -0.5 Hartree is employed, whereas a -1.0 Hartree shift is used for Li^+-Be and CH_3-CF_3. Since the DIIS algorithm leads to slow final convergence,[44] it is discontinued once the root mean squared difference (RMSD) of total density matrix elements changes by less than 5×10^{-4} between two successive iterations. The KSCED equations are deemed converged when the total energy of the system changes by less than 10^{-6} Hartree and the RMSD in the total density matrix is smaller than 10^{-5} between two successive iterations.

For the ZMP step, extrapolation of the solutions to Eq. 2.10 is performed using $\lambda = \gamma + \tau j$, where $j = 0, 1, \ldots, 5$. Unless otherwise noted, calculations for the water dimer and Li^+-Be employ $\gamma = 5000$ and $\tau = 100$, whereas calculations for CH_3-CF_3 employ $\gamma = 100$ and $\tau = 10$. To reach adequate convergence, Eq. 2.10 is solved in several stages. Firstly, a coarse solution is reached by using an MO shift of -10^3 Hartree and a value of $\lambda = 100$. Subsequently, using this coarse solution as a starting point, the Eq. 2.10 solved using a smaller MO shift of -84 Hartree and with $\lambda = \gamma$. Finally, solution of Eq. 2.10 for each increasing value of λ needed for extrapolation employs the solution for the prior value of λ as a starting point. The DIIS algorithm is used throughout. The orbitals from Eq. 2.10 are deemed converged when the RMSD in the density matrix was smaller than 10^{-9} between two successive iterations; significantly tighter convergence is needed for the ZMP equations than for the KSCED, to ensure an accurate extrapolation.

Calculations for the water dimer variously employ the aug-pc-3, aug-pc-2, and aug-pc-1 basis sets,[45] in each case using only the s- and p-type functions for the hydrogen atoms and the s-, p-, and d-type functions for the oxygen atoms. These water dimer basis sets are hereafter referred to as the modified aug-pc-3, aug-pc-2, and aug-pc-1 basis sets, respectively. In all calculations for Li^+-Be and CH_3-CF_3, the Li, Be, and C atoms are described using the s-, p-, and d-type functions of the combined aug-pc-4 and, for Li and Be, the cc-pVQZ (core/valence), for C, the cc-pV6Z (core/valence) basis sets,[46] and the H and F atoms are described using the full aug-pc-1 basis set.[45] Sensitivity of the e-DFT calculations to the basis set is discussed in the next section.

Larger basis sets provide a better description of low-density regions, allowing for the use of smaller values for the parameter ρ' in Eqs. 2.15 and 2.16 and providing robustness with respect to the choice of this parameter. For the water dimer, calculations using aug-pc-3, aug-pc-2, and aug-pc-1 basis sets employ values of $\rho' =$

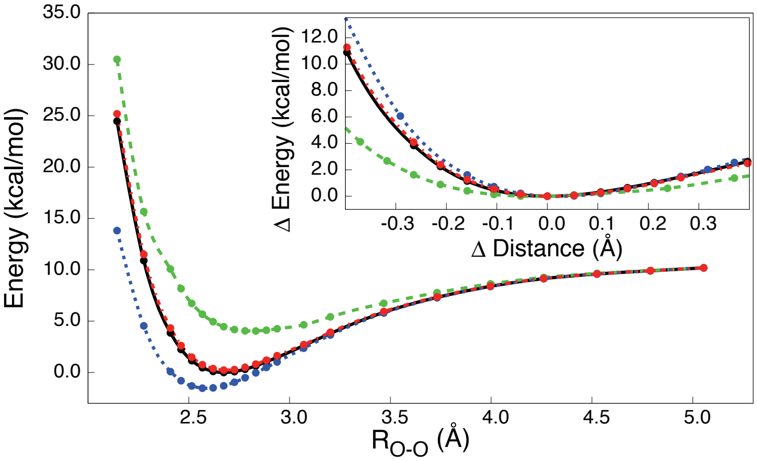

Figure 2.1: The water dimer dissociation curve, obtained using e-DFT-EE (red, dot-dashed), e-DFT-TF (green, dashed) and e-DFT-LC (blue, dotted). Also included are reference KS-DFT results (black, solid), which are graphically indistinguishable from the e-DFT-EE results. Total energies are plotted with respect to the KS-DFT minimum of -152.430722 Hartree. Inset, the curves are shifted vertically to align the energy minima and horizontally to align the equilibrium distances.

$10^{-5}, 10^{-4}$, and 5×10^{-3}, respectively. For Li^+-Be and CH_3-CF_3, calculations employ $\rho' = 10^{-6}$. In each case, the parameter κ in Eqs. 2.15 and 2.16 is chosen such that $\kappa\rho' = 10$ and $\xi = 10^{-4}$.

2.4.2 Water Dimer

Fig. 2.1 presents the dissociation curve for the water dimer, a system with a strong hydrogen bond and significantly overlapping subsystem densities. The curve is obtained using e-DFT-EE (dot-dashed), e-DFT-TF (dashed), and e-DFT-LC (dotted); KS-DFT results (solid) are also included for reference. The e-DFT calculations were performed using two embedded subsystems, each corresponding to a different molecule in the dimer. All calculations presented in the figure utilize the modified aug-pc-3 basis set, with the e-DFT calculations employing the supermolecular basis set convention. The dissociation curve is plotted as a function of the oxygen-oxygen distance, with the equilibrium water dimer geometry obtained from a KS-DFT energy minimization and with other geometries obtained by displacing the two molecules along the oxygen-oxygen vector while fixing all other internal coordinates.

The e-DFT-EE results in Fig. 2.1 agree well with KS-DFT throughout the range of dissociation distances. Numerical results for the two methods are graphically indistinguishable, and the calculated total energies differ by less than 0.5 kcal/mol throughout the entire attractive branch of the curve. Exact numerical agreement between the e-DFT-EE and KS-DFT descriptions is expected only in the limits of an exact XC functional and a complete basis set.

The sensitivity of the e-DFT results to approximations in the NAKP is clearly demonstrated in Fig. 2.1. The curve obtained using e-DFT-TF differs significantly from the KS-DFT reference, exhibiting a dissociation energy that is underestimated by 40% (∼4 kcal/mol) and an equilibrium bond length that is 0.15 Å too long. Calculations obtained using e-DFT-LC are somewhat improved, although the dissociation energy is still overestimated by 20% (∼2 kcal/mol) and the equilibrium bond length is underestimated by 0.10 Å. In the inset of Fig. 2.1, the curvature of the potential energy surfaces in the vicinity of the minimum are compared, revealing significant deviations of the results obtained using the approximate NAKP treatments (e-DFT-TF and e-DFT-LC) with respect to the results obtained using KS-DFT and e-DFT-EE.

Iannuzzi and coworkers[18] have demonstrated that e-DFT calculations using approximate treatments of the NAKP, including the TF and LC94 functionals, lead to qualitative failure in describing the structure of liquid water. Fig. 2.1 illustrates the origin of this failure in terms of the pairwise interactions among molecules, and it suggests that e-DFT-EE will enable the accurate, first-principles simulation of liquid water and aqueous solutions. Critical to this effort, however, is the efficient and parallelizable implementation of the EE method for large systems, which is discussed in Section V.

The sensitivity of the e-DFT calculations to basis set completeness is illustrated in

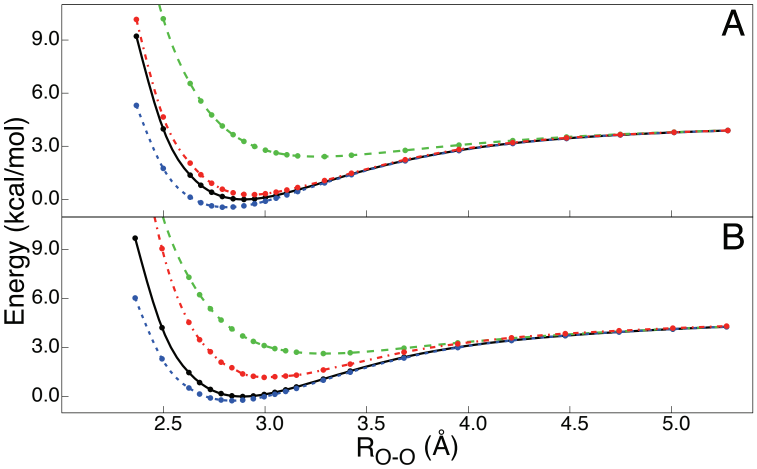

Figure 2.2: Basis set dependence of the water dimer dissociation curve, illustrated for calculations using the **(A)** modified aug-pc-2 and **(B)** modified aug-pc-1 basis sets. Results for the e-DFT-EE, e-DFT-TF, e-DFT-LC, and KS-DFT methods are reported as in Fig. 2.1. Total energies are plotted with respect to the KS-DFT minimum energies of -152.953947 Hartree (panel A) and -152.864441 Hartree (panel B).

Fig. 2.2, in which the water dimer dissociation curves are recalculated using the modified aug-pc-2 (Fig. 2.2A) and modified aug-pc-1 basis sets (Fig. 2.2B). Comparison of the KS-DFT results and the e-DFT-EE results reveals that the agreement between the methods worsens with smaller basis set; of course, both the KS-DFT calculations and the e-DFT-EE calculations are basis-set dependent. In the e-DFT-EE calculations, smaller basis sets give rise to numerical artifacts including the oscillatory behavior in the King-Handy expression for the kinetic potential.[28] For the modified aug-pc-1 basis set (Fig. 2.2B), the reasonable agreement between KS-DFT and e-DFT-LC is due to a fortuitous cancellation of errors from the approximate NAKP functional and small basis set.

2.4.3 Li^+-Be

We now consider the heterolytic cleavage of a weak covalent bond, Li^+-Be→Li^++Be, using KS-DFT and e-DFT. The e-DFT calculations were performed in the supermolecular basis set convention using two embedded subsystems, one corresponding

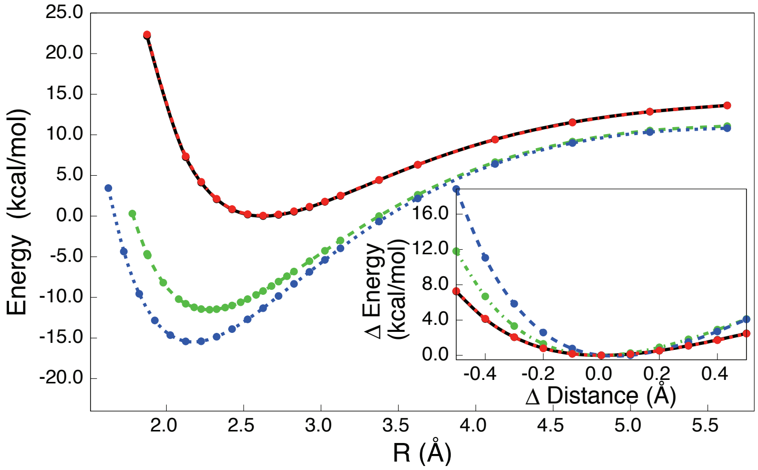

Figure 2.3: The Li$^+$-Be dissociation curve. Results for the e-DFT-EE, e-DFT-TF, e-DFT-LC, and KS-DFT methods are reported as in Fig. 2.1. The results for e-DFT-EE and the reference KS-DFT results are graphically indistinguishable. Total energies are plotted with respect to the KS-DFT minimum energy of -21.962072 Hartree. Inset, the curves are aligned as in the inset of Fig. 2.1.

to the 2-electron Li ion and the other corresponding to the 4-electron Be atom. The dissociation curve for Li$^+$-Be is plotted in Fig. 2.3.

As is seen from the main figure, the e-DFT-EE calculations accurately reproduce the calculated total energies from KS-DFT throughout the entire range of internuclear distances. The dissociation curves for these two methods, which are graphically indistinguishable in Fig. 2.3, deviate by less than 0.2 kcal/mol throughout the range of separations and the dissociation energy deviates by only 0.07 kcal/mol. In contrast, the e-DFT-TF results are in qualitative disagreement with the KS-DFT reference calculations; in addition to dramatically overestimating the dissociation energy of the molecule by ∼12.5 kcal/mol, the method predicts the equilibrium bond length to be 20% too short. Interestingly, the e-DFT-LC method performs significantly worse in this application. The calculations based on the approximate LC94 kinetic energy functional overestimate the dissociation energy by ∼16 kcal/mol and predict the equilibrium bond length to be 25% too short. The inset to Fig. 2.3 illustrates that both e-DFT methods that use approximate treatments for the NAKP lead to an overestimation of the energy surface curvature in the vicinity of the equilibrium bond distance.

The results in Fig. 2.3 illustrate the well-known breakdown of e-DFT with approximate treatments of the NAKP for applications involving strongly overlapping subsystem densities. They further show that our EE method overcomes this large error, yielding the first numerical demonstration of an e-DFT method to describe covalent bond-breaking with chemical accuracy. Since e-DFT-EE is a formally exact method, this result is expected. However demonstration that the level of accuracy in Fig. 2.3 can be achieved in practical numerical simulations constitutes a non-trivial validation of the method.

2.4.4 CH_3-CF_3

In a more challenging application for e-DFT, we consider the heterolytic cleavage of a strong carbon-carbon σ-bond, CH_3-$CF_3 \rightarrow CH_3^+ + CF_3^-$. The e-DFT calculations were again performed in the supermolecular basis set convention using two embedded subsystems, one corresponding to the 8-electron CH_3^+ moiety and the other corresponding to the 34-electron CF_3^- moiety. The geometry for the lowest energy point along the curve is provided in the supplemental information; the dissociation curve in Fig. 2.4 is plotted by extending the C-C distance keeping all other internal coordinates unchanged.

The dissociation curves in Fig. 2.4 are presented only for e-DFT-EE and the reference KS-DFT calculations. e-DFT-EE reproduces the KS-DFT reference value for the total energy for the molecule at the equilibrium bond distance to within 1.5 kcal/mol, and the embedding method also recovers the reference value for the equilibrium bond distance. Furthermore, as is clear from the inset, e-DFT-EE accurately reproduces the curvature of the energy surface in the vicinity of the equilibrium bond distance. In contrast, the e-DFT-TF and e-DFT-LC descriptions for this system fail dramatically,

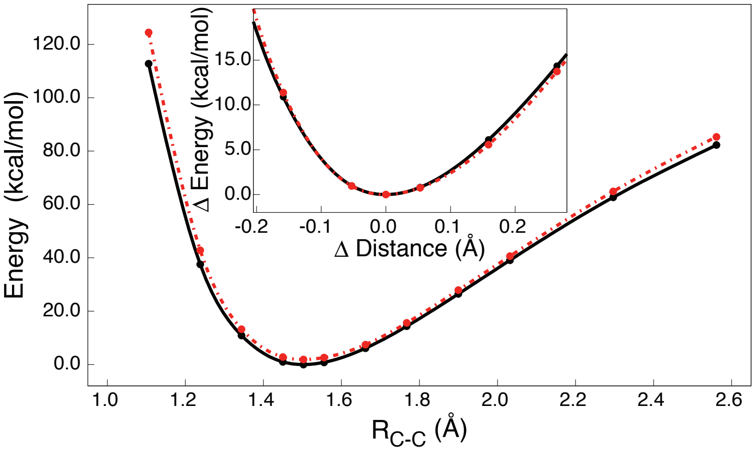

Figure 2.4: The CH_3-CF_3 dissociation curve for heterolytic cleavage of the C-C bond. Results are presented for the e-DFT-EE (red, dot-dashed) and KS-DFT (black, solid) methods. Total energies are plotted with respect to the KS-DFT minimum energy of -377.575687 Hartree. Inset, the curves are aligned as in the inset of Fig. 2.1.

predicting total energies at the equilibrium bond distance that deviate from the KS-DFT reference by 731 kcal/mol and 981 kcal/mol, respectively. For calculations with such strongly interacting subsystems, the failure of e-DFT with approximate descriptions for the NAKP methods has been previously observed.[21] However, the results for e-DFT-EE in Fig. 2.4 demonstrate significant progress in the accurate description of covalently interacting subsystems using e-DFT.

2.5 Results: Extension to Larger Systems

2.5.1 Pairwise Treatment of the NAKP

In the previously described implementation of e-DFT-EE, the ZMP step, or an equivalent LCS, is performed on the full system of interest. However, numerical challenges limit the LCS to systems with less than 10-15 atoms,[32,33,47–50] potentially hindering the applicability of e-DFT-EE in large systems. To avoid this problem, we demonstrate an pairwise approximation for the NAKP that enables the scalable implementation of e-DFT-EE.

For a system composed of $N_{\rm sub}$ embedded subsystems, $\{\rho_\alpha\}$, the non-additive kinetic energy can be approximated using a pairwise sum,[24] such that

$$\begin{aligned} T_s^{\rm nad}[\{\rho_\alpha\}] &\equiv T_s[\bar{\rho}] - \sum_{\alpha=1}^{N_{\rm sub}} T_s[\rho_\alpha] \\ &\approx \sum_{\alpha<\beta=1}^{N_{\rm sub}} \left(T_s[\rho_\alpha+\rho_\beta] - T_s[\rho_\alpha] - T_s[\rho_\beta]\right), \end{aligned} \tag{2.17}$$

where $\bar{\rho} = \sum_{\alpha=1}^{N_{\rm sub}} \rho_\alpha$. The NAKP for a given subsystem α is then

$$v_{\rm nad}[\rho_\alpha, \{\rho_\alpha\}; \mathbf{r}] = \sum_{\beta\neq\alpha}^{N_{\rm sub}} (v_{T_{\rm s}}^{\alpha\beta}(\mathbf{r}) - v_{T_{\rm s}}^{\alpha}(\mathbf{r})). \tag{2.18}$$

Applying the EE method to this approximation for the NAKP, a ZMP step is performed at each iteration of the KSCED to obtain the KS orbitals corresponding to each pair of subsystems densities, $\{\phi_i^{\alpha\beta}\}$. Then, using both the subsystem KS orbitals $\{\phi_i^\alpha\}$ from the KSCED and the subsystem-pair KS orbitals $\{\phi_i^{\alpha\beta}\}$, the NAKP is evaluated directly from Eqs. 2.8 and 2.18. In this approach, only the NAKP is assumed to be pairwise additive; all other interactions in the system are treated with full generality. Since the ZMP step is applied only to the subsystem pairs, this approach is numerically feasible if each subsystem is limited to a relatively small number of atoms, regardless of the total system size. The short-ranged nature of contributions to the non-additive kinetic energy suggests that distance-based cutoffs can be employed within the sum over subsystem pairs.[24]

It was emphasized earlier that the converged results of the ZMP step are independent of the choice of external potential, $v_{\rm ext}(\mathbf{r})$, in Eq. 2.10. In the pairwise implementation of e-DFT-EE for the water trimer in Sec. V B, we employ the following external potential for each pair of densities ρ_α and ρ_β,

$$\begin{aligned} v_{\mathrm{ext}}(\mathbf{r}) &= v_{\mathrm{ne}}(\mathbf{r}) + v_{\mathrm{J}}[\bar{\rho};\mathbf{r}] + v_{\mathrm{xc}}[\bar{\rho};\mathbf{r}] \\ &\quad + \frac{\delta \tilde{T}_{\mathrm{s}}[\bar{\rho}]}{\delta(\rho_\alpha + \rho_\beta)} - \frac{\delta \tilde{T}_{\mathrm{s}}[\rho_\alpha + \rho_\beta]}{\delta(\rho_\alpha + \rho_\beta)}, \end{aligned} \tag{2.19}$$

where $\tilde{T}_{\mathrm{s}}$ indicates the approximate TF functional. This external potential approximates the KSCED effective potential (Eq. 2.3) for the pair of subsystems embedded within the remainder of the full system; note that the TF functional is used only to regularize the effective potential for the ZMP step; it does not introduce any additional approximation into the e-DFT-EE calculation. In Sec. V C, we use a simple external potential that includes only the electron-nuclear interactions for the subsystem pair.

The following two sections demonstrate the accuracy of this pairwise implementation of e-DFT-EE (Sec. V B) and the efficiency with which it can be implemented in parallel (Sec. V C).

2.5.2 Water Trimer Application: Testing Pairwise Additivity in the NAKP

Fig. 2.5 presents a test of pairwise additivity in the NAKP (Eq. 2.18) for a hydrogen-bonded trimer of water molecules. e-DFT-EE calculations are performed using three embedded subsystems, each corresponding to a different molecule in the trimer. In a first set of results, the symmetric dissociation curve for the trimer is calculated using no assumptions about the NAKP (solid); in a second set of results, the curve is calculated using assuming pairwise additivity of the NAKP (dot-dashed). The equilibrium geometry is provided in the supplemental information; other geometries along the dissociation curve were then obtained by uniformly stretching the oxygen-oxygen distances in the cluster, keeping all other internal coordinates unchanged.

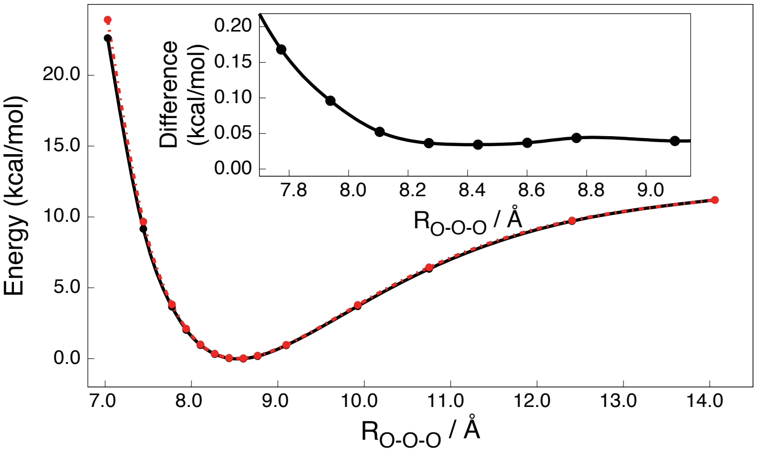

Figure 2.5: Symmetric dissociation curves for the water trimer, illustrating the pairwise additivity of the NAKP. Calculations are performed using the e-DFT-EE method, with no approximation to the NAKP (black, solid) and with the pairwise approximation to NAKP (red, dot-dashed). The curves are plotted as a function of the sum of the three O-O distances, with details of the molecular geometries provided in the text. Total energies plotted with respect to the minimum energy of -229.4403073 Hartree for the full NAKP treatment. Inset, the difference between the two curves is plotted.

The trimer calculations were performed using the modified aug-pc-2 basis set with the monomolecular basis set convention; all other calculation details are identical to those described previously for the modified aug-pc-2 calculations of the water dimer.

The agreement between the two curves in Fig. 2.5 indicates that Eqs. 2.17 and 2.18 are excellent approximations for the non-additive kinetic energy and NAKP, respectively. Throughout the entire attractive branch of the curve the total energies differ by less the 0.5 kcal/mol, and the largest deviations appear only in the strongly repulsive region at short distances. This good agreement is particularly notable, given that the cyclic trimer geometries might be expected to magnify possible non-additive contributions to the total energy; even better adherence of the NAKP to pairwise additivity is expected for linear geometries of the trimer. We have previously noted that higher-order corrections to Eqs. 2.17 and 2.18 are possible,[24] although the results in Fig. 2.5 suggest that the assumption of pairwise additivity will be adequate in many cases.

2.5.3 Parallel Scaling of e-DFT-EE

Primary bottlenecks in KS-DFT include calculation of the two-electron integrals and solution of the eigenvalue problem. In standard implementations, the two-electron integral calculations scales as M^4 and the eigenvalue calculation scales at best as M^2, where M is the total number of basis functions.[51,52] More efficient methods for computing the two-electron integrals include prescreening,[53] Ewald summations,[54] and the fast-multipole method;[55] however, solution of the eigenvalue problem remains a computational bottleneck in most KS-DFT implementations.[56]

As has been noted in previous work,[18] the monomolecular basis set convention leads to advantageous scaling properties for e-DFT. In this convention, the number of basis functions used to solve each KSCED, M_{sub}, is independent of system size. Consequently, the total cost of the eigenvalue problem scales linearly with the number of subsystems, N_{sub}, and it can be trivially parallelized to the subsystem level.

The cost of the two-electron integral calculation is also reduced in the monomolecular basis set convention. Terms arising from orbitals centered on molecules in more than two different subsystems are exactly zero, such that the total cost of this operation scales with $N_{\mathrm{sub}}^2 M_{\mathrm{sub}}^4$. Furthermore, in this convention, the density for each subsystem is spatially localized, such that short-ranged contributions to the KSCED effective potential, including exchange, correlation, short-ranged electrostatic contributions, and pairwise contributions to the NAKP, can be truncated at a cutoff distance. Long-ranged electrostatic contributions to the KSCED effective potential can be efficiently treated using Ewald summations or other standard methods.[54,55] Setting aside these long-ranged terms for the current demonstration, the use of distance-based cutoffs reduces the scaling of the total two-electron integral calculation to $N_{\mathrm{sub}} M_{\mathrm{sub}}^4$, which can be parallelized to yield constant wall-clock time scaling with increasing system size.

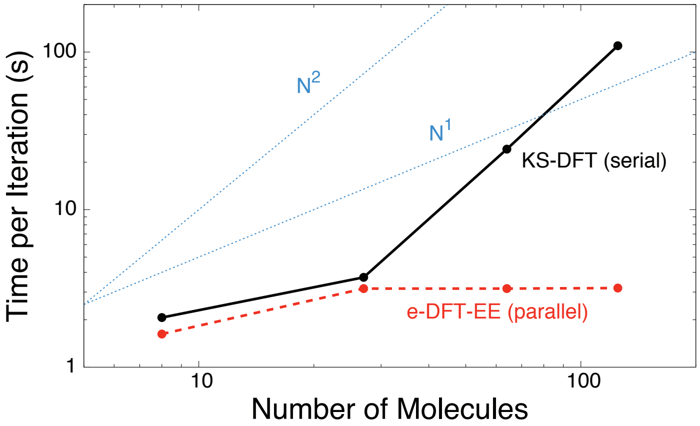

Figure 2.6: Wall-clock timings for lattices of hydrogen molecules, ranging in size from 8 to 125 H_2 molecules. The dotted blue lines indicate ideal quadratic and linear scaling, the solid, black curve corresponds to the serial implementation of integral-prescreened KS-DFT in Molpro, and the dashed, red curve corresponds to e-DFT-EE using a number of parallel processors equal to the number of molecules in the system.

To illustrate these scaling properties, Fig. 2.6 presents benchmark timings for simple tetragonal lattices of 8 to 125 H_2 molecules, using both e-DFT-EE and the KS-DFT implementation in Molpro. The H_2 molecules are oriented parallel to the z axis, with a bond length of 0.8 Å, and the centers-of-mass for the molecules are spaced by 3.0 Å along the x and y axes and by 3.8 Å along the z axis. All calculations employ the uncontracted STO-3G basis set,[57] Slater exchange[58] without electron correlation, and a grid density that ensures an integration error in the exchange energy of less than 10^{-6} Hartree. The e-DFT-EE calculations are performed with each molecule defined as a different subsystem, using the monomolecular basis set convention, and using one parallel processor per subsystem. Values for the parameters λ, ρ', κ, and the MO shift are the same as those used for the Li^+-Be system. The cutoff for the calculation of the electrostatics, exchange, and NAKP terms is set to 4.0 Å in these calculations, such that only nearest-neighbor molecules in the lattice contribute to these terms. All calculations are performed on a cluster of dual, quad-core 2.6 GHz Xeon Intel processors with Infiniband communication.

The timings in Fig. 2.6 indicate that the e-DFT-EE wall-clock time scales inde-

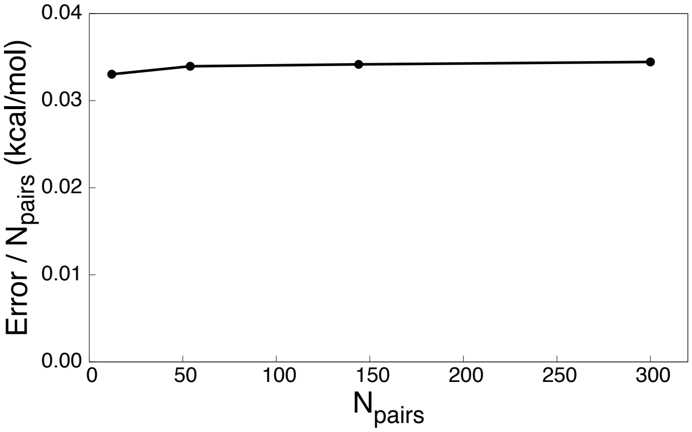

Figure 2.7: Error in the total energy of the e-DFT-EE calculation relative to KS-DFT for increasing system size, plotted with respect to the number of nearest-neighbor pairs.

pendently of the system size, with the deviations at small sizes due the boundaries of the finite crystal. As expected, the KS-DFT results in the serial Molpro implementation with integral prescreening scales quadratically with the increasing system size. In Fig. 2.7, relative energy of the e-DFT-EE and the KS-DFT calculations are plotted as a function of the number nearest-neighbor pairs in the lattice, $N_{\mathrm{pairs}} = 3(N_{\mathrm{sub}} - N_{\mathrm{sub}}^{2/3})$. The error is small and independent of system size. The integrated error in the density per molecule was found to behave similarly (not shown).

2.6 Conclusions

We introduce a general implementation of the EE method for calculating NAKP contributions in the e-DFT framework, and we present a range of molecular applications. The accuracy of e-DFT-EE is demonstrated for systems with covalently bonded and hydrogen-bonded subsystems. For the dissociation of the water dimer and the covalent bonds in Li^+-Be and $\mathrm{CH_3}$-$\mathrm{CF_3}$, e-DFT-EE preserves excellent agreement with reference KS-DFT calculations, whereas approximate treatments for the NAKP, including those based on the TF or LC94 kinetic energy functionals, lead to known failures.

Furthermore, pairwise approximation of the NAKP yields excellent accuracy for the hydrogen-bonded water trimer, and it enables ideal, constant system-size scaling in applications to molecular clusters with up to hundreds of atoms. These results establish e-DFT-EE as a promising methodology for performing accurate, first-principles molecular dynamics and for accurately embedding high-level wavefunction methods in complex systems.

Bibliography

[1] P. Cortona, Phys. Rev. B **44**, 8454 (1991).

[2] T. A. Wesolowski and A. Warshel, J. Phys. Chem. **97**, 8050 (1993).

[3] T. A. Wesolowski, in *Computational Chemistry: Reviews of Current Trends - Vol. 10*, pp. 1-82 (World Scientific, Singapore, 2006).

[4] N. Govind, Y. A. Wang, A. J. R. da Silva, and E. A. Carter, Chem. Phys. Lett. **295**, 129 (1998).

[5] H.-J. Werner, F. R. Manby, and P. J. Knowles, J. Chem. Phys. **118**, 8149 (2003).

[6] P. Elliott, K. Burke, M. H. Cohen, and A. Wasserman, Phys. Rev. A **82**, 024501 (2010).

[7] W. T. Yang, Phys. Rev. A **44**, 7823 (1991).

[8] W. Z. Liang, C. Saravanan, Y. H. Shao, R. Baer, A. T. Bell, and M. Head-Gordon, J. Chem. Phys. **119**, 4117 (2003).

[9] S. Li, J. Shen, W. Li, and Y. Jiang, J. Chem. Phys. **125**, 074109 (2006).

[10] W. Li, P. Piecuch, J. R. Gour, and S. Li, J. Chem. Phys. **131**, 114109 (2009).

[11] D. G. Fedorov and K. Kitaura, J. Chem. Phys. A **111**, 6904 (2007).

[12] M. A. Collins and V. A. Deev, J. Chem. Phys. **125**, 104104 (2006).

[13] C. R. Jacob, J. Neugebauer, and L. Visscher, J. Comput. Chem. **29**, 1011 (2008).

[14] J. Sauer, Chem. Rev. **89**, 199 (1989).

[15] G. Paccioni, P. S. Pagus, and F. Parmigiani, eds. *Cluster models for surface and bulk phenomena* , pp. 1-82 (NATO ASI Ser., New York, Plenum, 1992).

[16] K. Jug and T. Bredow, J. Comput. Chem. **25**, 1551 (2004).

[17] D. W. Zhang and J. Z. H. Zhang, J. Chem. Phys. **119**, 3599 (2003).

[18] M. Iannuzzi, B. Kirchner, and J. Hutter, Chem. Phys. Lett. **421**, 16 (2006).

[19] J. W. Kaminski, S. Gusarov, T. A. Wesolowski, and A. Kovalenko, J. Phys. Chem. A. **114**, 6082 (2010).

[20] A. S. P. Gomes, C. R. Jacob, and L. Visscher, Phys. Chem. Chem. Phys. **10**, 5353 (2008).

[21] A. W. Götz, S. M. Beyhan, and L. Visscher, J. Chem. Theory Comput. **5**, 3161 (2009).

[22] S. Fux, K. Kiewish, C. R. Jacob, J. Neugebauer, and M. Reiher, Chem. Phys. Lett. **461**, 353 (2008).

[23] S. Fux, C. R. Jacob, J. Neugebauer, L. Visscher, and M. Reiher, J. Chem. Phys. **132**, 164101 (2010).

[24] J. D. Goodpaster, N. Ananth, F. R. Manby, and T. F. Miller, III, J. Chem. Phys. **133**, 084103 (2010).

[25] C. R. Jacob and L. Visscher, J. Phys. Chem. **128**, 155102 (2008).

[26] S. M. Beyhan, A. W. Götz, C. R. Jacob, and L. Visscher, J. Chem. Phys. **132**, 044114 (2010).

[27] M. Levy, Proc. Natl. Acad. Sci. USA **76**, 6062 (1979).

[28] R. A. King and N. C. Handy, Phys. Chem. Chem. Phys. **2**, 5049 (2000).

[29] Q. S. Zhao and R. G. Parr, Phys. Rev. A **46**, 2337 (1992).

[30] Q. S. Zhao and R. G. Parr, J. Chem. Phys. **98**, 543 (1993).

[31] Q. S. Zhao, R. C. Morrison, and R. G. Parr, J. Chem. Phys. **50**, 2138 (1994).

[32] O. Roncero, M. P. de Lara-Castells, P. Villarreal, F. Flores, J. Ortega, M. Paniagua, and A. Aguado, J. Chem. Phys. **129**, 184104 (2008).

[33] O. Roncero, A. Zanchet, P. Villarreal, and A. Aguado, Chem. Phys. Lett. **131**, 234110 (2009).

[34] MOLPRO, version 2008.3, a package of ab initio programs, H.-J. Werner, P. J. Knowles, F. R. Manby, M. Schütz, and others, see www.molpro.net.

[35] T. A. Wesolowski, J. Chem. Phys. **106**, 8516 (1997).

[36] L. H. Thomas, Proc. Camb. Phil. Soc. **23**, 542 (1927).

[37] E. Fermi, Z. Phys. **48**, 73 (1928).

[38] A. Lembarki and H. Chermette, Phys. Rev. A **50**, 5328 (1994).

[39] J. P. Perdew, Phys. Rev. B **33**, 8822 (1986).

[40] A. D. Becke, Phys. Rev. A **38**, 3098 (1988).

[41] C. W. Murray, N. C. Handy, and G. J. Laming, Mol. Phys. **78**, 997 (1993).

[42] P. Pulay, Chem. Phys. Lett. **72**, 393 (1980).

[43] P. Pulay, J. Chem. Phys. **3**, 556 (1982).

[44] D. M. Shaw and A. St-Amant, J. Theor. Comput. Chem. **3**, 419 (2004).

[45] F. Jensen, J. Chem. Phys. **115**, 9113 (2001).

[46] D. E. Woon and T. H. Dunning, Jr., J. Chem. Phys. **103**, 4572 (1995).

[47] F. A. Hamprecht A. J. Cohen, D. J. Tozer, and N. C. Handy, J. Chem. Phys. **109**, 6264 (1998).

[48] A. D. Boese N. L. Doltsinis, N. C. Handy, and M. Sprik, J. Chem. Phys. **112**, 1670 (2000).

[49] P. J. Wilson T. J. Bradley, and D. J. Tozer, J. Chem. Phys. **115**, 9233 (2001).

[50] G. Menconi P. J. Wilson, and D. J. Tozer, J. Chem. Phys. **114**, 3958 (2001).

[51] S. Delvaux and M. Van Barel, J. Comput. Appl. Math. **213**, 268 (2008).

[52] M. Gu and S. C. Eisenstat, SIAM J. Matrix Anal. Appl. **16**, 172 (1995).

[53] M. Schutz, R. Lindh, and H.-J. Werner, Molecular Phys. **96**, 719 (1999).

[54] S. Hammes-Schiffer and H. C. Andersen, J. Chem. Phys. **101**, 375 (1994).

[55] G. Te Velde, F. M. Bickelhaupt, E. J. Baerends, C. Fonseca Guerra, S. J. A. Van Gisbergen, J. G. Snijders, and T. Ziegler, J. Comput. Chem. **22**, 931 (2001).

[56] Y. Saad, J. R. Chelikowsky, and S. M. Shontz, SIAM Review **52**, 3 (2010).

[57] W. J. Hehre, R. F. Stewart, and J. A. Pople, J. Chem. Phys **51**, 2657 (1969).

[58] J. C. Slater, Phys. Rev. **81**, 385-390 (1951).

[59] M. Dulak, J. W. Kamiński, and T. A. Wesolowski, J. Chem. Theory Comput. **3**, 735 (2007).

[60] C.-O. Almbladh and A. C. Pedroza, Phys. Rev. A **29**, 2322 (1984).

[61] C.-O. Almbladh and U. von Barth, Phys. Rev. B **31**, 3231 (1985).

[62] Ł. Rajchel, P. S. Żuchowski, M. M. Szczęśniak, and G. Chałasiński, Chem. Phys. Lett. **486**, 160 (2010).

[63] Ł. Rajchel, P. S. Żuchowski, M. M. Szczęśniak, and G. Chałasiński, Phys. Rev. Lett. **104**, 163001 (2010).

Chapter 3

Density functional theory embedding for correlated wavefunctions: Improved methods for open-shell systems and transition metal complexes

3.1 Introduction

The demand for accurate and efficient descriptions of complex molecular systems requires development of quantum embedding methods for electronic structure in which a small subsystem is treated with a high level of theory while the remainder of the system is treated at a more affordable level. Widely used examples of quantum embedding include QM/MM,[1–6] ONIOM,[7,8] and fragment molecular orbital (FMO) approaches,[9–11] which have led to significant advances in the simulation of condensed-phase and biomolecular systems. However, such methods generally rely on empirical models for the subsystem interactions, including link-atom approximations for embedding across covalent bonds[12–15] and point-charge electrostatic descriptions of the environment,[4,9] that are difficult to systematically improve and that can fail in practical applications.[3,6,16,17]

Density functional theory (DFT) offers an appealing framework for addressing this challenge.[18–42] DFT embedding provides a formulation of electronic structure theory in which subsystem interactions depend only on their electronic densities, including non-additive contributions due to the electrostatic, exchange-correlation (XC), and kinetic energy terms. In the WFT-in-DFT embedding approach, the DFT embedding potential is included as an external potential for WFT calculations, providing a WFT-level description for one (or more) subsystem while the remaining subsystems and their interactions are seamlessly treated at the DFT level of theory.

Several groups, including this one, have recently demonstrated that non-additive kinetic energy contributions to the embedding potential can be exactly computed[26–28,33,35] with the use of optimized effective potential (OEP) methods.[43–49] In this paper, we introduce a simple technique to improve the robustness of OEP calculations in systems that exhibit small HOMO-LUMO gaps, such as transition metal complexes. In addition, we derive spin-dependent embedding potentials to enable the accurate description of open-shell systems in the WFT-in-DFT embedding framework. Numerical applications to the van-der-Waals-bound ethylene-propylene dimer and to the hexaaquairon(II) transition-metal cation illustrate the applicability of these new techniques and demonstrate the accuracy of the WFT-in-DFT approach in systems for which conventional density functional theory methods exhibit substantial errors.

3.2 Theory

Like Kohn-Sham (KS)-DFT, DFT embedding provides a formally exact framework for the ground-state electronic structure problem. Here, we review DFT-in-DFT embedding and its basis for WFT-in-DFT calculations.

3.2.1 DFT-in-DFT Embedding

We begin by considering a closed-shell system in which the total electronic density ρ_{AB} consists of two subsystems, $\rho_{\mathrm{AB}} = \rho_{\mathrm{A}} + \rho_{\mathrm{B}}$. The corresponding one-electron orbitals for ρ_{A} and ρ_{B} obey the Kohn-Sham Equations with Constrained Electron

Density (KSCED),[22]

$$\left[-\frac{1}{2}\nabla^2 + v_{\text{eff}}[\rho_{\text{A}}, \rho_{\text{AB}}; \mathbf{r}]\right] \phi_i^{\text{A}}(\mathbf{r}) = \epsilon_i^{\text{A}} \phi_i^{\text{A}}(\mathbf{r}), \tag{3.1}$$

$$\left[-\frac{1}{2}\nabla^2 + v_{\text{eff}}[\rho_{\text{B}}, \rho_{\text{AB}}; \mathbf{r}]\right] \phi_j^{\text{B}}(\mathbf{r}) = \epsilon_j^{\text{B}} \phi_j^{\text{B}}(\mathbf{r}), \tag{3.2}$$

where $i = 1, \ldots, N^{\text{A}}$, $j = 1, \ldots, N^{\text{B}}$, and N^{A} and N^{B} are the number of electrons in the respective subsystems. v_{eff} is the effective potential for the coupled one-electron equations,

$$v_{\text{eff}}[\rho_{\text{A}}, \rho_{\text{AB}}; \mathbf{r}] \quad = \quad v_{\text{eff}}^{\text{KS}}[\rho_{\text{A}}; \mathbf{r}] + v_{\text{emb}}(\mathbf{r}), \tag{3.3}$$

where $v_{\text{eff}}^{\text{KS}}[\rho_{\text{A}}; \mathbf{r}]$ is the standard KS potential for subsystem A, and

$$\begin{aligned} v_{\text{emb}}(\mathbf{r}) \quad &= \quad v_{\text{ne}}^{\text{B}}(\mathbf{r}) + v_{\text{J}}[\rho_{\text{B}}; \mathbf{r}] + v_{\text{xc}}[\rho_{\text{AB}}; \mathbf{r}] - \\ &\qquad v_{\text{xc}}[\rho_{\text{A}}; \mathbf{r}] + v_{\text{nad}}[\rho_{\text{A}}, \rho_{\text{AB}}; \mathbf{r}]. \end{aligned} \tag{3.4}$$

Here, $v_{\text{ne}}^{\text{B}}(\mathbf{r})$ is the nuclear-electron Coulomb potential from the nuclei contained in subsystem B, v_{J} is the Hartree potential, and v_{xc} is the XC potential. In addition to these familiar terms from conventional KS-DFT calculations, DFT embedding introduces the non-additive kinetic potential (NAKP) which properly enforces Pauli exclusion between the subsystem densities. It is obtained from

$$v_{\text{nad}}[\rho_{\text{A}}, \rho_{\text{AB}}; \mathbf{r}] = \left[\frac{\delta T_{\text{s}}^{\text{nad}}[\rho_{\text{A}}, \rho_{\text{B}}]}{\delta \rho_{\text{A}}}\right](\mathbf{r}), \tag{3.5}$$

where $T_{\mathrm{s}}^{\mathrm{nad}}[\rho_{\mathrm{A}}, \rho_{\mathrm{B}}] \equiv T_{\mathrm{s}}[\rho_{\mathrm{AB}}] - T_{\mathrm{s}}[\rho_{\mathrm{A}}] - T_{\mathrm{s}}[\rho_{\mathrm{B}}]$, and $T_{\mathrm{s}}[\rho]$ is the non-interacting kinetic energy functional. The total energy functional for the full system is then

$$\begin{aligned} E[\rho_{\mathrm{AB}}] &= T_{\mathrm{s}}[\rho_{\mathrm{A}}] + T_{\mathrm{s}}[\rho_{\mathrm{B}}] + T_{\mathrm{s}}^{\mathrm{nad}}[\rho_{\mathrm{A}}, \rho_{\mathrm{B}}] + \\ &\quad V_{\mathrm{ne}}[\rho_{\mathrm{AB}}] + J[\rho_{\mathrm{AB}}] + E_{\mathrm{xc}}[\rho_{\mathrm{AB}}], \end{aligned} \tag{3.6}$$

where the last three terms on the right-hand side (RHS) are the nuclear-electron Coulomb energy, the Hartree energy, and the XC energy computed over the total density. Enforcing $v_{\mathrm{emb}}(\mathbf{r})$ to be identical for all subsystems (see Sec. III B) leads to a unique partitioning in the DFT embedding formulation, such that the specification of the nuclei and the integer number of electrons in subsystem A and B fully specify the density partitioning.[26,35] Eqs. 1-3.6 are easily generalized to the description of multiple embedded subsystems.

We have previously demonstrated that by using OEP methods to calculate the NAKP, DFT-in-DFT embedding can accurately describe both weakly and strongly interacting subsystems, including subsystems connected by covalent bonds;[27,28] and we have shown that this method is computationally feasible for large systems by way of localized approximations to the NAKP.[28] More recently, we have introduced a projection approach that completely avoids the NAKP calculation in exact DFT embedding,[29] which appears worthy of further investigation. The OEP-based approach employed here is appealing because it provides a local embedding potential that is a functional of only the subsystem electronic densities.

In practice, the KSCED equations (Eq. 3.1 and Eq. 3.2) are solved by simply modifying the core Hamiltonian in the self-consistent field (SCF) calculation to include the additional embedding terms. The embedding potential (Eq. 3.4) can be written in the atomic orbital (AO) basis as

$$\begin{aligned}\mathbf{v}_{\mathrm{emb}} &= \mathbf{v}_{\mathrm{ne}}^{\mathrm{B}} + \mathbf{J}[\gamma_{\mathrm{B}}] + \mathbf{v}_{\mathrm{xc}}[\gamma_{\mathrm{AB}}] - \\ &\quad \mathbf{v}_{\mathrm{xc}}[\gamma_{\mathrm{A}}] + \mathbf{v}_{\mathrm{nad}}[\gamma_{\mathrm{A}}, \gamma_{\mathrm{AB}}],\end{aligned} \tag{3.7}$$

where the various terms on the RHS of this expression correspond to those in Eq. 3.4. The subsystem and total AO density matrices in Eq. 3.7 satisfy $\gamma_{\mathrm{A}} + \gamma_{\mathrm{B}} = \gamma_{\mathrm{AB}}$. It follows that the Fock matrix for subsystem A can be expressed as

$$\mathbf{f}^{\mathrm{A\ in\ B}} = \mathbf{h}^{\mathrm{A\ in\ B}} + \mathbf{J}[\gamma_{\mathrm{A}}] + \mathbf{v}_{\mathrm{xc}}[\gamma_{\mathrm{A}}], \tag{3.8}$$

where

$$\mathbf{h}^{\mathrm{A\ in\ B}} = \mathbf{h}^{\mathrm{A}} + \mathbf{v}_{\mathrm{emb}}, \tag{3.9}$$

and $\mathbf{h}^{\mathrm{A}}$ is the core Hamiltonian for subsystem A (the kinetic energy plus external potential due to the nuclei in subsystem A). The Fock matrix for subsystem B, $\mathbf{f}^{\mathrm{B\ in\ A}}$, is analogously defined.

3.2.2 WFT-in-DFT Embedding

The embedding potential in Eq. 3.4 describes the subsystem interactions in terms of their corresponding electronic densities. However, the subsystem densities can be computed with any level of theory, thus allowing for the description of one subsystem at the (single- or multi-reference) WFT level, while the remaining environment is treated at the DFT level.[23,29,34,35,50–54] Closed-shell WFT-in-DFT embedding simply involves performing a WFT calculation on a given subsystem using the modified core Hamiltonian, $\mathbf{h}^{\mathrm{A\ in\ B}}$ in Eq. 3.9, that contains the embedding terms due to the environment of the other subsystem. The WFT-in-DFT energy is then obtained by modifying the DFT energy with respect to subsystem contributions at the WFT level,[35]

$$\begin{aligned} E_{\mathrm{tot}}\left[\rho_{\mathrm{A}}^{\mathrm{WFT}},\rho_{\mathrm{B}}^{\mathrm{DFT}}\right] &= E_{\mathrm{AB}}^{\mathrm{DFT}}[\rho_{\mathrm{AB}}^{\mathrm{DFT}}] \\ &\quad -\left(E_{\mathrm{A}}^{\mathrm{DFT}}[\rho_{\mathrm{A}}^{\mathrm{DFT}}]+\int v_{\mathrm{emb}}(\mathbf{r})\rho_{\mathrm{A}}^{\mathrm{DFT}}(\mathbf{r})d\mathbf{r}\right) \\ &\quad +\left(E_{\mathrm{A}}^{\mathrm{WFT}}[\rho_{\mathrm{A}}^{\mathrm{WFT}}]+\int v_{\mathrm{emb}}(\mathbf{r})\rho_{\mathrm{A}}^{\mathrm{WFT}}(\mathbf{r})d\mathbf{r}\right). \end{aligned} \tag{3.10}$$

This expression is easy to evaluate since the terms in the parentheses are just the DFT and WFT energies of subsystem A performed using the modified core Hamiltonian, $\mathbf{h}^{\mathrm{A\ in\ B}}$. Just as DFT-in-DFT embedding is an exact theory for the case of an exact DFT XC functional, WFT-in-DFT embedding is an exact theory for the case of an exact DFT XC functional and a full configuration interaction (FCI) WFT description.[52]

3.3 Methods of Implementation

Here, we describe techniques to improve the accuracy and convergence of both DFT-in-DFT and WFT-in-DFT calculations. First, a description of open-shell DFT embedding is developed to incorporate the effects of spin-dependence in the embedding potential. Then, implementation of the OEP calculation is discussed, and an orbital occupation constraint is introduced to enable robust DFT-in-DFT and WFT-in-DFT embedding calculations for systems with low-lying virtual orbitals, such as transition metal complexes.

3.3.1 Embedding for Open-Shell Systems

For an open-shell embedded subsystem, the α and β electrons generally experience different embedding potentials due to differing non-additive XC and NAKP contributions. Previous WFT-in-DFT implementations for open-shell systems have in practice neglected this difference, effectively assuming that the spin polarization is localized within the WFT subsystem.[34,53] In this study, we show that effects due to spin-dependent potentials are substantial and easily included via separate α and β embedding potentials. We develop approaches to utilize both restricted and unrestricted open-shell orbital formulations in WFT calculations.

3.3.1.1 Open-Shell DFT-in-DFT Embedding

We begin by considering an open-shell system for which the total electronic density is comprised of the α and β density of the two subsystems, $\rho_{\mathrm{AB}} = \rho_{\mathrm{A}}^{\alpha} + \rho_{\mathrm{A}}^{\beta} + \rho_{\mathrm{B}}^{\alpha} + \rho_{\mathrm{B}}^{\beta}$. The effective potential for the unrestricted spin orbitals[27] is

$$v_{\mathrm{eff}}^{\alpha}[\rho_{\mathrm{A}}^{\alpha}, \rho_{\mathrm{A}}^{\beta}, \rho_{\mathrm{B}}^{\alpha}, \rho_{\mathrm{B}}^{\beta}; \mathbf{r}] = v_{\mathrm{eff}}^{\mathrm{KS},\alpha}[\rho_{\mathrm{A}}^{\alpha}, \rho_{\mathrm{A}}^{\beta}; \mathbf{r}] + v_{\mathrm{emb}}^{\alpha}(\mathbf{r}), \tag{3.11}$$

where $v_{\mathrm{eff}}^{\mathrm{KS},\alpha}[\rho_{\mathrm{A}}^{\alpha}, \rho_{\mathrm{A}}^{\beta}; \mathbf{r}]$ is the standard KS effective potential for the unrestricted (U)KS orbitals, and $v_{\mathrm{emb}}^{\alpha}(\mathbf{r})$ is a spin-dependent embedding potential applied only to the α-spin electrons,

$$\begin{aligned} v_{\mathrm{emb}}^{\alpha}(\mathbf{r}) = {} & v_{\mathrm{ne}}^{\mathrm{B}}(\mathbf{r}) + v_{\mathrm{J}}[\rho_{\mathrm{B}}; \mathbf{r}] + v_{\mathrm{xc}}^{\alpha}[\rho_{\mathrm{AB}}^{\alpha}, \rho_{\mathrm{AB}}^{\beta}; \mathbf{r}] - \\ & v_{\mathrm{xc}}^{\alpha}[\rho_{\mathrm{A}}^{\alpha}, \rho_{\mathrm{A}}^{\beta}; \mathbf{r}] + v_{\mathrm{nad}}^{\alpha}[\rho_{\mathrm{A}}^{\alpha}, \rho_{\mathrm{AB}}^{\alpha}; \mathbf{r}]. \end{aligned} \tag{3.12}$$

The corresponding quantities for the β-spin electrons are analogously defined. The total energy functional for the full open-shell system is then

$$\begin{aligned} E[\rho_{\mathrm{AB}}] &= T_{\mathrm{s}}[\rho_{\mathrm{A}}^{\alpha}] + T_{\mathrm{s}}[\rho_{\mathrm{B}}^{\alpha}] + T_{\mathrm{s}}^{\mathrm{nad}}[\rho_{\mathrm{A}}^{\alpha}, \rho_{\mathrm{B}}^{\alpha}] + \\ &\quad T_{\mathrm{s}}[\rho_{\mathrm{A}}^{\beta}] + T_{\mathrm{s}}[\rho_{\mathrm{B}}^{\beta}] + T_{\mathrm{s}}^{\mathrm{nad}}[\rho_{\mathrm{A}}^{\beta}, \rho_{\mathrm{B}}^{\beta}] + \\ &\quad V_{\mathrm{ne}}[\rho_{\mathrm{AB}}] + J[\rho_{\mathrm{AB}}] + E_{\mathrm{xc}}[\rho_{\mathrm{AB}}^{\alpha}, \rho_{\mathrm{AB}}^{\beta}]. \end{aligned} \tag{3.13}$$

Separate OEP calculations are performed over the α and β spin-densities for the exact calculation of the NAKP, which allows for numerically exact unrestricted open-shell DFT embedding (U-DFT-in-DFT).[27]

In practice, we solve for the unrestricted spin orbitals by adding the spin-dependent embedding potentials to the α and β Fock matrices. The α and β embedding potential can be written in the AO basis as

$$\begin{aligned} \mathbf{v}_{\mathrm{emb}}^{\xi} &= \mathbf{v}_{\mathrm{ne}}^{\mathrm{B}} + \mathbf{J}[\gamma_{\mathrm{B}}] + \mathbf{v}_{\mathrm{xc}}^{\xi}[\gamma_{\mathrm{AB}}^{\alpha}, \gamma_{\mathrm{AB}}^{\beta}] - \\ &\quad \mathbf{v}_{\mathrm{xc}}^{\xi}[\gamma_{\mathrm{A}}^{\alpha}, \gamma_{\mathrm{A}}^{\beta}] + \mathbf{v}_{\mathrm{nad}}^{\xi}[\gamma_{\mathrm{A}}^{\xi}, \gamma_{\mathrm{AB}}^{\xi}], \end{aligned} \tag{3.14}$$

where $\xi \in \{\alpha, \beta\}$, and the corresponding Fock matrices are

$$\mathbf{f}^{\xi,\mathrm{A\ in\ B}} = \mathbf{h}^{\mathrm{A}} + \mathbf{J}[\gamma_{\mathrm{A}}] + \mathbf{v}_{\mathrm{xc}}^{\xi}[\gamma_{\mathrm{A}}^{\alpha}, \gamma_{\mathrm{A}}^{\beta}] + \mathbf{v}_{\mathrm{emb}}^{\xi}. \tag{3.15}$$

The unrestricted spin orbitals for subsystem A are then obtained by separately diagonalizing $\mathbf{f}^{\alpha,\mathrm{A\ in\ B}}$ and $\mathbf{f}^{\beta,\mathrm{A\ in\ B}}$ in the usual way.

Practical implementations for performing OEP calculations using restricted open-shell orbitals have yet to be developed. We thus introduce a simple, approximate scheme for restricted open-shell DFT embedding (RO-DFT-in-DFT). In this approach, a U-DFT-in-DFT calculation is first performed, and the embedding potentials

$\mathbf{v}^{\alpha}_{\mathrm{emb}}$ and $\mathbf{v}^{\beta}_{\mathrm{emb}}$ are constructed using Eq. 3.14. Then, $\mathbf{f}^{\alpha,\mathrm{A\ in\ B}}$ and $\mathbf{f}^{\beta,\mathrm{A\ in\ B}}$ are constructed using Eq. 3.15, and the usual RO approach is employed to obtain subsystem orbitals that are spatially identical for the α and β electrons. Specifically, $\mathbf{f}^{\alpha,\mathrm{A\ in\ B}}$ is diagonalized to obtain a set of occupied α spin orbitals, $\{\phi^{\alpha,\mathrm{A}}_{\mathrm{occ}}\}$, and $\mathbf{f}^{\beta,\mathrm{A\ in\ B}}$ is then projected into the space of the occupied α spin orbitals using

$$\tilde{\mathbf{f}}^{\beta,\mathrm{A\ in\ B}} = \mathbf{c}^{\mathrm{T}}\mathbf{f}^{\beta,\mathrm{A\ in\ B}}\mathbf{c}, \tag{3.16}$$

where $\mathbf{c}$ is the matrix with columns comprised of the AO coefficients for $\{\phi^{\alpha,\mathrm{A}}_{\mathrm{occ}}\}$. Finally, the projected Fock matrix, $\tilde{\mathbf{f}}^{\beta,\mathrm{A\ in\ B}}$, is diagonalized to obtain the set of RO orbitals, $\{\phi^{\mathrm{A}}_{\mathrm{occ}}\}$, with the first $N^{\beta,\mathrm{A}}$ orbitals doubly occupied and with orbitals $N^{\beta,\mathrm{A}}+1,\ldots,N^{\alpha,\mathrm{A}}$ singly occupied, where $N^{\alpha,\mathrm{A}}$ and $N^{\beta,\mathrm{A}}$ indicate the number of α and β electrons in subsystem A. Although the second and third terms on the RHS of Eq. 3.15 are updated at each iteration of the RO-DFT-in-DFT calculation, we leave the embedding potentials unchanged to avoid performing OEP calculations using restricted open-shell orbitals. The RO-DFT-in-DFT energy for the total density is calculated using Eq. 3.13.

Several different schemes have been proposed to calculate the embedding potential for open-shell subsystems while neglecting its spin-dependence.[34,35,53] These approaches generally assume that interactions between the subsystems can be described by a single embedding potential. For example, in systems with an even number of electrons, the embedding potential, $\mathbf{v}_{\mathrm{emb}}$ in Eq. 3.7, can be obtained assuming that each embedded subsystem is closed-shell, and then the open-shell subsystem is calculated using $\mathbf{v}^{\alpha}_{\mathrm{emb}} = \mathbf{v}^{\beta}_{\mathrm{emb}} = \mathbf{v}_{\mathrm{emb}}$. In this approach, Eq. 3.15 is solved self-consistently while $\mathbf{v}^{\alpha}_{\mathrm{emb}}$ and $\mathbf{v}^{\beta}_{\mathrm{emb}}$ are held fixed, and the final DFT-in-DFT energy is calculated using Eq. 3.13. This spin-independent description of the embedding potential can be used with either an unrestricted treatment of the open-shell subsystem (U-DFT-in-DFT-

CS) or a restricted treatment of the open-shell subsystem (RO-DFT-in-DFT-CS); we later employ the approach to compare with the previously described methods (U-DFT-in-DFT and RO-DFT-in-DFT) that include spin-dependence in the embedding potential.

3.3.1.2 Open-Shell WFT-in-DFT Embedding

Unrestricted open-shell WFT-in-DFT (U-WFT-in-DFT) calculations are performed by first computing unrestricted Hartree-Fock (UHF) orbitals in the spin-dependent embedding potential, and then using these orbitals for a post-HF WFT calculation. The α and β Fock matrices for the calculation of the UHF orbitals are

$$\mathbf{f}^{\xi,\mathrm{A\ in\ B}} = \mathbf{h}^{\mathrm{A}} + \mathbf{J}[\gamma_{\mathrm{A}}] + \mathbf{K}^{\xi}[\gamma_{\mathrm{A}}^{\xi}] + \mathbf{v}_{\mathrm{emb}}^{\xi}, \tag{3.17}$$

where $\xi \in \{\alpha, \beta\}$, $\mathbf{K}$ is the HF exchange matrix, and the embedding potentials (Eq. 3.14) are obtained from a U-DFT-in-DFT embedding calculation. The total energy is evaluated using

$$\begin{aligned} E_{\mathrm{tot}}\left[\rho_{\mathrm{A}}^{\mathrm{WFT}}, \rho_{\mathrm{B}}^{\mathrm{DFT}}\right] &= E_{\mathrm{AB}}^{\mathrm{DFT}}[\rho_{\mathrm{AB}}^{\mathrm{DFT}}] \\ &- \left(E_{\mathrm{A}}^{\mathrm{DFT}}[\rho_{\mathrm{A}}^{\mathrm{DFT}}] + \sum_{\xi\in\{\alpha,\beta\}} \int v_{\mathrm{emb}}^{\xi}(\mathbf{r})\rho_{\mathrm{A}}^{\xi,\mathrm{DFT}}(\mathbf{r})d\mathbf{r}\right) \\ &+ \left(E_{\mathrm{A}}^{\mathrm{WFT}}[\rho_{\mathrm{A}}^{\mathrm{WFT}}] + \sum_{\xi\in\{\alpha,\beta\}} \int v_{\mathrm{emb}}^{\xi}(\mathbf{r})\rho_{\mathrm{A}}^{\xi,\mathrm{WFT}}(\mathbf{r})d\mathbf{r}\right). \end{aligned} \tag{3.18}$$

Restricted open-shell WFT-in-DFT (RO-WFT-in-DFT) calculations are performed by solving for restricted open-shell HF (ROHF) orbitals in the spin-dependent embedding potential. Just as in RO-DFT-in-DFT embedding, a U-DFT-in-DFT calculation is first performed, and the embedding potentials $\mathbf{v}_{\mathrm{emb}}^{\alpha}$ and $\mathbf{v}_{\mathrm{emb}}^{\beta}$ are constructed using Eq. 3.14. Then, the Fock matrices in Eq. 3.17 are constructed and the usual approach is employed to obtain RO orbitals; the second and third terms on the RHS of Eq. 3.17 are updated at each iteration while the embedding potential is left unchanged. The ROHF orbitals are used in the post-HF WFT calculation, and the total energy is then evaluated using Eq. 3.18. We note that for the RO-WFT-in-DFT energy calculation, the term $E_{\mathrm{A}}^{\mathrm{DFT}}[\rho_{\mathrm{A}}^{\mathrm{DFT}}]$, is evaluated using the ROKS-DFT energy.

3.3.2 Optimized Effective Potential

As seen in Eqs. 3.5 and 3.6, DFT embedding requires computation of both the kinetic energy, $T_{\mathrm{s}}[\rho_{\mathrm{AB}}]$, and its functional derivative. However, since the explicit functional form for the kinetic energy is unknown, OEP methods are needed to obtain these terms exactly.

The OEP is the local potential for which solution of the one-electron equations

$$\left[-\frac{1}{2}\nabla^2 + v_{\mathrm{OEP}}(\mathbf{r})\right]\phi_i \quad = \quad \epsilon_i\phi_i \tag{3.19}$$

yields orbitals that correspond to a given target density while minimizing the non-interacting kinetic energy. A variety of methods for determining such potentials from an input target density have been developed.[43–49] Calculations reported here employ the direct optimization procedure developed by Wu and Yang,[43,44] in which the kinetic energy is obtained via the unconstrained maximization

$$T_{\mathrm{s}}[\rho_{\mathrm{in}}] = \max_{v_{\mathrm{OEP}}(\mathbf{r})} \left\{W_{\mathrm{s}}\left[\Psi_{\mathrm{det}}, v_{\mathrm{OEP}}(\mathbf{r})\right]\right\}, \tag{3.20}$$

where

$$\begin{aligned} W_{\mathrm{s}}\left[\Psi_{\mathrm{det}}, v_{\mathrm{OEP}}(\mathbf{r})\right] &= 2\sum_{i}^{\frac{N}{2}}\langle\phi_i| -\frac{1}{2}\nabla^2|\phi_i\rangle \\ &+ \int\left(\rho_{\mathrm{OEP}}(\mathbf{r}) - \rho_{\mathrm{in}}(\mathbf{r})\right) v_{\mathrm{OEP}}(\mathbf{r}) d\mathbf{r} \\ &- \zeta||\nabla v_\lambda(\mathbf{r})||^2, \end{aligned} \tag{3.21}$$

and

$$v_{\mathrm{OEP}}(\mathbf{r}) = v_{\mathrm{eff}}^{\mathrm{KS}}[\rho_{\mathrm{in}};\mathbf{r}] + v_\lambda(\mathbf{r}). \tag{3.22}$$

In these equations, $v_\lambda(\mathbf{r}) = \sum_t b_t g_t(\mathbf{r})$, $\{g_t(\mathbf{r})\}$ comprise an auxiliary basis set for the potential, b_t are the corresponding expansion coefficients, and ζ is a regularization parameter.[44] Maximization of W_{s} utilizes the Newton method for optimization with a back-tracking line search in the expansion coefficients,[55]

$$\mathbf{b}^{(i+1)} = \mathbf{b}^{(i)} + \tau\mathbf{H}^{-1}\mathbf{g}, \tag{3.23}$$

where i is the iteration number, $\mathbf{H}$ and $\mathbf{g}$ are the Hessian and gradient of W_s, respectively, and $\tau \in$ [0,1] is the step-size in the line search.

In practice, to obtain the embedding potential, we do not explicitly calculate the NAKP for each subsystem. Instead, for closed shell subsystems, we directly update the embedding potential (Eq. 3.4) at each iteration of the KSCED equations using[26]

$$v_{\mathrm{emb}}^{(i+1)}(\mathbf{r}) = v_{\mathrm{emb}}^{(i)}(\mathbf{r}) - \theta v_\lambda(\mathbf{r}), \tag{3.24}$$

where $\theta \in$ [0,1] is a damping coefficient. By construction, the embedding potential for each subsystem is identical at every iteration. The KSCED equations are initialized using $v_{\mathrm{emb}}^{(0)}(\mathbf{r}) = 0$, such that the initial guess for the NAKP for subsystem A exactly cancels the remaining terms in Eq. 3.4 (and the initial guess for the NAKP for subsystem B likewise cancels the corresponding terms). Upon convergence of the KSCED equations, $v_\lambda(\mathbf{r}) = 0$, $v_{\mathrm{eff}}^{\mathrm{KS}}[\rho_{\mathrm{AB}}; \mathbf{r}] = v_{\mathrm{eff}}^{\mathrm{KS}}[\rho_{\mathrm{KS}}; \mathbf{r}]$, and $v_{\mathrm{emb}}(\mathbf{r}) = v_{\mathrm{emb}}^{(i)}(\mathbf{r})$. Enforcing the embedding potential to be identical for all subsystems leads to a unique partitioning of the subsystem densities.[26,35]

For open-shell calculations, we similarly update the spin-dependent embedding potential (Eq. 3.12); the OEP obtained for a given spin density is

$$v_{\mathrm{OEP}}^{\xi}(\mathbf{r}) = v_{\mathrm{eff}}^{\mathrm{KS},\xi}[(\rho_{\mathrm{A}}^{\alpha} + \rho_{\mathrm{B}}^{\alpha}), (\rho_{\mathrm{A}}^{\beta} + \rho_{\mathrm{B}}^{\beta}); \mathbf{r}] + v_{\lambda}^{\xi}(\mathbf{r}), \tag{3.25}$$

and as in Eq. 3.24, $v_\lambda^\xi(\mathbf{r})$ is used to update $v_{\mathrm{emb}}^{\xi}(\mathbf{r})$ at each iteration.

Finally, we note that XC functionals that include a fraction of the exact exchange can be employed in DFT embedding via the OEP calculation. The HF exchange matrix, $\mathbf{K}$, is evaluated using γ_{OEP}, the OEP density matrix in the AO basis. For DFT-in-DFT embedding, the exchange energy is calculated using

$$\begin{aligned} E_{\mathrm{X}}[\gamma_{\mathrm{OEP}}, \gamma_{\mathrm{in}}] &= -\mathrm{tr}\left(\gamma_{\mathrm{OEP}}\mathbf{K}[\gamma_{\mathrm{OEP}}]\right) \\ &\quad +\mathrm{tr}\left((\gamma_{\mathrm{OEP}} - \gamma_{\mathrm{in}})\mathbf{K}[\gamma_{\mathrm{OEP}}]\right), \end{aligned} \tag{3.26}$$

where the second term on the RHS corrects the exchange energy for small numerical differences between γ_{OEP} and γ_{in}. For calculations on the low-spin state of the hexaaquairon(II) cation, this correction is found to be as large as 20 kcal/mol; however, the correction is not required for the evaluation of the WFT-in-DFT energy (Eq. 3.10), since $E_{\mathrm{AB}}^{\mathrm{DFT}}[\rho_{\mathrm{AB}}^{\mathrm{DFT}}]$ is obtained directly from a KS-DFT calculation on the full system.

3.3.3 Orbital-Occupation Freezing

For W_{s} to be a concave function of $v^{\mathrm{OEP}}(\mathbf{r})$, it is necessary[43] that the orbitals used to construct ρ_{OEP} in Eq. 3.21 correspond to the lowest eigenvalues of Eq. 3.19. However, this can be problematic for systems with small energy differences between the occupied and virtual orbitals, where small changes in $v_{\mathrm{OEP}}(\mathbf{r})$ can alter the relative ordering of the orbitals.

To illustrate this issue, Fig. 3.1 shows the line search for an illustrative Newton step in an OEP calculation for the low-spin hexaaquairon(II) cation. W_{s} is plotted as a function of τ, where τ is the step-size in Eq. 3.23. For any step-size larger than $\tau = 0.38$ in this case, the orbital occupancy changes from one in which only $\mathrm{t}_{2\mathrm{g}}$-like d orbitals are occupied to one in which e_{g}-like d orbitals are occupied. In traditional back-tracking line searches, any step which increases W_{s} would be accepted, including the $\tau = 0.5$ step indicated with the red arrow. However, this step is problematic since the Hessian and gradient of W_{s} for the next Newton step would be evaluated using a density that corresponds to the wrong orbitals. The net results are poor convergence and incorrect solutions for the OEP.

We introduce a simple method to alleviate this problem by modifying the back-tracking line search. Reference (τ=0) orbitals are computed from Eq. 3.19 using $v_{\mathrm{OEP}}(\mathbf{r}) = v_{\mathrm{eff}}^{\mathrm{KS}}[\rho_{\mathrm{AB}}; \mathbf{r}]$, and for any proposed step-size τ, the corresponding orbitals are computed using $v_{\mathrm{OEP}}(\mathbf{r}) = v_{\mathrm{eff}}^{\mathrm{KS}}[\rho_{\mathrm{AB}}; \mathbf{r}] + v_{\lambda}(\mathbf{r})$. The proposed step is rejected if the overlap between these two sets of orbitals is less than 0.5, regardless of the change in W_{s}; otherwise, it is subjected to the usual criteria of the back-tracking line search algorithm. Upon rejection, the step-size τ is reduced by a factor of 2. This technique ensures that the correct orbitals remain occupied throughout the maximization of W_{s}. In Fig. 3.1, the proposed step indicated by the red arrow is rejected, whereas the proposed shorter step indicated by the black arrow is accepted; not only is the value

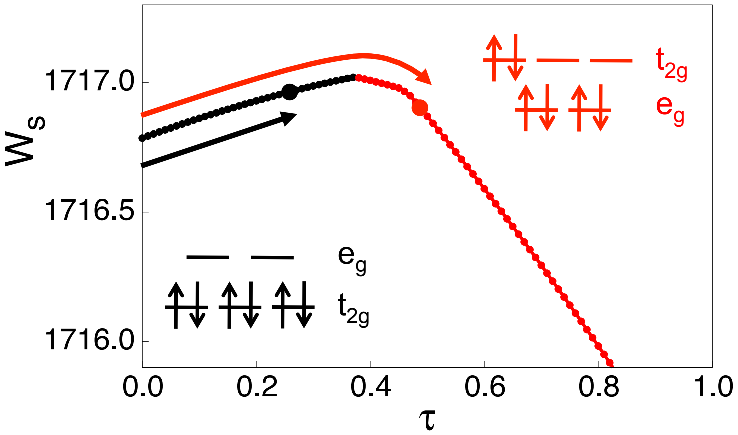

Figure 3.1: An illustrative Newton step in the OEP calculation for the low-spin hexaaquairon(II) cation, performed with (black) and without (red) the orbital-occupation-freezing technique. The technique ensures that correct orbitals remain occupied throughout the maximization of $W_{\rm s}$. See text for details.

of $W_{\rm s}$ increased, but the correct orbitals remain occupied. By utilizing this technique, we found that the maximization of $W_{\rm s}$ typically requires less than 20 Newton steps for the low spin state of the hexaaquairon(II) cation, whereas the optimization failed to converge without the use of orbital-occupation freezing.

3.3.4 Computational Details

The DFT embedding methods employed here are all implemented in the development version of the Molpro software package.[56] All calculations employ the supermolecular basis set convention, in which the molecular orbitals for each subsystem are described in the AO basis for the full system.[57] Calculations on the ethylene-propylene dimer use the aug-cc-pVTZ orbital basis set for the carbon atoms and the aug-cc-pVDZ orbital basis set for the hydrogen atoms. Calculations on the hexaaquairon(II) cation use the aug-cc-pVTZ orbital basis set for the iron atom and the aug-cc-pVDZ orbital basis set for the hydrogen and oxygen atoms. For the auxiliary basis set used in the OEP calculations, we employ atom-centered Gaussian basis functions ($g_t(\mathbf{r}) = N_t e^{-\lambda_t \mathbf{r}^2}$, where N_t is the normalization constant) for which the coefficient λ_t assumes values of 2^n, where $n = n_{\min}, n_{\min} + 2, \ldots, n_{\max} - 2, n_{\max}$. Calculations on the ethylene-propylene dimer employ the basis set for which the s-type functions for the carbon and hydrogen atoms span $\{n_{\min}, n_{\max}\}$ = {-4, 4}, and the p-type functions for the carbon and hydrogen atoms span {-2, 2}. Calculations for the hexaaquairon(II) cation employ the basis set for which the s-type functions for the iron atom span {-4, 6}, the p-type functions for the iron atom span {-4, 6}, the d-type functions for the iron atom span {-2, 2}, the s-type functions for the oxygen atoms span {-4, 6}, the p-type functions for the oxygen atoms span {-2, 4}, the s-type functions for the hydrogen atoms span {-4, 4}, and the p-type functions for the hydrogen atoms span {-2, 2}. For all systems, the finite auxiliary basis set for the OEP calculations was confirmed to introduce a difference of less than 1 kcal/mol between the total energy computed using KS-DFT and either closed-shell or unrestricted open-shell DFT-in-DFT embedding. The regularization parameter used in the OEP calculations is set to $\zeta = 10^{-3}$; smaller values were tested on the ethylene-propylene dimer and the hexaaquairon(II) cation and were found to have only a small ($\mathcal{O}(\mu\text{Hartree})$) effect on the total DFT-in-DFT energy.

The KSCED equations are initialized with subsystem densities comprised of the superposition of HF atomic densities and with $v_{\text{emb}}(\mathbf{r}) = 0$; different initial guesses for the embedding potential were tested on the hexaaquairon(II) cation and were found to yield similar final embedding potentials with only small ($\mathcal{O}(10\ \mu\text{Hartree})$) changes in the total DFT-in-DFT energy.

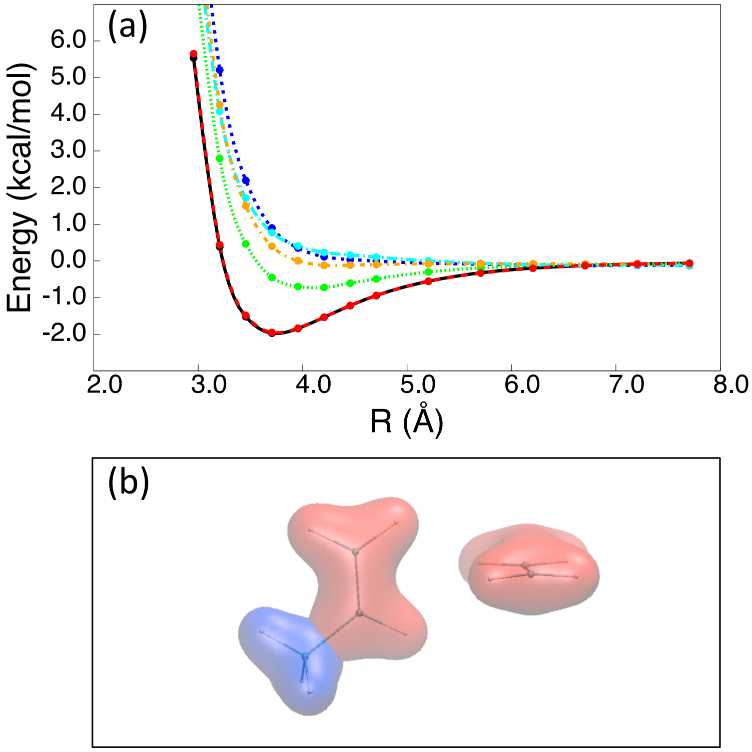

Figure 3.2: WFT-in-DFT embedding for the ethylene-propylene dimer. (a) The ethylene-propylene dissociation curve, obtained using CCSD(T)-in-B3LYP (red) and KS-DFT with PBE (green), B3LYP (orange), B-LYP (blue) and B88-P86 (cyan) for the XC functional. Also included are the reference CCSD(T) results (black), which are graphically indistinguishable from the CCSD(T)-in-B3LYP results. The curves are vertically shifted to align at infinite separation. (b) Isosurface plots indicate the subsystem partitioning for the ethene-propene dimer calculations. The red isosurface indicates the density of the 32 electrons associated with the C_2H_4-C_2H_3- moiety, and the blue isosurface indicates the density of the 8 electrons associated with the -CH_3 moiety. The isosurface plot corresponds to an electronic density of 0.05 a.u.

3.4 Results

3.4.1 The Ethylene-Propylene Dimer: WFT-in-DFT Embedding

The ethylene-propylene dimer is a prototypical system for which quantum embedding methods, such as QM/MM or ONIOM, may be employed. It exhibits a weak $\pi - \pi$ interaction that is difficult to address with conventional KS-DFT methods, while also exhibiting a spectator -CH_3 moiety that contributes little to the interaction energy while substantially increasing the cost of the high-level calculation. However, unlike the QM/MM treatment of subsystems, the interactions between the $\pi - \pi$ system and the -CH_3 moiety can be treated seamlessly using WFT-in-DFT embedding, as is now demonstrated.

Fig. 3.2(a) presents the ethylene-propylene dimer dissociation curve plotted as a function of the distance between the ethylene and propylene π bonds, with the equilibrium dimer geometry obtained via minimization at the MP2 level of theory. Other geometries along the curve are obtained by displacing the two molecules along the vector formed between the midpoints of the two C=C bonds, while fixing all other internal coordinates. The relative energies are plotted by aligning each curve at infinite separation. The full CCSD(T) calculation (black) shows a binding energy of 2.0 kcal/mol. KS-DFT calculations using the PBE[58,59] (green), B3LYP[60] (orange), B-LYP[61,62] (blue) and B88-P86[61,63] (cyan) XC functionals illustrate the difficulty in describing dispersion interactions using KS-DFT. The PBE functional underestimates the binding energy by 1.3 kcal/mol, while the rest of the XC functionals fail to capture any of the attractive interactions.

Finally, the red curve in Fig. 3.2(a) presents the results of WFT-in-DFT embedding, using a subsystem partitioning in which the 32 electrons associated with the π

system (C_2H_4-C_2H_3-, red in Fig. 3.2(b)) are treated at the WFT level of theory and the remaining 8 electrons in the -CH_3 moiety are treated at the DFT level of theory. We employ CCSD(T) for the WFT and the B3LYP XC functional for the DFT (i.e., CCSD(T)-in-B3LYP). Fig. 3.2(a) shows excellent agreement between the CCSD(T) (black) and CCSD(T)-in-B3LYP (red) calculations; these curves, which are graphically indistinguishable, differ by less than 0.10 kcal/mol through the entire range of distances. We have confirmed that this level of accuracy is maintained with different XC functionals used for the DFT; specifically, CCSD(T)-in-(B-LYP) energies differ from the CCSD(T) results by less than 0.20 kcal/mol throughout the entire curve. These results illustrate that WFT-in-DFT embedding can be used to systematically improve DFT results and to avoid embedding errors while partitioning across covalent bonds.

3.4.2 The Hexaaquairon(II) Cation

We now present DFT-in-DFT and WFT-in-DFT calculations for the high-spin $[{}^5\mathrm{T}_{2g} : (\mathrm{t}_{2g})^4(\mathrm{e}_g)^2]$ and low-spin $[{}^1\mathrm{A}_{1g} : (\mathrm{t}_{2g})^6(\mathrm{e}_g)^0]$ states of the hexaaquairon(II) cation, a system that presents challenges due to the presence of low-lying unoccupied orbitals, the important role of unpaired electrons, and the relatively large number of electrons (84 e^-) in the full system. First, we test the accuracy of DFT-in-DFT embedding for the various treatments of the open-shell embedding potential described earlier. We then employ WFT-in-DFT calculations to investigate the low-spin/high-spin energy splitting and the ligation energy for this transition metal complex.

3.4.2.1 DFT-in-DFT Embedding

Fig. 3.3(a) presents the potential energy curve for the simultaneous dissociation of all six H_2O ligands of the hexaaquairon(II) cation, plotted as a function of the average iron-oxygen distance. The equilibrium geometries for the low-spin $[{}^1\mathrm{A}_{1g} : (\mathrm{t}_{2g})^6(\mathrm{e}_g)^0]$

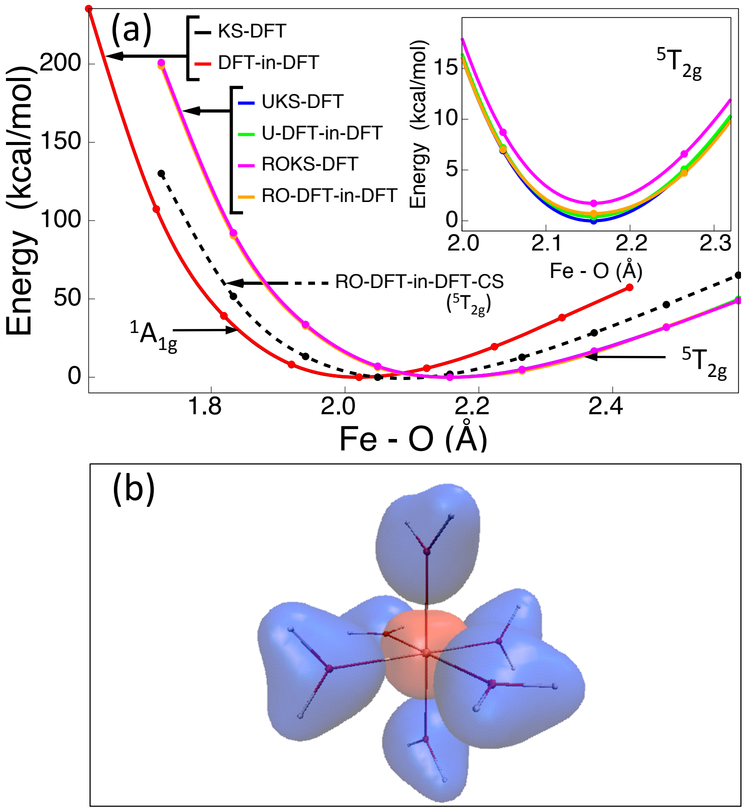

Figure 3.3: DFT-in-DFT embedding for the hexaaquairon(II) cation. (a) The potential energy curve for the simultaneous dissociation of the six H_2O ligands. All curves in the main panel are vertically shifted to share a common minimum energy; they are not horizontally shifted. The dissociation curves for the low-spin ($^1A_{1g}$) state obtained using KS-DFT (black) and DFT-in-DFT (red) are graphically indistinguishable. The dissociation curves or the high-spin ($^5T_{2g}$) state obtained using UKS-DFT (blue), U-DFT-in-DFT (green), ROKS-DFT (magenta), and RO-DFT-in-DFT (orange) are likewise graphically indistinguishable. The inset shows these four high-spin potential energy curves, with each curve vertically shifted only by the UKS-DFT minimum energy of -1721.693423 Hartree. The dashed black dissociation curve in the main panel is obtained using the RO-DFT-in-DFT-CS method, which neglects spin-dependence in the embedding potential. (b) Isosurface plots indicate the subsystem partitioning for the hexaaquairon(II) cation. The red isosurface indicates the density of the 24 electrons associated with the Fe atom, and the blue isosurface indicates the density of the 60 electrons associated with the six H_2O ligands. The isosurface plot corresponds to an electronic density of 0.05 a.u.

and high-spin [$^5T_{2g} : (t_{2g})^4(e_g)^2$] states are obtained using KS-DFT energy minimization with the B3LYP XC functional; all other geometries are obtained by uniformly stretching the iron-oxygen distances in the complex, keeping all other internal coordinates unchanged. All KS-DFT and DFT-in-DFT embedding results reported in this section are obtained using the B3LYP XC functional. The curves in the main panel of Fig. 3.3(a) are vertically shifted to share a common minimum value; they are not horizontally shifted. The high-spin state is lower in energy and exhibits a longer average iron-oxygen distance than the low-spin state.

We perform DFT-in-DFT embedding using a subsystem partitioning in which the 24 electrons associated with the iron center comprise one subsystem (red in Fig. 3.3(b)) and the remaining 60 electrons associated with the six water ligands comprise a second subsystem (blue in Fig. 3.3(b)). For the low-spin state, Fig. 3.3(a) demonstrates good numerical agreement between DFT-in-DFT (red) and KS-DFT (black); the relative energies differ by less than 0.6 kcal/mol throughout the range of reported internuclear distances.

For the high-spin state of the hexaaquairon(II) cation, Fig. 3.3(a) shows that the UKS-DFT and ROKS-DFT methods are in good agreement with each other, as well as with the corresponding U-DFT-in-DFT and RO-DFT-in-DFT embedding approaches described in Sec. III A 1. The U-DFT-in-DFT calculation accurately reproduces the relative energies obtained from UKS-DFT to within 0.4 kcal/mol throughout the attractive branch of the curve and to within 0.8 kcal/mol at shorter distances. The RO-DFT-in-DFT calculation reproduces the relative energy obtained from ROKS-DFT to within 1.0 kcal/mol throughout the attractive branch of the curve and to within 2.2 kcal/mol at shorter distances.

The inset of Fig. 3.3(a) shows the various potential energy curves computed for the high-spin state of the hexaaquairon(II) cation, with each curve vertically shifted by only the UKS-DFT minimum energy. This inset demonstrates relatively small differences in the total energies computed with the various embedding and open-shell treatments.

Finally, the dashed black curve in Fig. 3.3(a) demonstrates the importance of including spin-dependence in the embedding potential. This curve corresponds to the RO-DFT-in-DFT-CS treatment of the high-spin state of the hexaaquairon(II) cation described in Sec. III A 1. It exhibits large relative errors (over 70 kcal/mol) compared to the other treatments of the high-spin state of the hexaaquairon(II) cation, as well as qualitatively incorrectly shortening of the equilibrium internuclear distance. Although this approximation is expected to be more reliable for systems in which the spin-density is strongly localized with a single subsystem, the result demonstrates that substantial errors can emerge due to the neglect of spin-dependence in the embedding potential.

3.4.2.2 WFT-in-DFT Embedding

We now consider WFT-in-DFT embedding for the hexaaquairon(II) cation, employing the same subsystem partitioning as in the DFT-in-DFT embedding calculations (Fig. 3.3(b)). The hexaaquairon(II) cation is a benchmark system for spin splittings in transition metal complexes.[66] We initially discuss results for MP2 embedding to compare the U-WFT-in-DFT and RO-WFT-in-DFT approaches, and we then present results obtained using CCSD(T) embedding.

Fig. 4.2 presents results for the low-spin/high-spin energy difference (ΔE_{LH}) obtained using MP2, KS-DFT, and MP2-in-DFT embedding; detailed values are reported in Table 3.1. For KS-DFT calculations of ΔE_{LH}, the energy for the high-spin state of the hexaaquairon(II) cation was obtained at the UKS-DFT level of theory. The WFT-in-DFT embedding energy for the low-spin state of the hexaaquairon(II) cation is obtained using closed-shell WFT-in-DFT (Sec. II B), while the high-spin state is treated using either U-WFT-in-DFT or RO-WFT-in-DFT (Sec. III A 2). The KS-DFT results (red in Fig. 4.2) exhibit strong dependence on the XC functional, with hybrid functionals underestimating ΔE_{LH} to a somewhat lesser degree than the semi-local functionals.

Fig. 4.2 clearly illustrates that the RO-MP2-in-DFT results (blue) are in better agreement with the full MP2 calculation than the corresponding U-MP2-in-DFT results (green), particularly for semi-local XC functionals. Removal of spin-contamination in the WFT calculation reduces the energy of the high-spin state RO-WFT-in-DFT calculation with respect to that obtained using U-WFT-in-DFT.

Another important observation from Fig. 4.2 is that the dependence of ΔE_{LH} on the DFT XC functional is greatly reduced in the embedding calculation, even though only the single transition metal atom is treated at the WFT level. The spread of values obtained at the KS-DFT level of theory is over 6000 cm^{-1}, which is reduced by a factor of 3 in the RO-MP2-in-DFT embedding calculations.

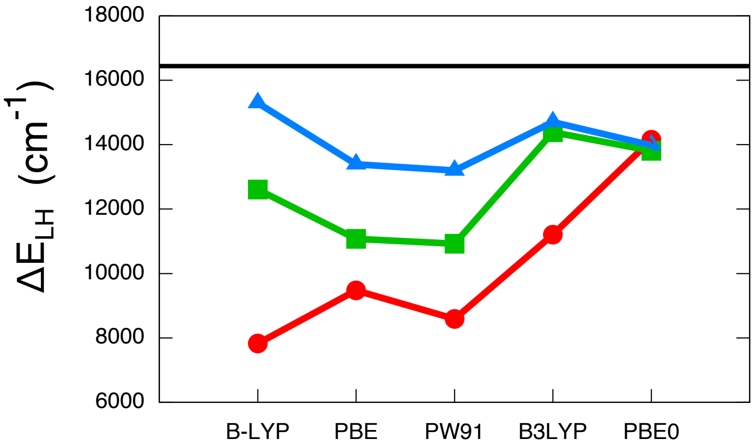

Figure 3.4: MP2-in-DFT embedding for the hexaaquairon(II) cation. High-spin/low-spin splitting energies obtained using KS-DFT (red, circles), U-MP2-in-DFT (green, squares), and RO-MP2-in-DFT (blue, triangles) with a range of different XC functionals that include B-LYP,[61,62] PBE,[58,59] PW91,[64] B3LYP,[60] and PBE0.[65] The black line indicates the reference value of 16439 cm^{-1} obtained at the RO-MP2 level of theory; U-MP2 yields a value of 17396 cm^{-1}.

Fig. 3.5(a) presents calculations of the low-spin/high-spin splitting obtained using WFT-in-DFT calculations at the RO-CCSD(T)-in-DFT level of theory; detailed values are reported in Table 3.2. For the reference calculation obtained at the full RO-CCSD(T) level of theory,[67] no T2 amplitudes were found to exceed 0.05, indicating that a single-reference description of the wavefunction is adequate. The general

Table 3.1: High-spin/low-spin splitting energies in cm^{-1} for the hexaaquairon(II) cation obtained using KS-DFT, U-MP2-in-DFT, and RO-MP2-in-DFT with a range of different XC functionals.

Functional	KS-DFT	U-MP2-in-DFT	RO-MP2-in-DFT
B-LYP	7828	12604	15294
PBE	9479	11079	13395
PW91	8593	10924	13201
B3LYP	11206	14387	14703
PBE0	14154	13812	13979

RO-MP2 yields 16439 cm^{-1}
U-MP2 yields 17396 cm^{-1}

trend for the RO-CCSD(T)-in-DFT calculations is consistent with the results obtained from RO-MP2-in-DFT. It is again seen that the dependence of ΔE_{LH} on the XC functional is substantially reduced using RO-CCSD(T)-in-DFT embedding, and the accuracy of the KS-DFT results are generally improved by treating the transition metal atom at the WFT level. For this system, the embedded RO-CCSD(T) calculation involves correlating significantly fewer electrons than the full RO-CCSD(T) calculation, and we found that the WFT step in the RO-CCSD(T)-in-DFT calculation required approximately 50 times less wall-clock time than the full RO-CCSD(T) calculation.

Fig. 3.5(b) shows that the LDA functional[68,69] presents an interesting outlier compared to the other results in Fig. 3.5(a). Unlike the semi-local and hybrid functionals, RO-CCSD(T)-in-LDA calculations do not exhibit a significant improvement with respect to the corresponding KS-DFT result. We now show that this anomalous result arises from a density-based error in the LDA functional.

Fig. 3.5(c) and Fig. 3.5(d) present the charge on the Fe atom from a Mulliken population analysis for the low-spin state of the hexaaquairon(II) cation. Fig. 3.5(c) shows that the semi-local and hybrid functionals all yield a similar charge for the Fe atom, which is very close to that of the full (relaxed) CCSD density. In contrast, Fig. 3.5(d) reveals the LDA functional significantly underestimates the Fe atomic charge, which indicates a significant error in the calculation of the ground state density. Although the use of embedded WFT can be expected to overcome the error in the contribution to the spin-splitting energy due to the LDA functional, it cannot overcome this error in the actual ground state density due to LDA.

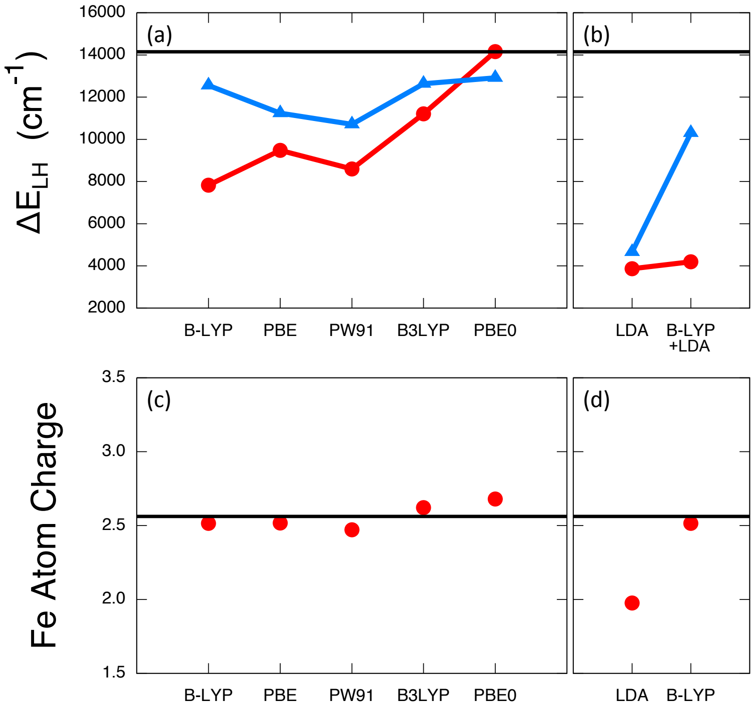

Figure 3.5: CCSD(T)-in-DFT embedding for the hexaaquairon(II) cation. (a,b) High-spin/low-spin splitting energies obtained using KS-DFT (red, circles) and RO-CCSD(T)-in-DFT (blue, triangles) with a range of different XC functionals. The B-LYP+LDA result is obtained using the B-LYP XC functional for the density calculation and the LDA XC functional for the energy calculation, as is described in the text. The black line indicates the reference value of 14149 cm^{-1} obtained at the RO-CCSD(T) level of theory. (c,d) The charge on the Fe atom is obtained using the Mulliken population analysis of the KS-DFT calculation with each functional. The relaxed CCSD density, indicated by the black line, has an Fe atomic charge of 2.56.

To confirm this interpretation, we show that removing the error in the LDA density leads to improved WFT-in-DFT estimates for the spin-splitting energy, even if the LDA functional is still employed for the DFT contributions to the energy. In Fig. 3.5(b), the B-LYP+LDA result for WFT-in-DFT embedding (blue, triangle) is obtained by *(i)* calculating the embedding potential and the subsystem densities us-

Table 3.2: High-spin/low-spin splitting energies in cm^{-1} for the hexaaquairon(II) cation obtained using KS-DFT and RO-CCSD(T)-in-DFT with a range of different XC functionals.

Functional	KS-DFT	RO-CCSD(T)-in-DFT
B-LYP	7828	12554
PBE	9479	11238
PW91	8593	10712
B3LYP	11206	12634
PBE0	14154	12912

RO-CCSD(T) yields 14149 cm^{-1}.

ing the B-LYP XC functional, *(ii)* performing the embedded WFT calculation at the CCSD(T) level, and *(iii)* using the LDA functional and CCSD(T) to evaluate the respective DFT and WFT contributions to the total energy in Eq. 3.18. The corresponding B-LYP+LDA result for KS-DFT (red, circle) is obtained by calculating the total density using KS-DFT with the B-LYP XC functional and then using the LDA functional to evaluate the KS-DFT energy. As is seen in Fig. 3.5(d), the B-LYP treatment of the subsystem densities leads to the expected partial charge for the Fe atom; it avoids the error in the electronic density that is introduced using LDA. However, the spin-splitting energy obtained using the B-LYP+LDA result for KS-DFT is essentially no better than that obtained using KS-DFT with the LDA functional (Fig.3.5(b)), indicating that simply correcting the LDA error in the density is not enough to avoid the LDA error in the energies. Finally, Fig. 3.5(b) shows that the B-LYP+LDA result for WFT-in-DFT does exhibit a substantial improvement over the corresponding KS-DFT result; this confirms that WFT embedding is able to overcome energy-based errors due to the DFT XC functional, although it is less effective at overcoming density-based errors due to the DFT XC functional.

Although we have shown that WFT-in-DFT embedding with the subsystem partitioning shown in Fig. 3.3(b) generally leads to improved estimates for the low-spin/high-spin splitting energy over KS-DFT, the same does not hold true for calculated ligation energies of the hexaaquairon(II) cation. Ligation energies calculated using RO-CCSD(T)-in-DFT embedding are essentially unchanged from those obtained using KS-DFT with the corresponding XC functional; indeed, the mean absolute difference between the computed WFT-in-DFT and KS-DFT ligation energy is only 0.6 kcal/mol per ligand across the set of functionals that includes LDA, B-LYP, PBE, PW91, B3LYP, and PBE0. Unlike the spin-splitting energy, which is highly sensitive to the electronic structure of the Fe atom and is thus impacted by the WFT subsystem description, the ligation energy is dominated by interactions between the Fe atom and the water ligands; these inter-subsystem interactions are still treated essentially at the DFT level in WFT-in-DFT embedding. An improved description for the ligation energy could be obtained by simply expanding the number of electrons that are treated at the WFT level of theory, or by including two-body correlation corrections through an embedded many-body expansion description of the system.[29]

3.5 Conclusion

In this work, we have introduced and demonstrated improved methods for the implementation of WFT-in-DFT calculations for open-shell systems and systems with low-lying virtual orbitals. A simple orbital-occupation-freezing technique is introduced to enable robust OEP calculations on systems with small HOMO-LUMO gaps, leading to accurate DFT-in-DFT and WFT-in-DFT embedding calculations on transition-metal complexes. Furthermore, the use of spin-dependent embedding potentials is shown to preserve the accuracy of open-shell DFT-in-DFT calculations in both the restricted and unrestricted orbital formulations, whereas neglect of the spin polarization leads to significant errors in both computed energies and geometries. WFT-in-DFT calculations on the hexaaquairon(II) cation reveal that the treatment of only the single transition metal atom leads to significant improvements in the accuracy of calculated spin-splittings, as well as marked reduction in the dependence of results on the DFT XC functional. Taken together, the exact embedding techniques reported and demonstrated here offer a promising approach to the robust treatment of systems for which the accuracy of WFT is required but for which the cost of the full WFT calculation is not feasible.

Bibliography

[1] A. Warshel and M. Levitt, J. Mol. Biol. **103**, 227 (1976).

[2] P. Sherwood, A. H. de Vries, S. J. Collins, S. P. Greatbanks, N. A. Burton, M. A. Vincent, and I. H. Hillier, Farad. Discuss. **106**, 79 (1997).

[3] J. L. Gao, P. Amara, C. Alhambra, and M. J. Field, J. Phys. Chem. A. **102**, 4714 (1998).

[4] H. Lin and D. G. Truhlar, Theor. Chem. Acc. **117**, 185 (2007).

[5] H. M. Senn and W. Thiel, Angew. Chem. Int. Ed. **48**, 1198 (2009).

[6] L. Hu, P. Söderhjelm, and U. Ryde, J. Chem. Theory. Comput. **7**, 761 (2011).

[7] S. Dapprich, I. Komáromi, K. S. Byun, K. Morokuma, and M. J. Frisch, J. Mol. Struct. THEOCHEM **461-462**, 1 (1999).

[8] F. Maseras and K. Morokuma, J. Comp. Chem. **16**, 1170 (1995).

[9] K. Kitaura, E. Ikeo, T. Asada, T. Nakano, and M. Uebayasi, Chem. Phys. Lett. **313**, 701 (1999).

[10] D. G. Fedorov and K. Kitaura, J. Chem. Phys. **120**, 6832 (2004).

[11] D. G. Fedorov and K. Kitaura, J. Phys. Chem. A. **111**, 6904 (2007).

[12] M. J. Field, P. A. Bash, and M. Karplus, J. Comput. Chem. **11**, 700 (1990).

[13] U. C. Singh and P. A. Kollman, J. Comput. Chem. **7**, 718 (1986).

[14] Y. Zhang, T. S. Lee, and W. Yang, J. Chem. Phys. **110**, 46 (1999).

[15] Y. Zhang, J. Chem. Phys. **122**, 024114 (2005).

[16] G. Chałasiński, M. M. Szczęśniak, P. Cieplak, and S. Scheiner, J. Chem. Phys. **94**, 2873 (1991).

[17] E. B. Kadossov, K. J. Gaskell, and M. A. Langell, J. Comput. Chem. **28**, 1240 (2007).

[18] G. Senatore and K. R. Subbaswamy, Phys. Rev. B. **34**, 5754 (1986).

[19] M. D. Johnson, K. R. Subbaswamy and G. Senatore, Phys. Rev. B. **36**, 9202 (1987).

[20] P. Cortona, Phys. Rev. B **44**, 8454 (1991).

[21] T. A. Wesolowski and A. Warshel, J. Phys. Chem. **97**, 8050 (1993).

[22] T. A. Wesolowski, in *Computational Chemistry: Reviews of Current Trends - Vol. 10*, pp. 1-82 (World Scientific, Singapore, 2006).

[23] N. Govind, Y. A. Wang, A. J. R. da Silva, and E. A. Carter, Chem. Phys. Lett. **295**, 129 (1998).

[24] P. Huang and E. A. Carter, J. Chem. Phys. **135**, 194104 (2011).

[25] P. Elliott, K. Burke, M. H. Cohen, and A. Wasserman, Phys. Rev. A **82**, 024501 (2010).

[26] J. Nafziger, Q. Wu, and A. Wasserman, J. Chem. Phys. **135**, 234101 (2011).

[27] J. D. Goodpaster, N. Ananth, F. R. Manby, and T. F. Miller, III, J. Chem. Phys. **133**, 084103 (2010).

[28] J. D. Goodpaster, T. A. Barnes, and T. F. Miller, III, J. Chem. Phys. **134**, 164108 (2011).

[29] F. R. Manby, M. Stella, J. D. Goodpaster, and T. F. Miller, III, J. Chem. Theory Comput. **8**, 2564 (2012).

[30] O. Roncero, M. P. de Lara-Castells, P. Villarreal, F. Flores, J. Ortega, M. Paniagua, and A. Aguado, J. Chem. Phys. **129**, 184104 (2008).

[31] O. Roncero, A. Zanchet, P. Villarreal, and A. Aguado, J. Chem. Phys. **131**, 234110 (2009).

[32] S. Fux, K. Kiewish, C. R. Jacob, J. Neugebauer, and M. Reiher, Chem. Phys. Lett. **461**, 353 (2008).

[33] S. Fux, C. R. Jacob, J. Neugebauer, L. Visscher, and M. Reiher, J. Chem. Phys. **132**, 164101 (2010).

[34] A. S. P. Gomes, C. R. Jacob, and L. Visscher, Phys. Chem. Chem. Phys. **10**, 5353 (2008).

[35] C. Huang, M. Pavone, and E. A. Carter, J. Chem. Phys. **134**, 154110 (2011).

[36] A. Solovyeva, M. Pavanello, and J Neugebauer, J. Chem. Phys. **136**, 194104 (2012).

[37] C. R. Jacob, J. Neugebauer, and L. Visscher, J. Comput. Chem. **29**, 1011 (2008).

[38] M. Iannuzzi, B. Kirchner, and J. Hutter, Chem. Phys. Lett. **421**, 16 (2006).

[39] J. W. Kaminski, S. Gusarov, T. A. Wesolowski, and A. Kovalenko, J. Phys. Chem. A. **114**, 6082 (2010).

[40] Ł. Rajchel, P. S. Żuchowski, M. M. Szczęśniak, and G. Chałasiński, Chem. Phys. Lett. **486**, 160 (2010).

[41] A. W. Götz, S. M. Beyhan, and L. Visscher, J. Chem. Theory Comput. **5**, 3161 (2009).

[42] A. S. P. Gomes and C. R. Jacob, Annu. Rep. Prog. Chem., Sect. C: Phys. Chem. **108**, 222 (2012).

[43] Q. Wu and W. Yang, J. Phys. Chem. **118**, 2498 (2003).

[44] F. A. Bulat, T. Heaton-Burgess, A. J. Cohen, and W. Yang, J. Chem. Phys. **127**, 174101 (2007).

[45] Q. Wu, P. W. Ayers, and Y. Zhang, J. Chem. Phys. **131**, 164112 (2009).

[46] C. R. Jacob, J. Chem. Phys. **135**, 244102 (2011).

[47] Q. S. Zhao and R. G Parr, Phys. Rev. A **46**, 2337 (1992).

[48] Q. S. Zhao and R. G Parr, J. Chem. Phys. **98**, 543 (1993).

[49] Q. S. Zhao, R. C. Morrison, and R. G Parr, Phys. Rev. A **50**, 2138 (1994).

[50] S. Sharifzadeh, P. Huang, and E. A. Carter, Chem. Phys. Lett. **470**, 347 (2009).

[51] T. Klüner, N. Govind, Y. A. Yang, and E. A. Carter, J. Chem. Phys. **116**, 42 (2002).

[52] T. A. Wesolowski, Phys. Rev. A **77**, 012504 (2008).

[53] P. Huang and E. A. Carter, J. Chem. Phys. **125**, 084102 (2006).

[54] S. Sharifzadeh, P. Huang, and E. A. Carter, J. Phys.: Condens. Matter **21**, 355501 (2009).

[55] A. Mordecai, in *Nonlinear Programming: Analysis and Methods*, (Dover Publishing, 2003).

[56] H.-J. Werner, P. J. Knowles, R. Lindh, F. R. Manby, M. Schütz et al. Molpro, version 2012.1; Cardiff University: Cardiff, U. K.; Universitt Stuttgart: Stuttgart, Germany, 2012. See www.molpro.net.

[57] T. A. Wesolowski, J. Chem. Phys. **106**, 8516 (1997).

[58] J. P. Perdew, K. Burke, and M. Ernzerhof, Phys. Rev. Lett. **77**, 3865 (1996).

[59] J. P. Perdew, K. Burke, and M. Ernzerhof, Phys. Rev. Lett. **78**, 1396 (1997).

[60] A. D. Becke, J. Chem. Phys. **98**, 5648 (1993).

[61] A. D. Becke, Phys. Rev. A **38**, 3098 (1988).

[62] C. Lee, W. Yang, and R. G. Parr, Phys. Rev. B **37**, 785 (1988).

[63] J. P. Perdew, Phys. Rev. B **33**, 8822 (1986).

[64] J. P. Perdew, J. A. Chevary, S. H. Vosko, K. A Jackson, M. R. Pederson, D. J. Singh, and C. Fiolhais, Phys. Rev. B. **46**, 6671 (1992).

[65] C. Adamo and V. Barone, J. Chem. Phys. **110**, 6158 (1999).

[66] A. Fouqueau, S. Mer, M. E. Casida, L. M. L. Daku, A. Hauser, T. Mineva, and F. Neese, J. Chem. Phys. **120**, 9473 (2004).

[67] P. J. Knowles, C. Hampel, and H.-J. Werner, J. Chem. Phys. **99**, 5219 (1993).

[68] J. C. Slater, Phys. Rev. **81**, 385-390 (1951).

[69] S. H. Vosko, L. Wilk, and M. Nusair, Can. J. Phys. **58**, 1200-1211 (1980).

Chapter 4

Accurate and systematically improvable density functional theory embedding for correlated wavefunctions

4.1 Introduction

The observation that many chemical processes are predominately governed by changes within a localized subsystem has motivated the development of a number of multiscale strategies.[1–24] The success of such methods is contingent on the availability of a sufficiently accurate description of the environment, as well as a suitable model for the coupling between subsystems. Density functional theory (DFT) provides an ideal framework for multiscale embedding.[17–24] In these approaches, an electronic structure calculation on a chemical system is partitioned into calculations on two subsystems: subsystem A, which is treated using an accurate wavefunction theory (WFT), and subsystem B, which is treated using the more computationally efficient DFT method.[25–36] Our projector-based WFT-in-DFT embedding approach has the advantage of offering a framework that is both exact for cases in which both subsystems are treated using DFT (DFT-in-DFT embedding) and efficient for calculations on large systems.[36,37]

Although projector-based embedding is numerically exact for DFT-in-DFT embedding, it is clear that some error is introduced into any practical WFT-in-DFT embedding calculation. Because the energy of the DFT environment is calculated at the DFT level, this contribution will be no more accurate than that of a standard DFT calculation. Evaluation of the interaction between subsystems is also handled using DFT theory, which introduces errors into both the embedding potential of the WFT subsystem, and the nonadditive energy between subsystems. We analyze WFT-in-DFT embedding by decomposing the error into these three contributions, and use the results to suggest further improvements to projector-based embedding. The analysis is performed through careful comparison with local coupled-cluster calculations.

We also analyze the errors of a number of embedding calculations on systems that might be expected to be particularly difficult to treat using projector-based embedding. In particular, we investigate the potential energy surface of a heterolytic bond cleavage using projector-based embedding. As with other local correlation methods, our embedding method exhibits discontinuities in the potential energy surface; however, these discontinuities are small and decrease as the WFT subsystem is expanded. Finally, we consider reactions involving highly conjugated molecules, and find that projector-based embedding produces reliably accurate results for reactions involving moderate changes in polarization.

4.2 Projector-Based Embedding

The projector-based embedding method provides a rigorous framework for embedding a DFT or WFT subsystem description in a DFT environment.[36] In this approach, a Kohn-Sham (KS)-DFT calculation is first performed over the full system. The resulting occupied molecular orbitals (MOs), $\{\phi_i\}$, are then localized and partitioned into the sets $\{\phi_i^{\mathrm{A}}\}$ and $\{\phi_i^{\mathrm{B}}\}$, which correspond to subsystems A and B, respectively. These two sets of orbitals are used to form the density matrices of subsystems A and B in the atomic orbital basis, γ^{A} and γ^{B}.

Next, the subsystem Fock matrix is formed for the embedding calculation, such that

$$\mathbf{f}^{\mathrm{A}} = \mathbf{h}^{\mathrm{A\ in\ B}}[\gamma^{\mathrm{A}}, \gamma^{\mathrm{B}}] + \mathbf{g}[\tilde{\gamma}^{\mathrm{A}}], \tag{4.1}$$

where the embedded core Hamiltonian is

$$\mathbf{h}^{\mathrm{A\ in\ B}}[\gamma^{\mathrm{A}}, \gamma^{\mathrm{B}}] = \mathbf{h} + \mathbf{g}[\gamma^{\mathrm{A}} + \gamma^{\mathrm{B}}] - \mathbf{g}[\gamma^{\mathrm{A}}] + \mu \mathbf{P}^{\mathrm{B}}. \tag{4.2}$$

Here, $\mathbf{h}$ is the standard one-electron core Hamiltonian, $\mathbf{g}$ includes all the two-electron terms, $\mathbf{P}^{\mathrm{B}}$ is a projection operator, and μ is a level-shift parameter; $\tilde{\gamma}^{\mathrm{A}}$ is the density matrix associated with the MO eigenstates of $\mathbf{f}^{\mathrm{A}}$, $\{\tilde{\phi}_i^{\mathrm{A}}\}$. The projection operator is given by

$$P^{\mathrm{B}}_{\alpha\beta} \equiv \langle b_\alpha | \left\{ \sum_{i \in \mathrm{B}} |\phi_i^{\mathrm{B}}\rangle\langle\phi_i^{\mathrm{B}}| \right\} |b_\beta\rangle, \tag{4.3}$$

where α, β label the atomic orbital basis functions.[38–45] In the limit of $\mu \to \infty$, the MOs in $\{\tilde{\phi}_i^{\mathrm{A}}\}$ are constrained to be mutually orthogonal with the MOs of subsystem B;[36,37] if in addition the same density functional is used for all calculations, the MOs $\{\tilde{\phi}_i^{\mathrm{A}}\}$ coincide with the original orbitals $\{\phi_i^{\mathrm{A}}\}$.

A self-consistent field optimization, using the Fock matrix $\mathbf{f}^{\mathrm{A}}$, is performed to obtain $\tilde{\gamma}^{\mathrm{A}}$, and the final DFT-in-DFT energy is

$$\begin{aligned} E_{\mathrm{DFT}}[\tilde{\gamma}^{\mathrm{A}}; \gamma^{\mathrm{A}}, \gamma^{\mathrm{B}}] = \\ & E_{\mathrm{DFT}}[\tilde{\gamma}^{\mathrm{A}}] + E_{\mathrm{DFT}}[\gamma^{\mathrm{B}}] + E^{\mathrm{nad}}_{\mathrm{DFT}}[\gamma^{\mathrm{A}}, \gamma^{\mathrm{B}}] \\ & + \mathrm{tr}\left[(\tilde{\gamma}^{\mathrm{A}} - \gamma^{\mathrm{A}})(\mathbf{h}^{\mathrm{A\ in\ B}}[\gamma^{\mathrm{A}}, \gamma^{\mathrm{B}}] - \mathbf{h})\right], \end{aligned} \tag{4.4}$$

where E_{DFT} is the standard DFT energy (evaluated with core-Hamiltonian $\mathbf{h}$) and $E^{\mathrm{nad}}_{\mathrm{DFT}}[\gamma^{\mathrm{A}}, \gamma^{\mathrm{B}}]$ is the nonadditive energy between the subsystem densities. The last term is a first-order correction to the difference between $E^{\text{nad}}_{\text{DFT}}[\gamma^{\text{A}}, \gamma^{\text{B}}]$ and $E^{\text{nad}}_{\text{DFT}}[\tilde{\gamma}^{\text{A}}, \gamma^{\text{B}}]$.[31] In the limit of $\mu \to \infty$, $\tilde{\gamma}^{\text{A}} = \gamma^{\text{A}}$ and the DFT-in-DFT embedding energy is identical to the energy from the corresponding KS calculation performed over the full system; as a result, the projector-based approach is numerically exact for DFT-in-DFT embedding calculations.[36] In practice, a large finite value of μ is used, and an additional perturbative correction to the energy can performed;[36] for appropriate values of μ this correction is typically far smaller than the energy differences discussed in this paper and is thus neglected throughout. Furthermore, as has been previously emphasized, this embedding scheme is exact for any self-consistent field method, such as Hartree-Fock (HF) theory.[36,37]

The nonadditive contribution to the energy, $E^{\text{nad}}_{\text{DFT}}[\gamma^{\text{A}}, \gamma^{\text{B}}]$, can be decomposed into electrostatic and exchange-correlation contributions

$$E^{\text{nad}}_{\text{DFT}}[\gamma^{\text{A}}, \gamma^{\text{B}}] = J^{\text{nad}}[\gamma^{\text{A}}, \gamma^{\text{B}}] + E^{\text{nad}}_{\text{xc}}[\gamma^{\text{A}}, \gamma^{\text{B}}], \tag{4.5}$$

where

$$J^{\text{nad}}[\gamma^{\text{A}}, \gamma^{\text{B}}] = \int \mathrm{d}r_1 \int \mathrm{d}r_2 \, \frac{\gamma^{\text{A}}(1)\gamma^{\text{B}}(2)}{r_{12}} \tag{4.6}$$

and

$$E^{\text{nad}}_{\text{xc}}[\gamma^{\text{A}}, \gamma^{\text{B}}] = E_{\text{xc}}[\gamma^{\text{A}} + \gamma^{\text{B}}] - E_{\text{xc}}[\gamma^{\text{A}}] - E_{\text{xc}}[\gamma^{\text{B}}]. \tag{4.7}$$

The electrostatic term, J^{nad}, is easily evaluated, and although the exact form of E_{xc} is unknown, approximate functionals are well established. Since the embedded MOs $\{\tilde{\phi}^{\text{A}}_i\}$ are orthogonal to those in subsystem B, there is no nonadditivity in the kinetic energy. This removes the requirement of performing optimized effective potential calculations[20,21,23,24,30,31] or using approximate nonadditive kinetic energy functionals.

The projector-based formalism easily allows for WFT-in-DFT embedding, in which subsystem A is treated using a WFT-level description and subsystem B is described at the DFT level.[36] This is achieved by replacing the standard one-electron core Hamiltonian with the embedded core Hamiltonian of Eq. 4.2. The electronic energy from the WFT-in-DFT embedding approach is

$$\begin{aligned} E_{\mathrm{WFT}}[\Psi^{\mathrm{A}};\gamma^{\mathrm{A}},\gamma^{\mathrm{B}}] = {} & \langle\Psi^{\mathrm{A}}|\hat{H}^{\mathrm{A\ in\ B}}[\gamma^{\mathrm{A}},\gamma^{\mathrm{B}}]|\Psi^{\mathrm{A}}\rangle \\ & - \mathrm{tr}\left[\gamma^{\mathrm{A}}(\mathbf{h}^{\mathrm{A\ in\ B}}[\gamma^{\mathrm{A}},\gamma^{\mathrm{B}}] - \mathbf{h})\right] \\ & + E_{\mathrm{DFT}}[\gamma^{\mathrm{B}}] \\ & + E^{\mathrm{nad}}_{\mathrm{DFT}}[\gamma^{\mathrm{A}},\gamma^{\mathrm{B}}], \end{aligned} \tag{4.8}$$

where $|\Psi^{\mathrm{A}}\rangle$ is the embedded wavefunction from the WFT method, and $\hat{H}^{\mathrm{A\ in\ B}}[\gamma^{\mathrm{A}},\gamma^{\mathrm{B}}]$ is the WFT Hamiltonian resulting from replacing the standard one-electron core Hamiltonian with the embedded core Hamiltonian. The term $\mathrm{tr}\left[\tilde{\gamma}^{\mathrm{A}}(\mathbf{h}^{\mathrm{A\ in\ B}}[\gamma^{\mathrm{A}},\gamma^{\mathrm{B}}] - \mathbf{h})\right]$ is included in the first term of Eq. 4.8 and thus does not show up in the first-order correction term, as it did in Eq. 4.4.

4.3 Results I: Sources of error in WFT-in-DFT embedding

4.3.1 Term-By-Term Comparison with LCSSD(T)

We now formulate an approach to compare the individual terms in the energy expression of a CCSD(T)-in-DFT embedding calculation with the corresponding values calculated at the CCSD(T) level.[46] To do this, we first recognize that the local (L)CCSD(T) method by Schütz and Werner[47,50–52] becomes exactly equivalent to the canonical CCSD(T) method when all orbital pairs are correlated and all excitation domains are set to the full virtual basis. The terms in the LCCSD(T) energy expression, in turn, can be organized in a way that enables direct comparison to the terms in the CCSD(T)-in-DFT embedding energy expression.

The LCCSD(T) energy can be decomposed as a function of the amplitudes and the atomic-orbital density matrices as

$$\begin{aligned} &E_{\mathrm{LCCSD(T)}}[T_1, T_2, T_3; \gamma^{\mathrm{A}}, \gamma^{\mathrm{B}}] = \\ &\quad + E_{\mathrm{HF}}[\gamma^{\mathrm{A}}] + E^{\mathrm{A}}_{\mathrm{(S)}} + E^{\mathrm{A}}_{\mathrm{(D)}} + E^{\mathrm{A}}_{\mathrm{(T)}} \\ &\quad + E_{\mathrm{HF}}[\gamma^{\mathrm{B}}] + E^{\mathrm{B}}_{\mathrm{(S)}} + E^{\mathrm{B}}_{\mathrm{(D)}} + E^{\mathrm{B}}_{\mathrm{(T)}} \\ &\quad + E^{\mathrm{nad}}_{\mathrm{HF}}[\gamma^{\mathrm{A}}, \gamma^{\mathrm{B}}] + E^{\mathrm{nad}}_{\mathrm{(D)}} + E^{\mathrm{nad}}_{\mathrm{(T)}}, \end{aligned} \tag{4.9}$$

where E_{HF} is the HF energy and $E^{\mathrm{nad}}_{\mathrm{HF}}[\gamma^{\mathrm{A}}, \gamma^{\mathrm{B}}]$ is the same as Eq. 4.5, except with the corresponding exchange terms replacing $E^{\mathrm{nad}}_{\mathrm{xc}}[\gamma^{\mathrm{A}}, \gamma^{\mathrm{B}}]$. When the full virtual space is included, the singles are additive and thus there is no nonadditive component. The nonadditive correlation for the double-excitation terms is simply

$$E^{\mathrm{nad}}_{\mathrm{(D)}} = E_{\mathrm{(D)}} - E^{\mathrm{A}}_{\mathrm{(D)}} - E^{\mathrm{B}}_{\mathrm{(D)}} \tag{4.10}$$

and likewise for the triple-excitation correlation energy.

The correlation energy from the single excitations within subsystem A is given by

$$E^{\mathrm{A}}_{\mathrm{(S)}} = 2 \sum_{i \in A} \mathbf{f}^{i\dagger} \mathbf{t}^{i} \tag{4.11}$$

where the summation spans the occupied orbitals of subsystem A, $\mathbf{f}^i$ is the internal-external part of the Fock matrix in vector form, and $\mathbf{t}^i$ are the single excitation amplitudes in vector form.[47]

The correlation energy from the double excitations within subsystem A is given by

$$E^{\mathrm{A}}_{(\mathrm{D})} = \sum_{\substack{i\geq j\\ i,j\in A}} (2-\delta_{ij})\mathrm{tr}[\mathbf{L}^{ij}\mathbf{C}^{ij}], \tag{4.12}$$

where the summation spans the occupied orbitals of subsystem A, and $\mathbf{L}^{ij}$ are the internal coulomb and exchange matrices. The matrix elements of $\mathbf{C}^{ij}$ are given by $C^{ij}_{r,s} = T^{ij}_{r,s} + t^i_r t^j_s$, where $T^{ij}_{r,s}$ and t^i_r are the double and single excitation amplitudes, respectively.[47]

Finally, the correlation energy from the triple excitations within subsystem A is given by

$$\begin{aligned} E^{\mathrm{A}}_{(\mathrm{T})} = \sum_{\substack{i\geq j\geq k\\ i,j,k\in A}} (2-\delta_{ij}-\delta_{jk}) \Bigg(&\sum_{rstr'} t^i_{r'} S_{rr'}\,(js|kt)\,X^{ijk}_{rst} \\ &+ \sum_{rsts'} t^j_{s'} S_{ss'}\,(ir|kt)\,X^{ijk}_{rst} \\ &+ \sum_{rstt'} t^k_{t'} S_{tt'}\,(ir|js)\,X^{ijk}_{rst} + \sum_{rst} W^{ijk}_{rst} X^{ijk}_{rst} \Bigg), \end{aligned} \tag{4.13}$$

where the first summation spans the occupied orbitals of subsystem A, the indices i, j, k represent occupied orbitals, and the indices r, s, t represent unoccupied orbitals. $S_{rr'}$ is an element of the overlap matrix of the projected atomic orbitals, $(ir|js)$ are two-electron integrals, and $\tilde{t}^i_r$ are the single amplitudes. X^{ijk}_{rst} is defined as $X^{ijk}_{rst} = 4T^{ijk}_{rst} - 2T^{ijk}_{rts} - 2T^{ijk}_{tsr} - 2T^{ijk}_{srt} + T^{ijk}_{trs} + T^{ijk}_{str}$ where T^{ijk}_{rst} are the triples amplitudes. The tensor element W^{ijk}_{rst} contains the double-excitation amplitudes, T^{ij}_{rs}.[50,51]

4.3.2 Calculation Details

All geometry optimizations are performed using Gaussian09[53] and are provided in the supplemental information. All other calculations are performed in Molpro 2012.1.[54]

In all calculations the orbitals are localized using Pipek-Mezey localization.[55] The atoms associated with subsystem A for each reaction are given in the supplemental information. Any localized orbital with a Löwdin charge of 0.4 on an atom associated with subsystem A is included in the set of orbitals associated with subsystem A. All calculations employ a level shift parameter μ, which is set to 10^6 au. All KS-DFT calculations employ a large grid for the exchange-correlation functional evaluation, achieved by specifying the Molpro option GRID=10^{-10}. For computational efficiency, all LCCSD(T) calculations employ density fitting (DF), and the triples are approximated using the noniterative (T0) procedure.[50,51]

To enable the rigorous comparison of terms from the LCCSD(T) calculation and the embedding calculation, some care must be taken. First, all orbital pairs are correlated to recover the energy from canonical CCSD(T). Second, the choice of orbitals must be consistent between the LCCSD(T) and CCSD(T)-in-DFT embedding calculations.

In the WFT-in-DFT embedding method, subsystem B comprises KS MOs, and thus evaluation of the errors resulting from using the DFT energy of subsystem B requires the use of KS MOs as the reference MOs. The difference between canonical CCSD(T) using the HF reference and DF-LCCSD(T0) using the KS reference is within 0.3 mE_h for all reactions discussed in this paper, which is smaller than the errors that will be discussed in the next sections; therefore, in the next section we will simply refer to terms calculated from DF-LCCSD(T0) as CCSD(T).

Likewise, consistent evaluation of the error arising from the embedding potential requires that the reference MOs for the embedded CCSD(T) calculation on subsystem A be obtained from the corresponding DFT calculation. This selection of reference MOs is used only throughout Sec. III C. In all other sections, the reference MOs of the embedded CCSD(T) calculation are chosen to be the set of MOs resulting from an embedded HF calculation. We note that the difference between CCSD(T)-

in-DFT embedding where the MOs for subsystem A are obtained from an embedded DFT calculation compared to an embedded HF calculation is within 0.2 mE_h for the reactions considered in Sec. III C.

Below we analyze the contributions to the embedding error for a set of six energies associated with different reactions. All of the chosen reactions are large enough to involve partitioning across a covalent bond, but also small enough to allow for calculation of the full CCSD(T) reference energy. The reactions considered are given in Table I.

The data set consists of the following reactions: (1) activation energy for the symmetric $\mathrm{S_N2}$ reaction of $\mathrm{Cl^-}$ and propyl chloride; (2) acid hydrolysis of dimethylether to form methanol; (3) deprotonation of the phenol hydroxyl group; (4) ring-closing isomerization of 3-methylene-1-heptene to form butylcylobutane; (5) the Diels-Alder reaction of 2-methoxy-1,3-butadiene with methyl vinyl ketone; and (6) the activation energy for the Diels-Alder reaction. The geometries are provided in the supplemental information.

	reaction	$E/\mathrm{m}E_\mathrm{h}$
1	$\mathrm{S_N2}$ activation barrier	7.8
2	acid hydrolysis	177.8
3	phenol deprotonation	568.8
4	ring closing	10.6
5	Diels-Alder reaction	63.1
6	Diels-Alder barrier	34.0

Table 4.1: CCSD(T) reaction energies and barriers in the test set obtained using cc-pVTZ with aug-cc-pV(T+d)Z on Cl, and aug-cc-pVTZ for all atoms for reactions 2–4.[56,57] For ease of error analysis, we adopt a sign convention in which all reactions or activation processes are positive in energy. Geometries were obtained using B3LYP with 6-311G*++ (reaction 1), def2-TZVP (reactions 2–4), or 6-31G* (reactions 5, 6).[58–61]

4.3.3 Sources of Error in WFT-in-DFT embedding

4.3.3.1 Error from the Embedding Potential

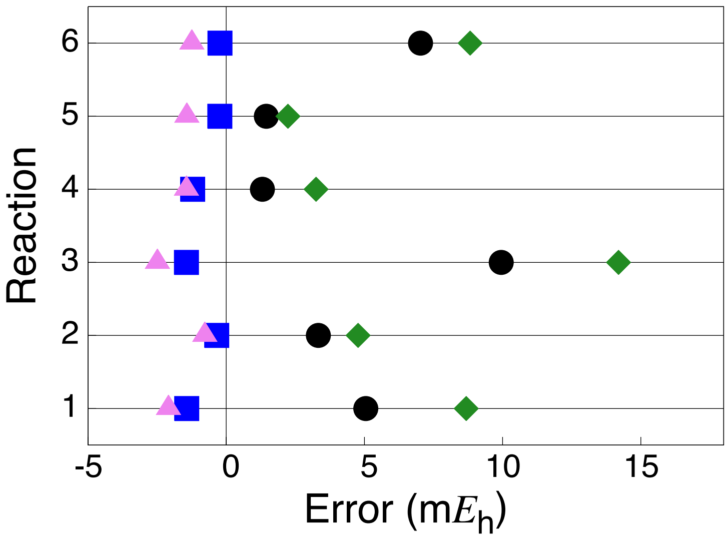

Figure 4.1: The error arising from the embedding potential (blue squares), the DFT energy of subsystem B (violet triangles), and the nonadditive exchange-correlation energy (green diamonds) compared to the total CCSD(T)-in-B3LYP embedding error (black circles). CCSD(T) calculations performed on the full system are used as the reference. The largest source of error is the nonadditive exchange-correlation energy functional.

Now we discuss how comparison of terms in the energy expressions for CCSD(T) and CCSD(T)-in-DFT embedding can be used to determine the error arising from the embedding potential. The energy of subsystem A from the CCSD(T) calculation is the sum of the HF energy (using the KS density) and the correlation energy of subsystem A,

$$E^{\mathrm{A}}_{\mathrm{CCSD(T)}} = E_{\mathrm{HF}}[\gamma^{\mathrm{A}}] + E^{\mathrm{A}}_{\mathrm{(S)}} + E^{\mathrm{A}}_{\mathrm{(D)}} + E^{\mathrm{A}}_{\mathrm{(T)}}. \tag{4.14}$$

The total energy of subsystem A from a CCSD(T)-in-DFT embedding calculation is

$$\begin{aligned} E^{\mathrm{A}}_{\mathrm{emb}} &= \langle \Psi^{\mathrm{A}} | \hat{H}^{\mathrm{A\ in\ B}}[\gamma^{\mathrm{A}}, \gamma^{\mathrm{B}}] | \Psi^{\mathrm{A}} \rangle \\ &\quad - \mathrm{tr}\left[\gamma^{\mathrm{A}}(\mathbf{h}^{\mathrm{A\ in\ B}}[\gamma^{\mathrm{A}}, \gamma^{\mathrm{B}}] - \mathbf{h})\right]. \end{aligned} \tag{4.15}$$

For an embedding potential that includes all of the CCSD(T) many-body effects, the energy of $E^{\mathrm{A}}_{\mathrm{CCSD(T)}}$ and $E^{\mathrm{A}}_{\mathrm{emb}}$ would be identical; therefore, the error arising from the embedding potential is calculated as

$$E^{\mathrm{error}}_{\mathrm{pot}} = E^{\mathrm{A}}_{\mathrm{emb}} - E^{\mathrm{A}}_{\mathrm{CCSD(T)}}. \tag{4.16}$$

The error in the reaction energies arising from the embedding potential is therefore the change in $E^{\mathrm{error}}_{\mathrm{pot}}$ between products and reactants, $\Delta E^{\mathrm{error}}_{\mathrm{pot}}$.

The blue squares in Figure 4.1 show the value of $\Delta E^{\mathrm{error}}_{\mathrm{pot}}$ for the data set, compared to the total CCSD(T)-in-B3LYP embedding error shown in the black circles. For no system is the error larger than 1.5 mE_{h}, with the average error being 0.8 mE_{h}. This demonstrates a key insight of this paper, which is that the embedding potential calculated using WFT-in-DFT embedding is very accurate.

4.3.3.2 Error from Use of DFT for Subsystem B

Next, we quantify the WFT-in-DFT embedding error resulting from treating subsystem B using DFT. This error is obtained by computing

$$\begin{aligned} E^{\mathrm{B,error}}_{\mathrm{DFT}} &= E_{\mathrm{DFT}}[\gamma^{\mathrm{B}}] \\ &\quad - \left(E_{\mathrm{HF}}[\gamma^{\mathrm{B}}] + E^{\mathrm{B}}_{\mathrm{(S)}} + E^{\mathrm{B}}_{\mathrm{(D)}} + E^{\mathrm{B}}_{\mathrm{(T)}}\right), \end{aligned} \tag{4.17}$$

which allows for a direct comparison of the DFT and CCSD(T) energies of subsystem B.

The values calculated for $\Delta E^{\mathrm{B,error}}_{\mathrm{DFT}}$ are shown in Figure 4.1 as violet triangles. The largest error in this data set is 2.5 mE_{h} and the average error is 1.5 mE_{h}. These errors are larger than those resulting from the embedding potential, but are still relatively small compared to the total WFT-in-DFT embedding error. Therefore, for this data set, DFT does an adequate job describing the energy change localized within the environment and is not the dominate source of error.

4.3.3.3 Error from the Nonadditive Exchange-Correlation Energy

Finally, we analyze the error that arises from evaluation of the nonadditive exchange-correlation energy with an approximate functional. The error is obtained by computing

$$\begin{aligned} E_{\mathrm{xc}}^{\mathrm{nad,error}} &= E_{\mathrm{DFT}}^{\mathrm{nad}}[\gamma^{\mathrm{A}}, \gamma^{\mathrm{B}}] \\ &\quad - \left(E_{\mathrm{HF}}^{\mathrm{nad}}[\gamma^{\mathrm{A}}, \gamma^{\mathrm{B}}] + E_{\mathrm{corr}}^{\mathrm{nad(D)}} + E_{\mathrm{corr}}^{\mathrm{nad(T)}}\right), \end{aligned} \tag{4.18}$$

which allows for the direct comparison of the approximate density functional to the energy obtained at the CCSD(T) level.

The values for $\Delta E_{\mathrm{xc}}^{\mathrm{nad,error}}$ are given in Figure 4.1 as green diamonds. This term dominates the WFT-in-DFT embedding error, with the largest value of $\Delta E_{\mathrm{xc}}^{\mathrm{nad,error}}$ being 14.2 mE_{h}, and the average value being 7.2 mE_{h}. It is thus this term that is responsible for introducing the largest error in the WFT-in-DFT embedding methodology.

The sum of $\Delta E_{\mathrm{pot}}^{\mathrm{error}}$, $\Delta E_{\mathrm{DFT}}^{\mathrm{B,error}}$, and $\Delta E_{\mathrm{xc}}^{\mathrm{nad,error}}$ captures all of the discrepancy between the CCSD(T)-in-DFT and full CCSD(T) calculations. Due to the use of density fitting and the noniterative triples approximation used in the CCSD(T) calculation, the sum of these errors is off by an average of 0.4 mE_{h} compared to the total CCSD(T)-in-B3LYP embedding error; this makes no difference in the interpretation of the data.

To confirm that our results are not sensitive to the approximate exchange-correlation functional, we repeated the analysis using both PBE[62] and M06[63] (not shown). These conclusions are robust with respect to the approximate exchange-correlation functional. The nonadditive exchange-correlation energy remains the largest source of error, followed by the DFT energy of subsystem B. Again, we find that DFT, for all of the functionals tested, provides very accurate embedding potentials.

4.3.4 Improvement of the Nonadditive Exchange-Correlation Energy

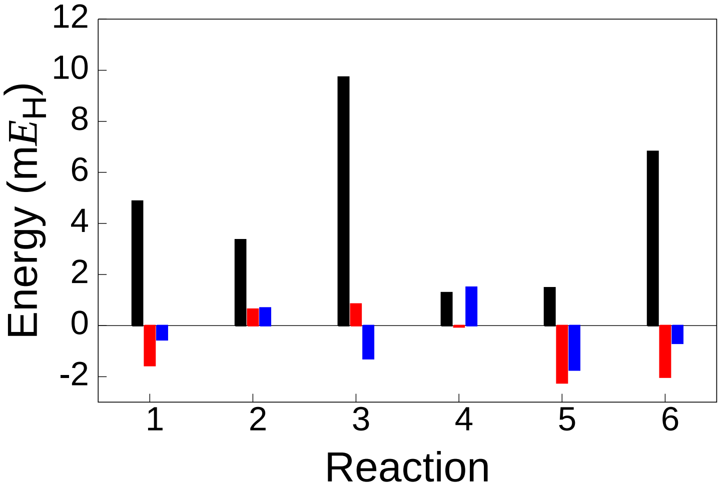

Figure 4.2: Bar graph of the error in the energy obtained from CCSD(T)-in-B3LYP embedding (black), MP2-corrected CCSD(T)-in-B3LYP embedding (red), and SOS-MP2-corrected CCSD(T)-in-B3LYP embedding. CCSD(T) calculations performed on the full system are used as the reference.

Having determined the nonadditive exchange-correlation energy to be the dominate source of error, new algorithms can be proposed to calculate this term more accurately. One approach would be to evaluate the nonadditive exchange exactly and to use a computationally cheap WFT method, such as MP2,[64] to evaluate the nonadditive correlation. The resulting correction to the WFT-in-DFT embedding energy is then

$$
\begin{aligned}
E_{\mathrm{xc}}^{\Delta\mathrm{MP2}} = E_{\mathrm{HF}}^{\mathrm{nad}}[\tilde{\gamma}_{HF}^{\mathrm{A}}, \gamma^{\mathrm{B}}] &+ \sum_{\substack{i \in A \\ j \in B}} \sum_{rs} \left(2T_{rs}^{ij} - T_{sr}^{ij}\right) K_{rs}^{ij} \\
&- E_{\mathrm{DFT}}^{\mathrm{nad}}[\gamma^{\mathrm{A}}, \gamma^{\mathrm{B}}] \\
&- \mathrm{tr}\left[(\tilde{\gamma}_{\mathrm{HF}}^{\mathrm{A}} - \gamma^{\mathrm{A}})(\mathbf{h}^{\mathrm{A\ in\ B}}[\gamma^{\mathrm{A}}, \gamma^{\mathrm{B}}] - \mathbf{h})\right],
\end{aligned}
\tag{4.19}
$$

where $\tilde{\gamma}_{\mathrm{HF}}^{\mathrm{A}}$ is the HF embedded density of subsystem A, T_{rs}^{ij} is the MP2 amplitude, and K_{rs}^{ij} are the exchange two electron integrals.[65] For the MP2 calculation the orbitals $\{\tilde{\phi}_i^{\mathrm{A}}\} \cup \{\phi_i\}_{\mathrm{B}}$ are used, which allows for the direct calculation of the MP2 correlation between the HF orbitals for A and the KS orbitals of B.

Figure 4.2 compares the CCSD(T)-in-B3LYP embedding error (black) to the MP2-corrected CCSD(T)-in-B3LYP embedding error (red). The average error of WFT-in-DFT embedding is 4.6 mE_{h}, which drops to 1.2 mE_{h} when the MP2 correction is applied. Alternatively, instead of calculating the full MP2 energy in Eq. 4.19, one could only calculate the scaled opposite spin (SOS)-MP2 correlation energy.[66] Scaling the opposite spin MP2 correlation by the usual empirical factor of 1.3 leads to the SOS-MP2-corrected CCSD(T)-in-B3LYP embedding error shown in blue in Figure 4.2. Applying the SOS-MP2 correction results in an average error of 1.1 mE_{h}, which is essentially the same error as that of the full MP2 correction, and only requires computations that scale N^4 compared to N^5 for the full MP2 energy.

The average error of standard MP2 calculations on these systems is 6.3 mE_{h} relative to CCSD(T); it is thus clear that effectiveness of the MP2 correction does not rely on the MP2 energy being particularly accurate for the full calculation. Instead, we observe that MP2 theory accurately represents the correlation energy between subsystems A and B, while not necessarily representing other correlation terms accurately. This is consistent with other local coupled-cluster methods that treat distant pairs at the MP2 level.[47]

4.4 Results II: Continuity, Convergence, and Conjugation in WFT-in-DFT embedding

4.4.1 Potential Energy Surfaces

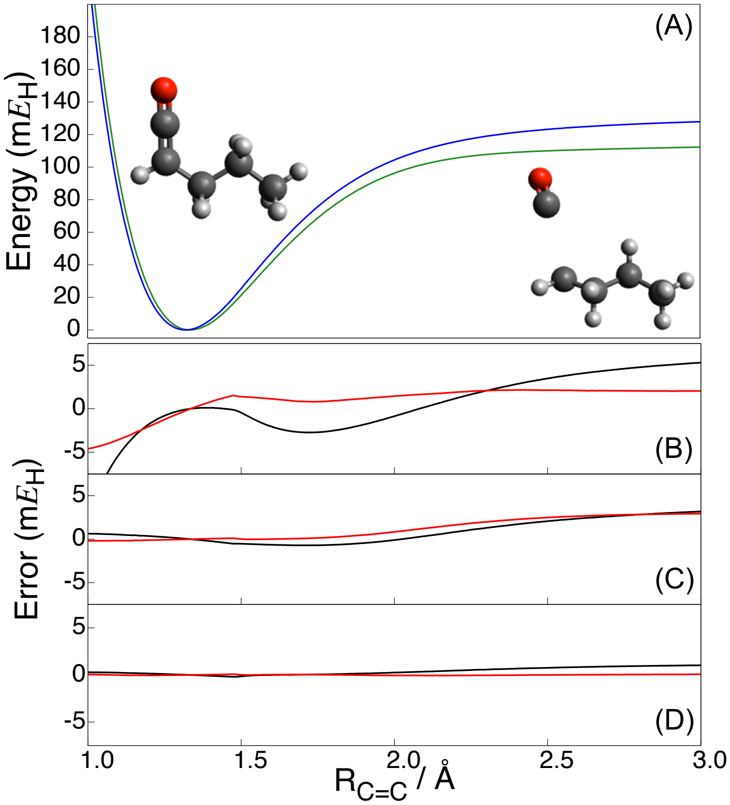

Figure 4.3: (A) Potential energy curves for the dissociation of the C-C bond in singlet 1-penten-1-one obtained using CCSD(T) (green), KS-DFT with B3LYP (blue), and CCSD(T)-in-B3LYP embedding (black). The structure was reoptimized at the HF/cc-pVDZ level of theory for each value of the C-C bond distance.[56] The O=C=CH– moiety was treated at the CCSD(T) level for the CCSD(T)-in-B3LYP embedding calculations. (B–D) The error in CCSD(T)-in-B3LYP embedding (black) and MP2-corrected CCSD(T)-in-B3LYP embedding (red) as a function of distance between the carbon-carbon double bond. The results are shown for three partitionings of the molecule, with subsystem A corresponding to (B) =C=CH–, (C) O=C=CH–, or (D) O=C=CH–CH_2–.

Next, we examine the potential energy surface for heterolytic bond cleavage. Local correlation methods show discontinuities in the potential energy surface for the heterolytic bond cleavage of CO dissociation in ketene.[67] Here, we study a related system, CO dissociation in 1-penten-1-one.

Panel A of Figure 4.3 shows potential energy curves calculated using CCSD(T), B3LYP, and CCSD(T)-in-B3LYP embedding. The cc-pVDZ basis was used for all calculations. Here, B3LYP performs relatively well near equilibrium, but overestimates the energy by up to 16 mE_h near dissociation. The CCSD(T)-in-B3LYP calculations are very accurate near equilibrium and slightly underestimate the energy near the dissociation limit. MP2-corrected CCSD(T)-in-B3LYP were also performed for this system; the results are not shown in panel A of Figure 4.3, because they are graphically indistinguishable from the uncorrected CCSD(T)-in-B3LYP results.

Panels B–D show the error in CCSD(T)-in-B3LYP embedding and MP2-corrected CCSD(T)-in-B3LYP embedding for three different subsystem partitionings of the molecule. The error and the change of the slope at the derivative discontinuity around 1.5 Å decreases by treating more of the system at the CCSD(T) level. Energy discontinuities of 50 μE_h are seen at short distances, as shown in Figure 4.7 of the supplemental information. Like other local correlation methods, abrupt changes in the localized orbitals for different nuclear configurations lead to discontinuities in the WFT-in-DFT embedding energy and its derivatives. Here, these defects are small and can be systematically controlled by increasing the size of subsystem A.

4.4.2 WFT-in-DFT Embedding of Conjugated Systems

A demanding case for any embedding methodology is the partitioning of a π-conjugated system. The applicability of WFT-in-DFT embedding to treat such systems is tested and compared to systems without conjugation.

First, we consider the dissociation of a fluoride anion from both an alkane chain (1-fluorodecane) and an alkene chain (1-fluoro-1,3,5,7,9-decapentaene). The geometries for both compounds and their dissociated products were obtained using B3LYP/def2-

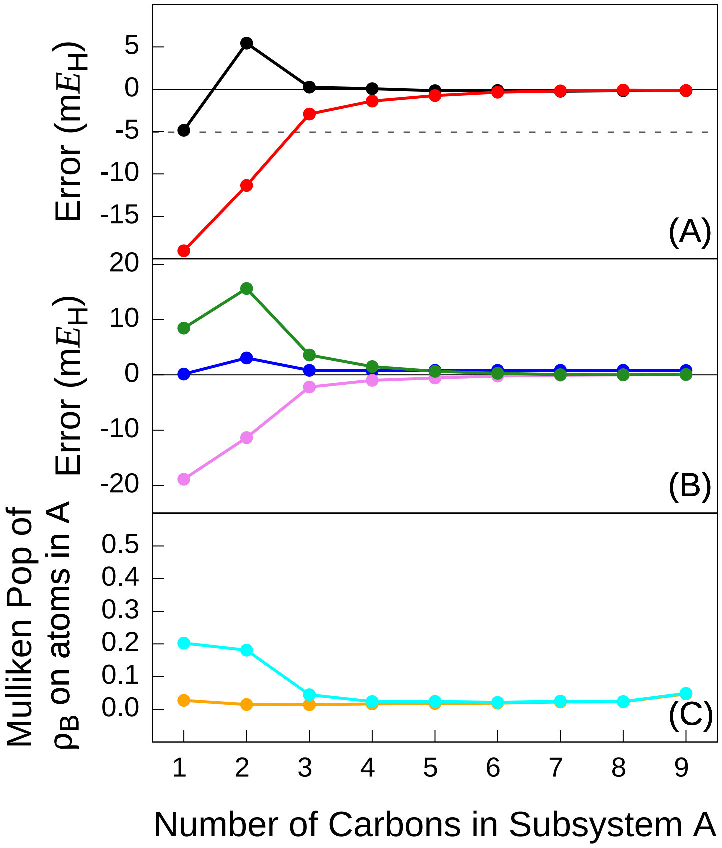

Figure 4.4: (A) The error in CCSD(T)-in-B3LYP embedding (black open circles) and MP2-corrected CCSD(T)-in-B3LYP embedding (red filled circles) as a function of the number of carbons included in subsystem A for the dissociation of the alkane. The B3LYP energy is given by the black dotted line. (B) Contributions to the WFT-in-DFT error: embedding potential (blue open circles), DFT for subsystem B (violet filled circles), and DFT for nonadditive exchange-correlation energy (green squares). (C) DFT Mulliken population of the density associated with subsystem B on the atoms in subsystem A, shown for 1-fluorodecane (black open circles) and the dissociated alkane chain (red filled circles).

TZVP. All CCSD(T) and embedding calculations were performed using the cc-pVDZ basis, with aug-cc-pVDZ for fluorine.[56]

Figure 4.4A shows the CCSD(T)-in-B3LYP with and without the MP2 correction for fluoride anion dissociation from the alkane chain. Results are provided for a number of different choices of the subsystem partitioning, and the error of both methods can be seen to rapidly vanish as more atoms are included in the WFT subsystem.

The individual sources of error in the CCSD(T)-in-B3LYP embedding calculations, computed in the same way as in Sec. 4.3.3, are shown in Figure 4.4B. Again, it is observed that the error arising from the embedding potential is small, accounting for only a small portion of the total error. Unlike previous results, the error arising from treating subsystem B at the DFT level is of similar magnitude as the nonadditive exchange-correlation energy error. As these errors are of opposite sign, evaluating the nonadditive exchange-correlation energy using DFT leads to a favorable cancellation of error. The MP2 correction only increases the accuracy of the subsystem interaction energy, and cannot be expected to correct large errors associated with the DFT energy of subsystem B.

Figure 4.4C shows the Mulliken population of the density associated with subsystem B on the atoms associated with subsystem A. In the dissociated product, the density associated with subsystem B distributes onto the atoms of subsystem A to stabilize the positive charge. We find that when the difference of this quantity is large between two configurations, there is typically a favorable cancellation of error between the error arising from treating subsystem B using DFT and the error arising from evaluating the nonadditive exchange-correlation energy using DFT. In general, we note that if the nonadditive exchange-correlation is not the dominant source of error, the MP2 correction cannot significantly improve the accuracy of the embedding calculation.

After dissociation of the fluoride anion from 1-fluoro-1,3,5,7,9-decapentaene, the subsequent geometry optimization leads to an isomerization where the proton on the second carbon moves to the first. Therefore, the analysis for this reaction begins at the second carbon. Figure 4.5A shows the error in CCSD(T)-in-B3LYP embedding (black open circles) and MP2-corrected CCSD(T)-in-B3LYP embedding (red filled circles) as a function of the number of carbons included in subsystem A for fluoride anion dissociation from 1-fluoro-1,3,5,7,9-decapentaene. Unlike the alkane case, the

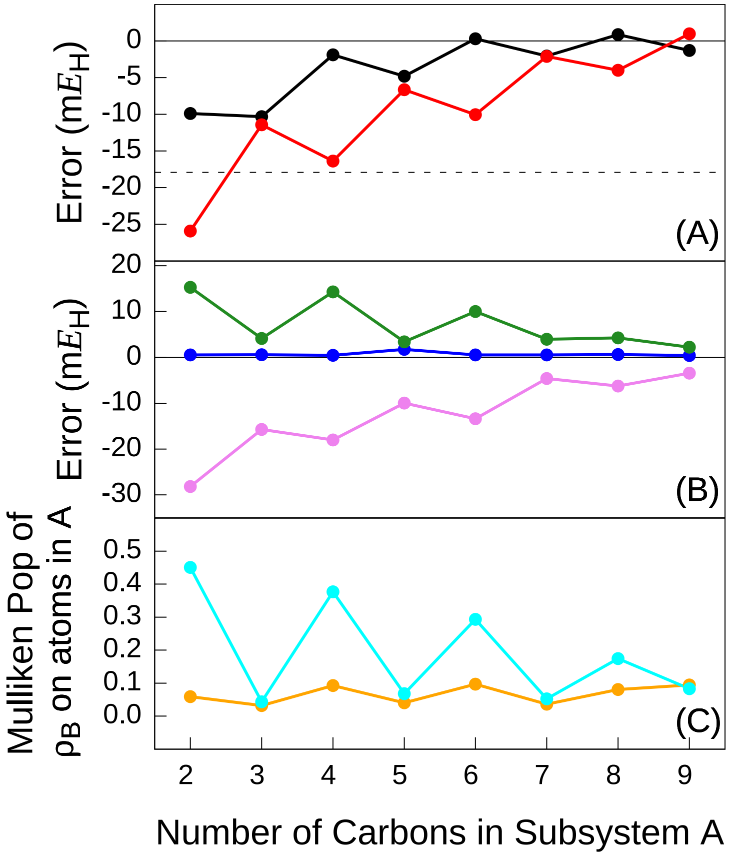

Figure 4.5: (A) The error in CCSD(T)-in-B3LYP embedding (black open circles) and MP2-corrected CCSD(T)-in-B3LYP embedding (red filled circles) as a function of the number of carbons included in subsystem A for the dissociation of the alkene. The B3LYP energy is given by the black dotted line. (B) Contributions to the WFT-in-DFT error: embedding potential (blue open circles), use of DFT for subsystem B (violet filled circles), nonadditive exchange-correlation energy (green squares). (C) DFT Mulliken population of the density associated with subsystem B on the atoms in subsystem A, shown for 1-fluoro-1,3,5,7,9-decapentaene (black open circles) and the dissociated alkene chain (red filled circles).

alkene case exhibits large errors which slowly decrease once the majority of the system is treated at the CCSD(T) level.

Figure 4.5B shows the decomposition of the contributions to the error in CCSD(T)-in-B3LYP embedding. In this calculation, the error arising from treating subsystem B using DFT is the dominate source of error. This explains why the error remains large until the majority of the system is treated at the CCSD(T) level, and why the MP2-correction is insufficient to reduce the error.

Figure 4.5C shows the Mulliken population of the density associated with subsystem B on the atoms associated with subsystem A for the alkene case. As with the alkane case, a large difference in this quantity is seen between the fluorinated and defluorinated compounds. This observation provides insight into why the error from the DFT energy of B contributes strongly to the error of the embedding calculations.

The magnitude of the change in the dipole moment between the fluorinated and defluorinated compounds is show in Table 4.2 for KS-DFT with B3LYP and CCSD. In the alkane dissociation, the change in the dipole moment is large, demonstrating a small polarizability, and there is good agreement between KS-DFT and CCSD. In the alkene dissociation, the change in dipole moment is considerably smaller than the alkane case, demonstrating that the density polarizes to stabilize charge. For the alkene, there is large disagreement between KS-DFT and CCSD, demonstrating the known failure of DFT to accurately treat polarizability though a π-conjugated system.[68] Therefore, when there are large errors associated with KS-DFT, these large errors will affect the DFT energy of subsystem B, causing large WFT-in-DFT embedding errors. We emphasize that for cases in which DFT does correctly describe the polarization of the environment, this large source of error does not arise. The failure of WFT-in-DFT embedding in Figure 4.5 is not a failure of embedding itself, but rather a failure of DFT to accurately treat the polarizability of π-conjugated systems.

	method	dissociation	exchange
alkane	B3LYP	7.338	0.781
	CCSD	7.539	0.802
alkene	B3LYP	1.702	0.551
	CCSD	3.034	0.630

Table 4.2: The magnitude of the change in the dipole moment between products and reactants for the dissociation of F^- from the alkane and alkene chains, as well as the corresponding magnitudes for the H-F exchange reaction. Values are reported in atomic units.

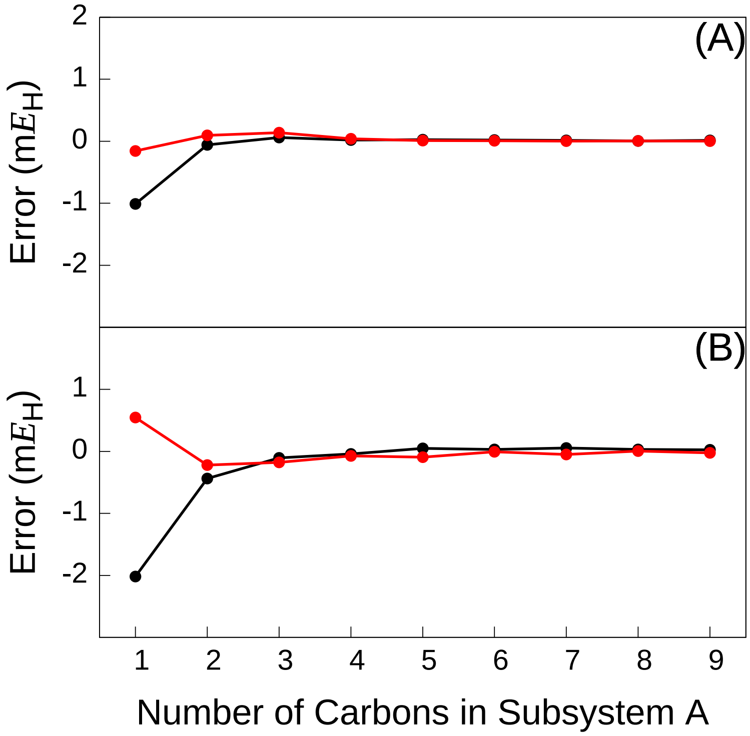

Figure 4.6: The error in CCSD(T)-in-B3LYP embedding (black open circles) and MP2-corrected CCSD(T)-in-B3LYP embedding (red filled circles) as a function of the number of carbons included in subsystem A for the exchange of fluoride to a hydride in (a) 1-fluorodecane and (b) 1-fluoro-1,3,5,7,9-decapentaene.

Finally, we consider the reaction of exchanging the fluoride anion from 1-fluorodecane and 1-fluoro-1,3,5,7,9-decapentaene with a hydride (Figure 4.6). The change in dipole moment for these reactions is provided in Table 4.2. These reactions exhibit a moderate change in dipole moment, and there is good agreement between CCSD and KS-DFT.

Figures 4.6A and 4.6B plot the error in the CCSD(T)-in-B3LYP embedding and MP2-corrected CCSD(T)-in-B3LYP embedding energies for the hydride exchange reactions from alkane and alkene chains, respectively, as a function of the number of carbons included in subsystem A. For every partition, the errors are small. For the smallest division, the MP2 correction provides a significant improvement in the accuracy of the CCSD(T)-in-B3LYP embedding energy; for larger divisions, the effect of the MP2 correction is much smaller. Unlike in the case of fluoride anion dissociation, DFT applied to the hydride exchange reaction accurately represents the change in dipole. As there are no large errors arising from the DFT energy of subsystem B, WFT-in-DFT embedding performs accurately and the MP2 correction further improves the energetics.

The important observation from these calculations is that when there is a large error in the DFT calculation on the environment, there will be correspondingly large errors in the WFT-in-DFT embedding energy. Importantly, this failure is associated with errors intrinsic to the DFT functionals, and does not arise due to errors in the embedding potential. When a chemical process involves a large change in the Mulliken population of subsystem B located on the subsystem A atoms, it is likely that the embedding error will be dominated by errors arising from the DFT-level treatment of subsystem B; errors of this sort cannot be reduced by the MP2 correction.

4.5 Conclusions

Projector-based quantum embedding provides a scheme for multiscale descriptions with the exactness property that DFT-in-DFT is equivalent to DFT on the whole system.[36,37] In many tests and applications, we find the accuracy of the scheme to be excellent, allowing for aggressive partitioning across covalent bonds close to the reactive center of the system of interest. However, for some applications, the errors introduced by embedding are larger than would typically be acceptable, and the principal aims of this paper have been to understand and take steps towards resolving the errors in such cases.

Careful comparison of CCSD(T)-in-DFT embedding calculations with full CCSD(T) calculations has led to key insights regarding the sources of error in the embedding calculations. First, the embedding potential obtained using approximate density functionals is found to be accurate for all of the cases we have investigated, making a contribution to the overall error of the embedding calculation that is negligible compared to other sources of error. It was not immediately obvious that this would be the case, because functionals (particularly in cases where they are parameterized) are designed with accurate energies in mind.

And second, it is found that in many cases, the primary source of error in CCSD(T)-in-DFT embedding is the treatment of nonadditive exchange-correlation effects with an approximate density functional. This is important because it is the one term in the error for which simple corrections can be developed that conserve the efficiency of the original method. Here, we found that use of MP2 or SOS-MP2 corrections for this term typically improved the accuracy of the energetics for chemical reactions, reducing the average error from 4.6 mE_h to 1.2 mE_h with respect to full CCSD(T) calculations.

To investigate the convergence with respect to the size of subsystem A, we studied dissociation and exchange events at the terminus of 10-carbon alkyl and conjugated chains. For the removal of F^-, the results of the CCSD(T)-in-DFT embedding calculation for the conjugated system are noticeably worse than for the alkane, and it is found that the MP2 correction does not reduce this error in the computed reaction energy. Our analysis shows, however, that these results follow from the fact that DFT provides a poor description of the polarization of the charged alkene fragment and that the uncorrected CCSD(T)-in-DFT results benefit from a cancellation of errors in the DFT treatment of subsystem B and in the DFT treatment of nonadditive exchange-correlation. The MP2 correction improves the description of nonadditive energy term, but it does not compensate for the inaccuracies in the DFT description of subsystem B.

For a hydride exchange reaction at the terminus of the alkyl and conjugated chains, the CCSD(T)-in-DFT embedding results converge smoothly and rapidly to reference CCSD(T) calculations performed over the full system, regardless of inclusion of the MP2 correction and regardless of conjugation in the chain. These results demonstrate that in the regime where DFT is adequate for the treatment of the environment, our projector-based embedding scheme can effectively partition the system, even in conjugated molecules.

The current work demonstrates that projection-based embedding provides both a rigorous and practical approach to embedding correlated wavefunctions in a DFT description of the environment. Although the results presented here utilize coupled-cluster methods for describing the correlated wavefunction, we emphasize that projection-based embedding can be combined just as easily with multi-reference electronic structure methods, as well as any mean-field description of the environment. The embedding method is straightforward to employ - requiring only the specification of which atoms are to be treated at the WFT and DFT levels of theory - and it is fully implemented and available in the Molpro quantum chemistry package.

4.6 Accurate and Systematically Improvable Density Functional Theory Embedding for Correlated Wavefunctions: Supplemental Information

4.6.1 Potential Energy Surfaces

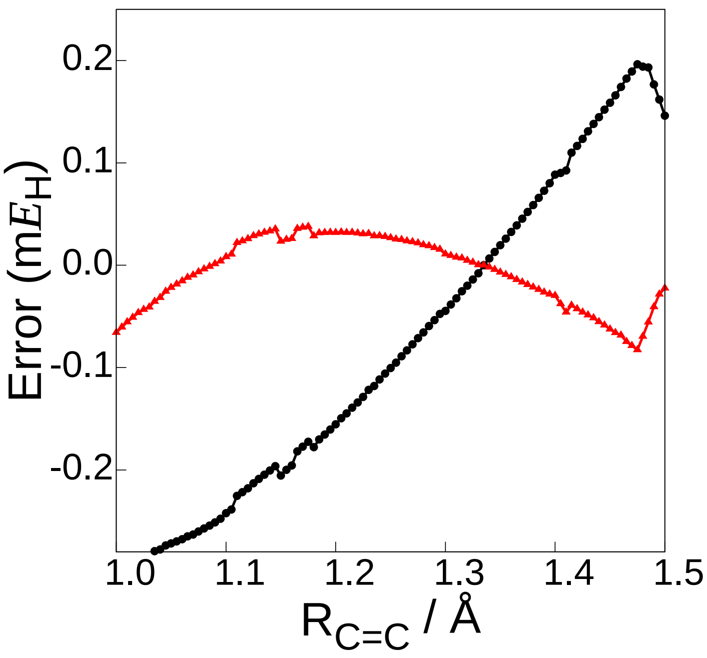

Figure 4.7: Graph of the error in CCSD(T)-in-B3LYP (black) and MP2 corrected CCSD(T)-in-B3LYP (red) as a function of distance between the carbon-carbon double bond. The O=C=CH–CH$_2$– moiety was treated at the CCSD(T) level for the CCSD(T)-in-B3LYP embedding calculations. Abrupt changes in the localized orbitals for different nuclear configurations lead to discontinuities in the WFT-in-DFT energy and its derivatives

4.7 Data Set Computational Details

Molecular geometries are reported in angstrom using Cartesian coordinates.

4.7.1 Symmetric S$_N$2 Reaction Barrier

Propylchloride
KS-DFT (B3LYP) / 6-311g*++ Optimized Geometry
Subsystem A atoms: C8, H9, H10, Cl11

C1	-1.823996	-0.717480	0.144292
H2	-2.784508	-0.872856	-0.353495
H3	-1.203709	-1.595688	-0.046137
H4	-2.013376	-0.669699	1.221397
C5	-1.151988	0.559917	-0.359191
H6	-1.810375	1.420026	-0.177162
H7	-1.004107	0.511737	-1.442695
C8	0.173632	0.884185	0.310894
H9	0.573039	1.838983	-0.026992
H10	0.089151	0.898664	1.397499
Cl11	1.468705	-0.346524	-0.067552

Transition State

KS-DFT (B3LYP) / 6-311g*++ Optimized Geometry

Subsystem A atoms: C1, H2, H3, Cl11, Cl12

C1	0.000719	-0.388805	0.105519
H2	0.000666	-1.250604	0.746120
H3	0.000734	-0.559306	-0.953281
C4	0.000193	0.996697	0.687217
H5	-0.878266	1.089608	1.331323
H6	0.879535	1.090788	1.329810
C7	-0.001812	2.094992	-0.373882
H8	-0.005528	3.088594	0.087416
H9	0.887844	2.018883	-1.005190
H10	-0.889460	2.013099	-1.006979
Cl11	2.416740	-0.696767	-0.089570
Cl12	-2.416159	-0.697843	-0.089391

4.7.2 Acid Hydrolysis Reaction Energy

Dimethyl Ether
KS-DFT (B3LYP) / Def2-TZVP Optimized Geometry
Subsystem A atoms: C1, O2, H3, H4, H5

C1	-1.173920	0.194451	0.000000
O2	-0.000001	-0.586419	0.000000
H3	-1.231875	0.834561	-0.890754
H4	-1.231865	0.834609	0.890722
H5	-2.021089	-0.490198	0.000022
C6	1.173921	0.194451	0.000000
H7	2.021088	-0.490200	0.000005
H8	1.231861	0.834579	0.890742
H9	1.231879	0.834589	-0.890736

Methanol
KS-DFT (B3LYP) / Def2-TZVP Optimized Geometry
Subsystem A atoms: O2, H6

C1	0.665448	-0.020220	0.000000
O2	-0.748210	0.122194	0.000000
H3	1.028648	-0.544325	-0.891167
H4	1.028648	-0.544324	0.891167
H5	1.083163	0.985675	0.000000
H6	-1.147468	-0.753259	0.000000

CH_3^+
KS-DFT (B3LYP) / Def2-TZVP Optimized Geometry
Subsystem A atoms: C1, H2, H3, H4

C1	0.000000	-0.000001	0.000000
H2	0.945569	-0.545889	-0.000001
H3	-0.945544	-0.545931	-0.000001
H4	-0.000024	1.091829	-0.000001

4.7.3 Phenol Deprotonation

Phenol
KS-DFT (B3LYP) / Def2-TZVP Optimized Geometry
Subsystem A atoms: O1, H6

C1	0.218552	-1.219283	0.000014
C2	-1.168651	-1.184791	-0.000069
C3	-1.850797	0.028852	-0.000109
C4	-1.127187	1.214896	-0.000067
C5	0.263118	1.193734	0.000013
C6	0.936484	-0.025561	0.000056
H1	0.758987	-2.15667	0.00005
H2	-1.721496	-2.115963	-0.000101
H3	-2.932538	0.048567	-0.000172
H4	-1.643317	2.16685	-0.000098
H5	0.823932	2.12249	0.00004
O1	2.300596	-0.110893	0.000128
H6	2.680547	0.774789	0.000232

Phenolate
KS-DFT (B3LYP) / Def2-TZVP Optimized Geometry
Subsystem A atoms: O1

C1	1.077309	0.000000	-0.000014
C2	0.286113	1.209101	-0.000003
C3	-1.097619	1.196760	0.000012
C4	-1.823396	0.000000	0.000013
C5	-1.097619	-1.196759	0.000010
C6	0.286113	-1.209102	-0.000005
H1	0.829304	2.149743	-0.000005
H2	-1.634545	2.143825	0.000017
H3	-2.907447	0.000000	0.000035
H4	-1.634545	-2.143825	0.000013
H5	0.829303	-2.149744	-0.000009
O1	2.341566	0.000000	-0.000016

4.7.4 Ring Closing

Ring Open
KS-DFT (B3LYP) / Def2-TZVP Optimized Geometry
Subsystem A atoms: C12,C15,C16,H17,H18,C19,H20,H21,H22

C1	-3.545023	0.629867	-0.421139
C2	-2.506770	-0.227213	0.300475
H3	-3.361405	1.694576	-0.256667
H4	-4.555825	0.409794	-0.071888
H5	-3.521013	0.454536	-1.499548
C6	-1.075186	0.045717	-0.160699
H7	-2.739265	-1.286652	0.148181
H8	-2.577664	-0.054295	1.379802
C9	-0.033543	-0.824403	0.557100
H10	-0.838343	1.103391	-0.006521
H11	-0.998423	-0.127598	-1.239341
C12	1.388709	-0.552578	0.125819
H13	-0.266039	-1.879491	0.392857
H14	-0.114525	-0.651038	1.637376
C15	1.939021	0.764969	0.494120
C16	2.110936	-1.464774	-0.530108
H17	3.144393	-1.286877	-0.798480
H18	1.691125	-2.425795	-0.801128
C19	2.771005	1.502943	-0.237972
H20	1.601127	1.161132	1.449678
H21	3.142039	2.454299	0.121039
H22	3.098937	1.186855	-1.220934

Ring Closed

KS-DFT (B3LYP) / Def2-TZVP Optimized Geometry

Subsystem A atoms: C12,C15,C16,H17,H18,C19,H20,H21,H22

C1	3.794291	0.519261	0.000003
C2	2.639877	-0.480728	-0.000003
H3	3.758022	1.164438	-0.881470
H4	4.761328	0.012414	-0.000002
H5	3.758024	1.164425	0.881486
C6	1.263955	0.185711	0.000001
H7	2.724185	-1.134284	0.874923
H8	2.724184	-1.134273	-0.874938
C9	0.107415	-0.813847	-0.000002
H10	1.176665	0.837654	-0.875560
H11	1.176667	0.837647	0.875568
C12	-1.248215	-0.197709	-0.000001
H13	0.192433	-1.477758	0.870558
H14	0.192433	-1.477754	-0.870565
C15	-1.733584	1.050750	-0.000003
C16	-2.624861	-0.841354	0.000003
H17	-2.872972	-1.429596	-0.887456
H18	-2.872969	-1.429592	0.887466
C19	-3.185495	0.621333	0.000000
H20	-1.268168	2.028627	-0.000006
H21	-3.765065	0.888772	-0.886974
H22	-3.765062	0.888776	0.886975

4.7.5 Diels Alder

Methyl Vinyl Ketone
KS-DFT (B3LYP) / 6-31G* Optimized Geometry
Subsystem A atoms: C1,H1,C2,H2,H3,C3,O1

C1	0.876535	-0.634977	-0.000004
H1	0.993976	-1.716638	0.000005
C2	1.942550	0.172493	0.000004
H2	2.953994	-0.224441	0.000020
H3	1.852200	1.255508	-0.000004
C3	-0.544547	-0.189222	-0.000028
O1	-1.435445	-1.025231	0.000011
C4	-0.858775	1.298350	0.000004
H4	-0.434414	1.789750	0.883609
H5	-0.434444	1.789780	-0.883599
H6	-1.942326	1.428021	0.000024

2-methoxy-1,3-butadiene
KS-DFT (B3LYP) / 6-31G* Optimized Geometry
Subsystem A atoms: C1,C4,C2,H3,C3,H4,H5,H1,H2

C1	0.617061	1.646444	-0.000018
H1	1.694859	1.746315	-0.000110
H2	0.038603	2.562692	0.000138
C2	-1.487945	0.367430	0.000047
C3	-2.185049	-0.774091	0.000042
H3	-2.005313	1.324367	0.000116
H4	-3.270785	-0.767429	0.000099
H5	-1.692300	-1.740640	-0.000031
O1	0.579814	-0.762164	-0.000208
C4	-0.023554	0.461802	-0.000068
C5	1.997125	-0.795343	0.000129
H6	2.407626	-0.307484	-0.893910
H7	2.407176	-0.307121	0.894173
H8	2.275794	-1.850840	0.000397

Transition State

KS-DFT (B3LYP) / 6-31G* Optimized Geometry

Subsystem A atoms: C1,C2,C3,C4,C5,C6,H1,H2,H3,H4,H5,H6,H7,H8,C7,O1

C1	1.068810	-0.812570	0.719810
C2	-0.339230	-1.188850	-0.695950
C3	-1.266210	-0.148460	-0.876330
C4	-0.304900	1.715430	0.605970
C5	1.004030	1.590610	0.231600
C6	1.712240	0.368160	0.321740
H1	-1.130060	0.556110	-1.689640
H2	0.355970	-1.381110	-1.508990
H3	-0.678730	-2.097060	-0.202640
H4	1.635290	-1.737950	0.762130
H5	-0.866540	2.614980	0.375910
H6	-0.764700	1.054020	1.327930
H7	1.487360	2.384380	-0.333520
H8	0.347890	-0.721890	1.524310
C7	-2.592740	-0.095470	-0.255940
O1	-3.435810	0.724000	-0.615230
C8	-2.932550	-1.097300	0.849810
H9	-3.061010	-2.104130	0.432560
H10	-2.148450	-1.163030	1.614860
H11	-3.870750	-0.793220	1.318090
O2	2.936890	0.401990	-0.277740
C9	3.765940	-0.749750	-0.211570
H12	4.727800	-0.448890	-0.630610
H13	3.904990	-1.083200	0.824760
H14	3.359950	-1.577760	-0.806160

Product

KS-DFT (B3LYP) / 6-31G* Optimized Geometry

Subsystem A atoms: C3,C8,C2,C1,C4,C5,H7,H6,H8,H5,H2,H3,H1,C6,O1

C1	-1.097853	-0.009400	0.307622
H1	-0.934291	-0.461527	1.296642
C2	-0.395447	-0.905157	-0.741185
H2	-0.861748	-1.897406	-0.785253
H3	-0.527828	-0.444533	-1.727887
C3	1.101813	-1.049944	-0.432388
H4	1.246067	-1.766230	0.390560
H5	1.616769	-1.478343	-1.302945
C4	-0.485038	1.400083	0.279829
H6	-0.903187	1.945611	-0.577138
H7	-0.808110	1.957516	1.170221
C5	1.019771	1.371473	0.219750
H8	1.558008	2.294164	0.423611
C6	-2.601257	0.012621	0.023153
O1	-3.092155	0.811145	-0.753610
C7	-3.449014	-1.027538	0.734995
H9	-3.495173	-0.790941	1.806419
H10	-4.460915	-1.032016	0.324814
H11	-3.005536	-2.027088	0.650795
O2	3.102253	0.393352	-0.206064
C8	1.730467	0.282418	-0.094316
C9	3.875760	-0.623808	0.415869
H12	3.702491	-1.613323	-0.027993
H13	4.921497	-0.349057	0.259886
H14	3.675958	-0.677301	1.495684

Bibliography

[1] A. Warshel, and M. Karplus, J. Amer. Chem. Soc. **94**, 5612 (1972).

[2] A. Warshel, and M. Levitt, J. Mol. Biol. **103**, 227 (1976).

[3] P. Sherwood, A. H. de Vries, S. J. Collins, S. P. Greatbanks, N. A. Burton, M. A. Vincent, and I. H. Hillier, Faraday Discuss. **106**, 79 (1997).

[4] J. L. Gao, P. Amara, C. Alhambra, and M. J. Field, J. Phys. Chem. A **102**, 4714 (1998).

[5] H. Lin, and D. G. Truhlar, Theor. Chem. Acc. **117**, 185 (2007).

[6] H. M. Senn, and W. Thiel, Angew. Chem., Int. Ed. **48**, 1198 (2009).

[7] L. Hu, P. Söderhjelm, and U. Ryde, J. Chem. Theory Comput. **7**, 761 (2011).

[8] S. Dapprich, I. Komáromi, K. S. Byun, K. Morokuma, and M. J. Frisch, THEOCHEM **461-462**, 1 (1999).

[9] F. Maseras, and K. Morokuma, J. Comp. Chem. **16**, 1170 (1995).

[10] K. Kitaura, E. Ikeo, T. Asada, T. Nakano, and M. Uebayasi, Chem. Phys. Lett. **313**, 701 (1999).

[11] D. G. Fedorov, and K. Kitaura, J. Chem. Phys. **120**, 6832 (2004).

[12] D. G. Fedorov, and K. Kitaura, J. Phys. Chem. A **111**, 6904 (2007).

[13] P. Arora, W Li, P. Piecuch, J. W. Evans, M. Albao, and M. S. Gordon, J. Phys. Chem. C **114**, 12649 (2010).

[14] S. R. Pruitt, M. A. Addicoat, M. A. Collins, and M. S. Gordon, Phys. Chem. Chem. Phys. **14**, 7752 (2012).

[15] K. R. Brorsen, N. Minezawa, F. Xu, T. L. Windus, and M. S. Gordon, J. Chem. Theory Comput. **8**, 5008 (2012).

[16] A. Gaenko, T. L. Windus, M. Sosonkina, and M. S. Gordon, J. Chem. Theory Comput. **9**, 222 (2013).

[17] G. Senatore and K. Subbaswamy, Phys. Rev. B **34**, 5754 (1986).

[18] P. Cortona, Phys. Rev. B **44**, 8454 (1991).

[19] T. A. Wesolowski and A. Warshel, J. Phys. Chem. **97**, 8050 (1993).

[20] J. D. Goodpaster, N. Ananth, F. R. Manby, and T. F. Miller III, J. Chem. Phys. **133**, 084103 (2010).

[21] J. D. Goodpaster, T. A. Barnes, and T. F. Miller III, J. Chem. Phys. **134**, 164108 (2011).

[22] Ł. Rajchel, P. S. Żuchowski, M. M. Szczęśniak, and G. Chałasiński, Chem. Phys. Lett. **486**, 160 (2010).

[23] S. Fux, C. R. Jacob, J. Neugebauer, L. Visscher, and M. Reiher, J. Chem. Phys. **132**, 164101 (2010).

[24] J. Nafziger, Q. Wu, and A. Wasserman, J. Chem. Phys. **135**, 234101 (2011).

[25] N. Govind, Y. A. Yang, A. J. R. da Silva, and E. A. Carter, Chem. Phys. Lett. **295**, 129 (1998).

[26] N. Govind, Y. A. Wang, and E. A. Carter, Phys. Rev. B **110**, 7677 (1999).

[27] A. S. P. Gomes, C. R. Jacob, and L. Visscher, Phys. Chem. Chem. Phys. **10**, 5353 (2008).

[28] T. A. Wesolowski, Phys. Rev. A **77**, 012504 (2008).

[29] Y. G. Khait, and M. R. Hoffmann, J. Chem. Phys. **133**, 044107 (2010).

[30] C. Huang, M. Pavone, and E. A. Carter, J. Chem. Phys. **134**, 154110 (2011).

[31] C. Huang, and E. A. Carter, J. Chem. Phys. **135**, 194104 (2011).

[32] S. Hofener, A. S. P. Gomes, and L. Visscher, J. Chem. Phys. **136**, 044104 (2012).

[33] O. Roncero, A. Zanchet, P. Villarreal, and A. Aguado, J. Chem. Phys. **131**, 234110 (2009).

[34] A. Severo Pereira Gomes, and C. R. Jacob, Annu. Rep. Prog. Chem., Sect. C: Phys. Chem. **108**, 222 (2012).

[35] J. D. Goodpaster, T. A. Barnes, F. R. Manby, and T. F. Miller III, J. Chem. Phys. **137**, 224113 (2012).

[36] F. R. Manby, M. Stella, J. D. Goodpaster, and T. F. Miller III, J. Chem. Theory Comput. **8**, 2564 (2012).

[37] T. A. Barnes, J. D. Goodpaster, F. R. Manby, and T. F. Miller III, J. Chem. Phys. **139**, 024103 (2013).

[38] P. G. Lykos, and R. G. Parr, J. Chem. Phys. **24**, 1166 (1956).

[39] J. C. Phillips, and L. Kleinman, Phys. Rev. **116**, 287 (1959).

[40] A. A. Cantu, and S. Huzinaga, J. Chem. Phys. **55**, 5543 (1971).

[41] H. Stoll, B. Paulus, and P. Fulde, J. Chem. Phys. **123**, 144108 (2005).

[42] R. A. Mata, H.-J. Werner, and M. Schütz, J. Chem. Phys. **128**, 144106 (2008).

[43] T. M. Henderson, J. Chem. Phys. **125**, 014105 (2006).

[44] B. Swerts, L. F. Chibotaru, R. Lindh, L. Seijo, Z. Barandiaran, S. Clima, K. Pierloot, and M. F. A. Hendrickx, J. Chem. Theory Comput. **4**, 586 (2008).

[45] J. L. Pascual, N. Barros, Z. Barandiaran, and L. Seijo, J. Phys. Chem. A **113**, 12454 (2009).

[46] C. Hampel, K. Peterson, and H.-J. Werner, Chem. Phys. Lett. **190**, 1 (1992).

[47] C. Hampel and H.-J. Werner, J. Chem. Phys. **104**, 6286 (1996).

[48] M. Schütz and F.-R. Manby, Phys. Chem. Chem. Phys. **5**, 3349 (2003).

[49] H.-J. Werner and M. Schütz, J. Chem. Phys. **135**, 144116 (2011).

[50] M. Schütz and H.-J. Werner, Chem. Phys. Lett. **318**, 370 (2000).

[51] M. Schütz, J. Chem. Phys. **113**, 9986 (2000).

[52] M. Schütz, G. Rauhut, and H.-J. Werner, J. Phys. Chem. A **102**, 5997 (1998).

[53] M. J. Frisch, G. W. Trucks, H. B. Schlegel, G. E. Scuseria, M. A. Robb, J. R. Cheeseman, G. Scalmani, V. Barone, B. Mennucci, G. A. Petersson, H. Nakatsuji, M. Caricato, X. Li, H. P. Hratchian, A. F. Izmaylov, J. Bloino, G. Zheng, J. L. Sonnenberg, M. Hada, M. Ehara, K. Toyota, R. Fukuda, J. Hasegawa, M. Ishida, T. Nakajima, Y. Honda, O. Kitao, H. Nakai, T. Vreven, J. A. Montgomery, Jr., J. E. Peralta, F. Ogliaro, M. Bearpark, J. J. Heyd, E. Brothers, K. N. Kudin, V. N. Staroverov, R. Kobayashi, J. Normand, K. Raghavachari, A. Rendell, J. C. Burant, S. S. Iyengar, J. Tomasi, M. Cossi, N. Rega, J. M. Millam, M. Klene, J. E. Knox, J. B. Cross, V. Bakken, C. Adamo, J. Jaramillo, R. Gomperts, R. E. Stratmann, O. Yazyev, A. J. Austin, R. Cammi, C. Pomelli, J. W. Ochterski,

R. L. Martin, K. Morokuma, V. G. Zakrzewski, G. A. Voth, P. Salvador, J. J. Dannenberg, S. Dapprich, A. D. Daniels, . Farkas, J. B. Foresman, J. V. Ortiz, J. Cioslowski, and D. J. Fox, Gaussian, Inc., Wallingford CT, 2009.

[54] H.-J Werner, P. J. Knowles, R. Lindh, F. R. Manby, M. Shütz et al., MOLPRO, version 2012.1, a package of *ab initio* programs, 2012, see www.molpro.net.

[55] J. Pipek, and P. Mezey, J. Chem. Phys. **90**, 4916 (1989).

[56] T. H. Dunning, Jr., J. Chem. Phys. **90**, 1007 (1989).

[57] T. H. Dunning, Jr., K. A. Peterson, and A. K. Wilson, J. Chem. Phys. **114**, 9244 (2001).

[58] A. D. Becke, J. Chem. Phys. **98**, 5648 (1993).

[59] J. A. Pople, and P. C. Haharan, Theor. Chim. Acta **28**, 213 (1973).

[60] F. Weigend, and R. Ahlrichs, Phys. Chem. Chem. Phys. **7**, 3297 (2005).

[61] W. J. Hehre, R. Ditchfield, and J. A. Pople, J. Chem. Phys. **56**, 2257 (1972).

[62] J. P. Perdew, K. Burke, and M. Ernzerhof, Phys. Rev. Lett. **77**, 3865 (1996).

[63] Y. Zhao, and D. G. Truhlar, Theor. Chem. Account **120**, 215 (2008).

[64] C. Moller, and M. S. Plesset, Theor. Chem. Account **46**, 0618 (1934).

[65] M. Schütz, G. Hetzer, and H.-J. Werner, J. Chem. Phys. **111**, 5691 (1999).

[66] Y. Jung, R. C. Lochan, A. D. Dutoi, and M. Head-Gordon, J. Phys. Chem. **121**, 9793 (2004).

[67] N. J. Russ and T. D. Crawford, J. Chem. Phys. **121**, 691 (2004).

[68] H. L. Woodcock, H. F. Schaefer III, and P.-R. Schreiner, J. Phys. Chem. A **106**, 11923 (2002).

Outlook

This work shows the significant progress contributed by this thesis to the development of embedded density functional theory for the treatment of correlated wavefunctions. We started with a simple single electron embedded in an atomic system, progressed to covalent bonded molecular systems, and advanced to transition metals and large complex chemical systems. The methodology has not only advanced the size and complexity of systems which can be treated, but also the accuracy and robustness. However, significant challenges remain to be addressed and are discussed briefly here.

Chapter 4 discussed the use of computationally inexpensive wavefunction methods to evaluate the nonadditive exchange-correlation energy. In those cases we applied the use of MP2 theory, and it proved very accurate. However, there are many systems in which MP2 theory will give qualitatively inaccurate results, such as transition metal complexes and complexes with near degeneracies. Therefore, alternative inexpensive wavefunction methods, such as the random phase approximation, should be explored to determine the accuracy of those methods in the context of WFT-in-DFT.

The methodology used in chapter 4 employs the KS-DFT density for subsystem B, which was obtained from performing a KS-DFT calculation on the full system. However, in some systems the density in subsystem A may change significantly from KS-DFT to wavefunction theory. Therefore, the next challenge to the field is how to relax the density of subsystem B, after one obtains the density of subsystem A. This self-consistent minimization allows for the two subsystems to be correctly polarized.

This self-consistent procedure will allow for the total systems orbitals to be at the absolute minimum, which has several advantages. First, it allows for the treatment of excited states. If an excited-state wavefunction calculation is performed on subsystem A, subsystem B can polarize to the excited state and should be significantly more accurate than frozen density embedding.

A self-consistent procedure would also allow for the calculation of atomic forces through the use of the Hellmann-Feynman theorem. This would allow for geometry optimizations at the WFT-in-DFT level of theory. Previous experience has shown that geometries obtained at the KS-DFT level of theory can be inaccurate compared to experimental geometries, particularly for transition metal complexes. However, this requires the use of WFT methods with computationally tractable gradients. For many WFT methods, geometry optimization is too costly for all but the smallest of systems, and this remains a great challenge to the WFT community.

Although several challenges remain in the WFT-in-DFT methodology, it is important to emphasize how breakthroughs in both WFT and DFT can be seamlessly and effortlessly integrated into the field. In this sense, this work will remain complimentary to the work being done in both the WFT and DFT scientific communities.